FRICTION AND WEAR OF ZIRCONIA AND ALUMINA CERAMICS DOPED WITH CuO

Henry Rihard Pasaribu

The research in this thesis is sponsored by the Dutch Technology Foundation (STW).

De promotiecommissie is als volgt samengesteld:

Prof. dr. ir. H.J. Grootenboer, Universiteit Twente, voorzitter en secretaris
Prof. dr. ir. D.J. Schipper, Universiteit Twente, promotor
Prof. dr. ir. J. Huétink, Universiteit Twente
Prof. dr. ir. G.J. Vancso, Universiteit Twente
Prof. dr. ing. D.H.A. Blank, Universiteit Twente
Prof. dr. ir. P. de Baets, Universiteit Gent, België
Prof. dr. E. Santner, BAM, Berlijn, Duitsland

Pasaribu, Henry Rihard
FRICTION AND WEAR OF ZIRCONIA AND ALUMINA CERAMICS DOPED WITH CuO
Ph.D. Thesis, University of Twente, Enschede, the Netherlands
February 2005

ISBN 90-365-2143-2

Keywords:
tribology, ceramics, zirconia, alumina, copper oxide, low friction, wear resistant

Printed by Wöhrmann Print Service, the Netherlands.

FRICTION AND WEAR OF ZIRCONIA AND ALUMINA CERAMICS DOPED WITH CuO

PROEFSCHRIFT

ter verkrijging van
de graad van doctor aan de Universiteit Twente,
op gezag van de rector magnificus,
prof. dr. W.H.M. Zijm,
volgens besluit van het College voor Promoties,
in het openbaar te verdedigen
op vrijdag 11 februari 2005 om 16.45 uur

door

Henry Rihard Pasaribu
geboren op 17 juni 1976
te Binjai, Indonesië

Dit proefschrift is goedgekeurd door:

de promotor, prof.dr.ir. D.J. Schipper

to my wife, Susy
to my son, Daniel
to my beloved family in Indonesia

Summary

At present, there is considerable interest in the application of ceramics as, for instance, components in machines without lubrication. For a dry sliding system, an engineer needs to know the maximum operating conditions applicable to a ceramic material combination in order for it to operate safely, i.e. such that no severe wear takes place. In this thesis, a wear model is developed that relates the properties of the materials and the operating conditions to the type of wear (mild or severe wear) experienced by dry sliding ceramic systems (chapter 2). The wear model is verified experimentally, and hence, with this model, one can determine whether a dry sliding ceramic system will experience mild wear or severe wear.

In the wear model, it appears that the coefficient of friction has a significant influence in determining the wear type of dry sliding ceramic systems. Therefore, to extend the operating conditions (normal load and sliding velocity) of the mild wear regime, a low friction tribosystem is required. A low friction tribosystem can be achieved by having hard materials in contact to support the normal load and a weak interface between the two opposing surfaces to provide easy shear. This idea is implemented by adding various weight percentages of copper oxide (CuO) into alumina and zirconia ceramics (chapter 3). The dry sliding tests conducted on these materials showed that the coefficient of friction of alumina doped with CuO sliding against alumina decreases from 0.7 down to 0.4 and hardly depends on normal load and sliding velocity. On the other hand, CuO doped in zirconia sliding against alumina can reduce the coefficient of friction from 0.8 to a value of 0.2 to 0.3 depending on the operational conditions. SEM pictures taken from the wear track of zirconia doped with CuO, where low friction was observed, reveal that a smooth (patchy) layer is formed. The hardness measurements and the chemical composition analysis of the patchy layer suggest that the addition of CuO in zirconia is responsible in providing a soft interfacial layer in the contact that reduces friction.

To analyze the tribosystem of zirconia doped with CuO sliding against alumina, which is in fact a soft thin layer on top of a hard substrate sliding against a hard rough surface, a general deterministic contact model of a rough surface in contact with a flat layered surface was developed (chapter 4). The developed contact model was found to be in good agreement with the experimental and numerical data available in the literature. Further, the deterministic contact model was extended to a deterministic friction model of a rough surface sliding against a flat layered surface (chapter 5). The deterministic friction model also showed good agreement with the experimental data reported in the literature. The deterministic friction model is later used to predict the coefficient of friction of the tribosystem of zirconia doped with CuO sliding against alumina (chapter 6). The developed friction model is in good agreement with the experimental results. Finally, recommendations for future research are presented.

Samenvatting

Keramiek wordt meer en meer als materiaal gebruikt in machines en werktuigen waarbij geen smering wordt toegepast. De ontwerper heeft voor de ongesmeerde contactsituatie ontwerpregels nodig om vast te stellen wat de operationele condities mogen zijn van de gebruikte keramiek combinatie om ernstige slijtage te voorkomen. In hoofdstuk 2 van dit proefschrift is een slijtagemodel uiteengezet waarmee op basis van materiaaleigen-schappen en operationele condities voorspelt kan worden of een milde dan wel een ernstige slijtagevorm zal optreden voor de droge contactsituatie. Dit model is experimenteel gevalideerd.

Dit slijtagemodel geeft aan dat de wrijvingscoëfficiënt een zeer belangrijke parameter is met betrekking tot de slijtagevorm (mild - ernstig) die zal optreden. Daarom is een lage wrijvingscoefficient in belaste keramiek - keramiek contacten zeer gewenst. Dergelijke lage wrijvingsystemen kunnen worden gerealiseerd door de harde materialen, die de belasting overdragen, te voorzien van een dunne zachte laag voor het realiseren een interface met een lage afschuifsterkte tussen de in contact zijnde componenten. Dit principe is toegepast door aan de zirconia en alumina keramieken enige gewichtsprocenten koperoxide (CuO) tijdens de bereidingsfase toe te voegen (hoofdstuk 3). De wrijvings-experimenten uitgevoerd aan deze materialen hebben aangetoond dat de wrijvingscoëfficiënt van alumina met koperoxide in contact met alumina reduceert van 0.7 naar 0.4 en nagenoeg niet afhankelijk is van de normaal belasting en de opgelegde snelheid. Voor zirconia die voorzien is met koperoxide in contact met alumina levert een reductie in de wrijvingscoëfficiënt op van ongeveer 0.8 naar een waarde van 0.2 tot 0.3, afhankelijk van de operationele condities. SEM opnamen van het slijtagespoor op zirconia met koperoxide, waarbij de gewenste lage wrijving is geconstateerd, maken duidelijk dat een gladde discontinue laag is gevormd. Hardheidmetingen en chemische analyse van deze lagen duiden erop dat de toevoeging van koperoxide daadwerkelijk een zachte laag vormt welke verantwoordelijk is voor de gewenste wrijvingsreductie.

Voor het voorspellen van de wrijving van dergelijke tribosystemen, zirconia met enige gewichtsprocenten koperoxide in contact met aluminia, waarbij een dunne zachte laag is gevormd op het harde substraat, is een algemeen deterministisch contactmodel ontwikkeld, (hoofdstuk 4). Dit contactmodel is gevalideerd aan de hand van experimentele en numerieke data uit de literatuur. Dit deterministisch contactmodel is vervolgens uitgebreid naar een deterministisch wrijvingsmodel welke geschikt is voor een ruw glijdend oppervlak in contact met een gecoat oppervlak (hoofdstuk 5). Het deterministisch wrijvingsmodel vertoont goede overeenkomsten met de gepresenteerde data in de literatuur. Met dit model is de wrijving voorspeld van het zirconia voorzien met koperoxide - alumina systeem (hoofdstuk 6). Vergelijking met de uitgevoerde experimenten blijkt dat het ontwikkelde wrijvingsmodel de wrijving van dergelijke systemen goed voorspelt. Ten slotte zijn aanbevelingen voor verder onderzoek gegeven.

Acknowledgement

I thank the engineering design group of ITB, Bandung, Indonesia, who introduced me to Wijtze ten Napel when he visited ITB in 2000. I sincerely thank Wijtze ten Napel and Dik Schipper for giving me the opportunity to carry out the research on the project "nano-scale wear resistant oxide ceramics with low friction".

The nano-scale wear resistant oxide ceramics research project was sponsored by the Dutch technology foundation (STW). I gratefully acknowledge its financial support that made it possible to do this research.

I owe deep thanks to my supervisor, Prof. Schipper, for his guidance and ideas. I also thank him for telling me some Dutch habits which of course helped me in my social life in the Netherlands.

I want to thank Dik Schipper, Dave Blank, Ewa Tocha, Holger Schönherr, Jan-Willem Sloetjes, Julius Vancso, Louis Winnubst, Richard Ran, and Wika Wiratha for the collaboration and discussion in the monthly meetings.

Over the past four years, I have enjoyed the pleasant working environment in the tribology group and I want to thank the (ex-) staff members: Wijtze ten Napel, Dik Schipper, Kees Venner, Matthijn de Rooij, Erik de Vries, Walter Lette, Belinda Bruinink, Willie Kerver and the (former) PhD students: Ako, Bert, Bernd, Caner, Ellen, George, Gerrit, Irinel, Isaias, Jamari, Jan Willem, Loredana, Mark, Marc and Qiang for providing a nice working atmosphere.

I want to thank Karen Reuver who worked with me on my project for her M.Sc. thesis.

I would like to express my deep thanks to my wife, Susy, for her care, courage, and understanding. One of the happiest moments in my life, the birth of my son, Daniel, has made me a proud father. Their presence always brings happiness and harmony in my life. I want to thank my family in Indonesia for their support and prayers.

I thank the members of the Indonesian Student Association, the members of the bible study Twente and the members of the ITC Christian Fellowship that have made my social life in Enschede so enjoyable.

Contents

Nomenclature

Arabic symbols

a	[m]	Half width of the contact area in sliding direction
A	[m^2]	Contact area
A_{nom}	[m^2]	Nominal contact area
A_{tot}	[m^2]	Total contact area
b	[m]	Half width of the contact area perpendicular to sliding direction
B	[m]	Contact length
c	[JK^{-1}]	Specific heat
C_1	[-]	Proportionality constant to calculate the tensile stress at the trailing edge of a concentrated contact due to mechanical loading
C_2	[-]	Proportionality constant to calculate the tensile stress at the trailing edge of a concentrated contact due to thermal loading
d	[m]	Grain size
e	[-]	Eccentricity of an ellipse
E	[Pa]	Elasticity modulus
E_{eff}	[Pa]	Effective elasticity modulus of a layered surface
E^*	[Pa]	Reduced elasticity modulus
f	[-]	Coefficient of friction
F	[N]	Friction force
F_{adh}	[N]	Friction force due to adhesion
F_{pl}	[N]	Friction force due to ploughing
H	[Pa]	Hardness
H_{eff}	[Pa]	Effective hardness of a layered surface
k	[$m^3(Nm)^{-1}$]	Specific wear rate
K	[$W(m\ K)^{-1}$]	Thermal conductivity
K_{IC}	[$Pa(m)^{0.5}$]	Fracture toughness
K_{eff}	[$W(m\ K)^{-1}$]	Effective thermal conductivity
m	[-]	Proportionality constant
m_{bef}	[kg]	Weight of the specimen before an experiment
m_{af}	[kg]	Weight of the specimen after an experiment
P	[N]	Normal load
P_e	[-]	Peclet number
P_o	[Pa]	Maximum Hertzian contact pressure
P_{tot}	[N]	Total load carried by asperities in contact
R	[m]	Radius
S	[-]	Shape factor
$S_{c,m}$	[-]	Mechanical severity parameter for a sliding circular contact
t	[m]	Layer thickness

T	[K]	Temperature
V_w	[m^3]	Volume of material worn away
V	[m/s]	Sliding velocity
x	[m]	Sliding distance
Y	[-]	Geometry constant

Greek Symbols

α	[K^{-1}]	Thermal expansion coefficient
β	[m]	Asperity radius
χ	[-]	Comparison of the indentation depth of an asperity to the critical indentation when fully plastic situation occur
ΔT_s	[K]	Thermal shock resistance
$\phi(s)$	[-]	Distribution of asperities height
γ	[-]	Percentage of a wear track covered by patchy layers
Γ	[-]	Thermal severity parameter
θ	[-]	Flash temperature number
θ_i	[-]	Attack angle
Ξ	[-]	Thermal severity parameter for a sliding circular contact
M	[-]	Mechanical severity parameter
ν	[-]	Poisson's ratio
ν_{eff}	[-]	Effective poisson's ratio of a layered surface
ρ	[$kg(m)^{-3}$]	Mass density
σ_y	[Pa]	Yield stress
σ	[m]	Standard deviation of summit heights
σ_{max}	[Pa]	Maximum stress
$\sigma_{m,C}^{mech}$	[Pa]	Maximum tensile stress due to mechanical loading of a sliding circular contact
$\sigma_{m,E}^{mech}$	[Pa]	Maximum tensile stress due to mechanical loading of a sliding elliptical contact
$\sigma_{m,L}^{mech}$	[Pa]	Maximum tensile stress due to mechanical loading of a sliding line contact
τ	[Pa]	Interfacial shear strength
ω	[m]	Indentation depth
ω_{c1}	[m]	The critical indentation depth when the transition from elastic to elastic plastic contact situation occur
ω_{c2}	[m]	The critical indentation depth when the transition from elastic plastic to fully plastic contact situation occur

Subscripts

1, 2	Surface 1, 2
avg	Average

ad	Adhesion
e	Elastic contact situation
eff	Effective
ep	Elastic plastic contact situation
l	Layer
m	Moving
p	Plastic contact situation
pl	Ploughing
s	Substrate
st	Static

Chapter 1
Introduction

1.1 Ceramics in our daily life

Ceramics are interesting materials. Many products in our daily life are made of ceramics, for example dishes, knives, resistors, bearings, turbine rotors, extrusion dies and many others. Furthermore, for their chemical inertness and biocompatibility, ceramics are used for medical applications such as dental crowns, hip & knee prostheses, heart valves and bone implants.

The word ceramics comes from *keramos*, the ancient Greek word for objects made of fired clay. Ceramics can be defined as inorganic, non-metallic materials. This definition covers not only pottery but also glass, brick, limestone, porcelain, cement and technical ceramics. Ceramics are typically crystalline in nature and are compounds formed between metallic and non-metallic elements, for example alumina ceramic (Al_2O_3), a compound of aluminium and oxygen.

Humankind has known the early ceramics product, pottery, since 30,000 years ago [1]. From that time on, other types of ceramic products like tiles, bricks and cements were invented and have been used to support human life. From generation to generation, ceramics have been continuously developed and their quality improved. Ceramics have played a role in early human civilisation right through modern life.

The invention of the furnace accelerated the improvement of ceramics properties and the invention of new ceramics or ceramic composites [2]. High hardness, high stiffness and chemical inertness make ceramics distinct from other materials. These promising properties have triggered research on improving ceramics for wider technical applications, and particularly for components operating at elevated temperatures.

Faster, lighter and more efficient machines are a big challenge for the automotive and aircraft industries. Ceramics will be the front end material to meet these challenges. A ceramic engine, for instance, is the dream of the automotive and aircraft industries because with ceramics, a higher operational temperature can be achieved which means higher efficiency as well as lighter machines. However, the dream is still far from commercial realisation since the production costs of a ceramic engine are too high and ceramics reveal high friction and high wear at elevated temperatures [3] which limits the life of the machine. Nevertheless, many components of combustion and gas engines are now made of ceramics or covered with a ceramic layer to increase the

performance of the machine, for example zirconia capped ductile iron piston assembly, silicon nitride turbine blades, silicon carbide ball bearings, alumina mechanical face seals and many others. Research on low friction and wear resistant ceramics as well as to reduce the production costs of ceramic components is being carried out in many research groups.

1.2 Technical ceramics

Ceramic materials that are produced from raw material modification and refinement or even synthesized to form new ceramic materials are often called technical, advanced, engineering or fine ceramics [4]. In general, technical ceramics can be classified into oxide ceramics, non-oxide ceramics and ceramic composites. Further, the non-oxides ceramics can be classified based on their chemical components. The classification of ceramics is simply illustrated in figure 1.1.

Generally, oxide ceramics are oxidation resistant, chemically inert, and electrically insulating but have low thermal conductivity. Non-oxide ceramics are low oxidation resistant, electrically conducting, thermally conductive and very hard. Ceramic-based composites were invented by scientists to combine the above to achieve better properties, i.e. zirconia-toughened alumina composite (ZTA), SiAlON, etc.

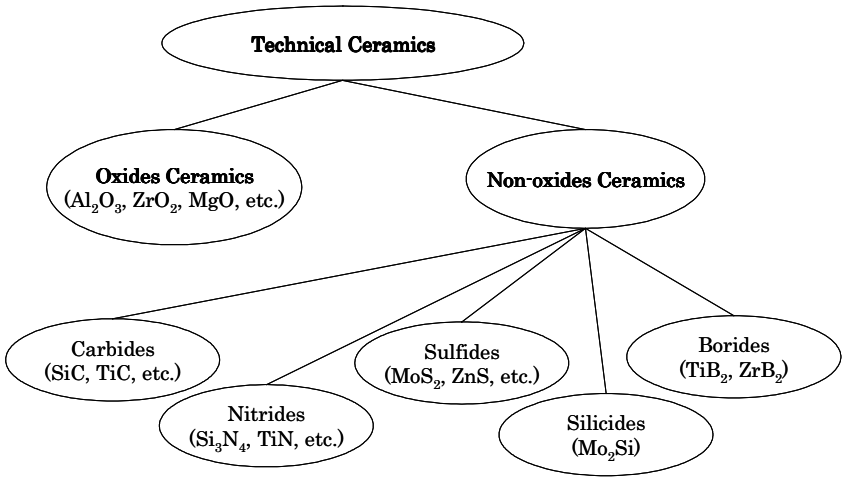

Figure 1.1: Classification of technical ceramics.

A ceramic product is produced by sintering a compacted ceramic powder (green body). High purity ceramic powder is an essential requirement to have a dense ceramic product. The powder is milled in such a way as to achieve an optimum particle size distribution. The large particles in the ceramic powder should be minimized because they can introduce defects and become regions of

stress intensification under load that lead to premature failures. Binder and sintering aid materials are sometimes added to the ceramic powder or the mixture of several ceramic powders in order to achieve better bonding between the particles and to maintain a certain crystal structure at room temperature. A green body, which is more or less close to the geometry of the final product, can be made by many methods like extrusion, injection moulding, pressing, slip casting or tape forming. The green body is sintered at an appropriate temperature for a certain period of time to obtain a dense product. The sintering process is critical because the amount and the method of applying energy as well as the sintering time determine the bonding properties between the powder particles and the amount of porosity in the product. The sintered product is then machined to the designed geometry.

Commercially available structural ceramics like alumina (Al_2O_3), zirconia (ZrO_2), silicon nitride (Si_3N_4) and silicon carbide (SiC) are broadly used in many applications. Properties of these commercially available ceramics are given in table 1.1.

Table 1.1: Properties of commercially available ceramics [5].

Property	Symbol	Unit	Al_2O_3	ZrO_2	SiC	Si_3N_4
Grain size	d	μm	1.8	0.6	6	1.2
Fracture toughness	K_{IC}	MPa.m$^{0.5}$	3.5	10	4	8
Young's modulus	E	GPa	390	205	430	320
Poisson's ratio	υ	-	0.23	0.3	0.17	0.24
Density	ρ	kg/m^3	3900	6050	3200	3100
Thermal expansion coeff.	α	10^{-6}/K	8	10	3.9	3
Thermal conductivity	K	W/(m K)	29	2	110	35
Specific heat	c	J/(kg K)	600	400	1000	800
Thermal shock resistance	ΔT_s	K	200	250	380	600
Hardness	H	GPa	22	14	28	15

Alumina (Al_2O_3) can be found in nature as bauxite which contains hydrated alumina ($Al_2O_3 \cdot H_2O$). By chemical processing, high purity alumina (up to 99.5%) can be obtained. Alumina was originally developed for refractory tubing. Nowadays alumina ceramic is used in many products because it is relatively cheaper and easier to produce compared to the production of other ceramics. In addition, a dense product (99.9 %) made of alumina can be achieved by a good sintering procedure and in combination with its chemical inertness, alumina is chosen for many biomedical applications, for example alumina is used for knee joint replacement.

Zirconia (ZrO_2) has a high melting temperature (2700°C) and it has three kinds of crystal structures. At room temperature, the crystal structure of zirconia is monoclinic while at about 1000°C, the crystal will transform to tetragonal and at even higher temperatures, 2370°C, the tetragonal crystal will transform into a cubic shape crystal. The transformation process is always

accompanied by a great change in volume that is followed by the formation of cracks. However, the addition of Y_2O_3, CaO or MgO into zirconia can maintain the tetragonal or cubic phase at room temperature. Zirconia has a low thermal conductivity and is thus often used for insulation components. The high toughness property of zirconia is attractive for dry sliding systems that operate at low sliding velocities.

Silicon carbide (SiC) is usually produced by mixing high purity silica (SiO_2) with carbon-rich powder and heating them up to 2200-2500°C. The reaction between silica and carbon results in the formation of silicon carbide and carbon monoxide. Silicon carbide is a very hard material and difficult to make into a fine-grained dense ceramic. The high hardness, high thermal shock and high fracture toughness properties has made silicon carbide suitable for high pressure and high temperature applications, for example silicon carbide ball bearings operating at high temperatures.

Silicon nitride (Si_3N_4) consists of two atoms, silicon and nitrogen, which can be found easily on the earth but silicon nitride cannot be found in nature. Silicon nitride is produced by heating up silicon powder at a high temperature (1200°C) in a nitrogen gas atmosphere. This material has the highest thermal shock resistance properties compared to the other ceramics (see table 1). Due to its high thermal shock resistance, silicon nitride (Si_3N_4) ceramic is often used for high temperature applications like turbine rotors in a gas engine.

For more details with respect to ceramics, the reader is referred to Kerkwijk [10] and He [11].

1.3 Friction and wear of materials

Friction and wear are not material properties but system properties that depend on the materials in contact and the operational conditions. When two bodies are in contact and slide over each other, they will experience friction (resistance to motion) and wear (damage and material loss). Friction and wear cannot be avoided in the contact of two bodies with relative motion. Friction is needed for traction and braking systems but must be minimized to reduce energy dissipation due to friction. Wear is needed for cutting processes but should be minimized in sliding and rolling contact applications in order to increase lifetime. There is in general no direct relation between friction and wear but these two phenomena are somehow interrelated.

1.3.1 Friction

Friction is very important in our daily life. Without friction, we cannot walk. A quantitative study of friction was carried out and documented by Leonardo da Vinci (1452-1519). In 1699, Amontons (1663-1705) formulated his observation, now known as the laws of friction. He stated that (1) the friction force is

proportional to the normal load and (2) the friction force is independent of the apparent contact area. In 1785, Coulomb stated that the friction force is independent of sliding velocity, which is now known as the third law of friction. Many material combinations in unlubricated sliding obey the first law of friction, e.g. steel on polished aluminium [6], alumina sliding against zirconia (see figure 1.2) but polymers often do not [7]. The second law is observed when a wood slider slides against a steel surface [8]. The third law is observed in dry sliding contact of alumina doped with 1 % wt CuO against alumina (see figure 1.3).

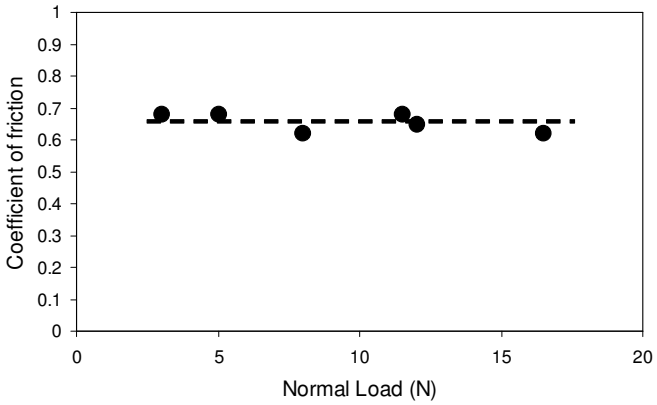

Figure 1.2: Coefficient of friction as a function of normal load of alumina sliding against zirconia (sliding velocity 0.1 m/s).

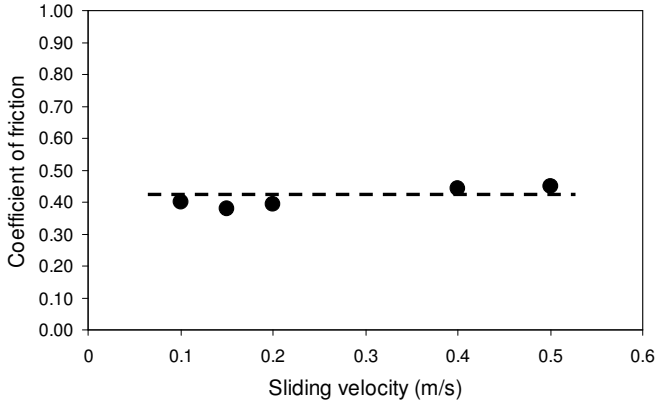

Figure 1.3: Coefficient of friction as a function of sliding velocity of alumina doped with 1 % wt CuO sliding against alumina (normal load 10N).

The friction experience by a moving component is often quantified by the value of the coefficient of friction (f) that can be written, based on the first law of friction, as:

$$f = \frac{F}{P} \tag{1.1}$$

in which F is the friction force and P is the normal load. Bowden and Tabor [6], observed the evidence that the frictional force arises from the adhesion force (F_{adh}) and the deforming force (F_{pl}) as shown schematically in figure 1.4. The adhesion force (F_{adh}) is needed to shear the contact between the surfaces and the deforming force (F_{pl}) is needed by a hard asperity to plough through the softer surface.

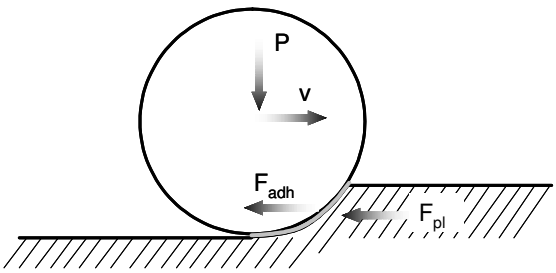

Figure 1.4: Resistance to motion according to Bowden and Tabor [6].

Therefore, the frictional force according to Bowden and Tabor [6] can be expressed as:

$$\begin{aligned} F &= F_{adh} + F_{pl} \\ &= \tau_i A + HA' \end{aligned} \tag{1.2}$$

where τ_i is the interfacial force per unit area required to shear the junction (i), H is the hardness of the softer material, A is the projected normal contact area and A' is the frontal contact area. The interfacial shear strength (τ_i) is the most difficult value to obtain. For a lubricated sliding contact, the shear strength is mostly related to the shear properties of the lubricant whereas for a dry sliding contact there is no direct relation between the interfacial shear strength and the bulk properties, and therefore it must be measured.

1.3.2 Wear

Wear can be defined as progressive loss of material from the rubbing surfaces. There are four basic mechanisms of wear, namely: adhesion, abrasion (wear

associated with the presence of hard particles), fatigue and corrosion. Combinations of these basic mechanisms lead to a characteristic damage mode such as: delamination, fretting, pitting, scuffing and galling [9] (see figure 1.5 and table 1.2).

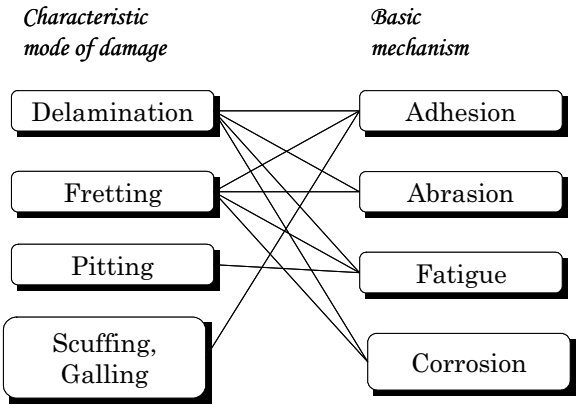

Figure 1.5: Modes of damage and basic mechanisms of wear [9].

Table 1.2: Definition of mode of damage [9].

Mode of damage	Definition
Delamination	Wear initiated by crack propagation at repeated sliding surface resulting in sheet-like wear particles.
Fretting	Wear of material due to oscillatory tangential displacement with small amplitude (at least less than the contact size).
Pitting	Wear due to fatigue which causes cavities or "holes" in the surface.
Scuffing	Gross damage characterized by local welding of the sliding surfaces.

Abrasive wear is frequently observed in dry sliding ceramic couples. Ceramic wear debris that is entrapped in the wear track of a dry sliding ceramic couple will cause a three-body abrasive tribosystem resulting in a grooved wear track [10] (see figure 1.6a). Adhesion wear is observed when ceramics slide against a metal [11]. Metal transfer onto the ceramic surface will occur due to the high adhesion force between the metal and the ceramic (see figure 1.6b). Delamination wear is also observed on zirconia ceramics doped with copper oxide sliding against alumina (see figure 1.6c).

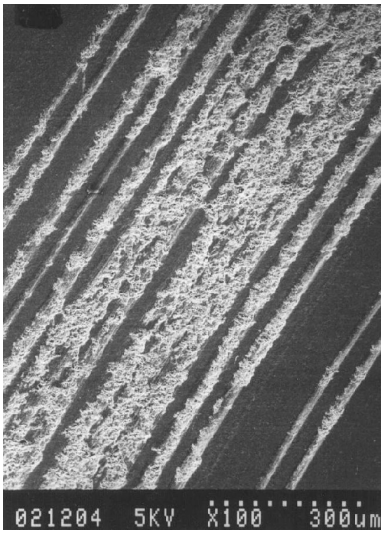

(a)

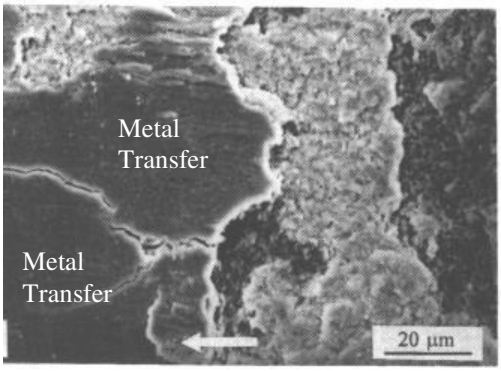

(b)

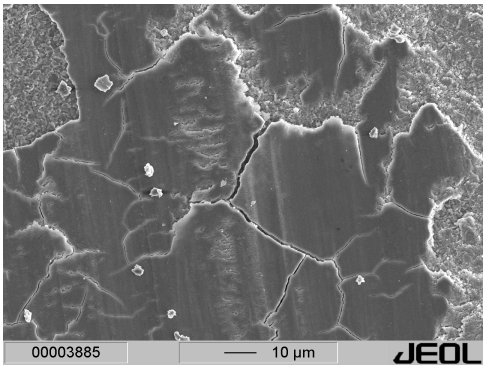

(c)

Figure 1.6: Abrasive wear (a) [10], adhesive wear (b) [11] and delamination wear (c) observed in dry sliding ceramic couples.

The properties and the operating conditions of the tested materials will determine the wear mechanism of a dry sliding system. Besides the wear mechanism, engineers are also interested in quantifying the amount of material that is removed from the surface. Archard [12] proposed an equation to calculate the volume of worn material as:

$$Q = \frac{KP}{H} \tag{1.3}$$

where Q is the volume of material worn per unit sliding distance, P is the normal load, K is a constant (wear coefficient) and H is the hardness of the softer surface. However, for engineering applications the quantity of K/H is often more useful [7]. The ratio K/H is called the specific wear rate (k) and by modifying equation (1.3), the specific wear rate can be calculated as:

$$k = \frac{V_w}{Px}\left[\frac{mm^3}{Nm}\right] \tag{1.4}$$

where V_w is the wear volume and x is the sliding distance.

In practice (see figure 1.7), the volume of worn material can linearly increase (constant specific wear rate) as a function of sliding distance but sometimes a sudden change in wear volume might occur (changing specific wear rate) depending on the wear mechanism involved in the contact. For example, a sudden change in the specific wear rate is observed in a dry sliding contact of alumina against alumina and a constant specific wear rate can be observed for alumina sliding against zirconia [5].

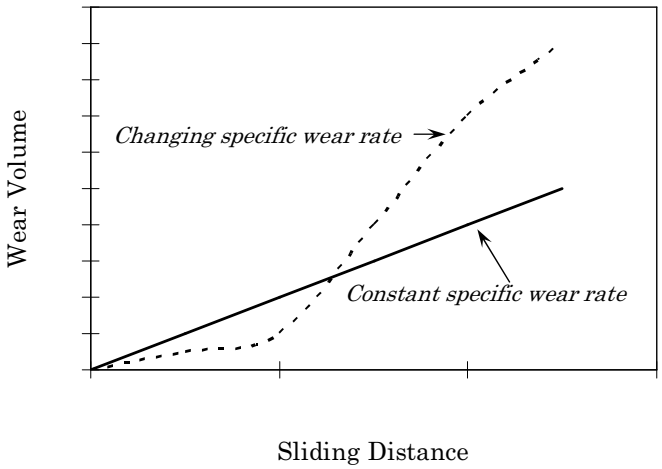

Figure 1.7: Specific wear rate of dry sliding system.

For further information on friction and wear mechanisms, the reader is referred to Bowden and Tabor [7], Hutchings [8], and Rabinowicz [9].

1.3.3 Testing methods

Nowadays there are many experimental methods that can be used to study friction and wear of materials (see figure 1.8). In general, the methods are divided into two types: the symmetric arrangement, in which the two surfaces are symmetrically disposed (see figure 1.8, a and b) and the asymmetric arrangement (see figure 1.8, c (pin on disc), d (pin on ring), e (block on ring) and f (pin on flat)). For the same material, the wear rate of the two specimens tested using the symmetric arrangements are expected to give the same wear volume. For the asymmetric arrangement, which is more common, the two bodies, even when made of the same material, will show different wear rates. The contact types of the asymmetric arrangement can be conformal (figure 1.9 a & b) or counterformal (figure 1.9 c & d).

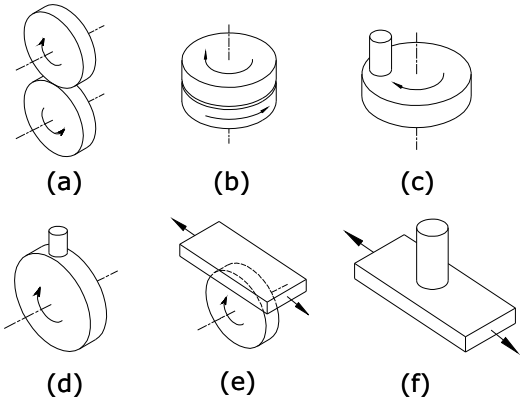

Figure 1.8: Sliding wear test arrangement.

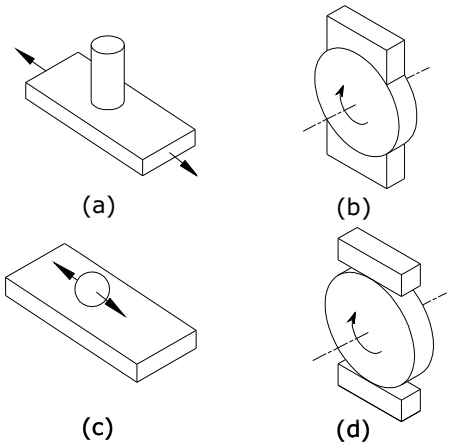

Figure 1.9: Conformal (a & b) and counterformal (c & d) contacts.

The specific wear rate (k) of the tested specimen is determined by measuring the weight of the specimen before (m_{bef}) and after the test (m_{af}). The weight difference ($m_{bef} - m_{af}$) divided by the density (ρ) gives the volume of the worn out material. So, since the load applied (P), the sliding distance (s) and the weight before (m_{bef}) and after (m_{af}) the test are known, then the specific wear rate of the tested specimen can be calculated as follow:

$$k = \frac{V_w}{Px} = \frac{\frac{m_{bef} - m_{af}}{\rho}}{Px} \qquad (1.5)$$

If the cross section profile of a wear track can be assumed to be uniform, the volume of the worn out material can also be calculated by multiplying the cross section area of the wear track times the length of the wear track.

1.4 Friction and wear of ceramics

As mentioned before, ceramics exhibit high friction and high wear when used as sliding components in machines [3, 11]. For dry sliding contact applications, the chosen material combination should be wear resistant ($k < 10^{-6} mm^3 N^{-1} m^{-1}$) and should reveal low friction ($f < 0.2$). In addition, the values of the coefficient of friction and the wear rate should not depend on the operating conditions, especially velocity and temperature [13].

Compared to metals and polymers, ceramics have some advantages and disadvantages with respect to tribological characteristics (see table 1.3). Ceramics have high hardness and high elasticity and therefore, for the same load and the same geometry of the contacting bodies, ceramics will show a smaller contact area compared to metals and polymers. The smaller contact area will result in a higher contact pressure and higher friction induced temperature but less wear due to adhesion. The high contact pressure and friction induced temperature will generate stresses in the contacting surfaces. If pores at the surface are subject to these high stresses, crack propagation might occur leading to grain pull-out, resulting in wear debris. The wear debris trapped in the system, which are hard, may cause a three body abrasive system resulting in a rougher rubbing surface and consequently a higher friction [14-18]. As a result, a sudden change in the value of the coefficient of friction and a change in the wear rate will also occur. Therefore, it should be possible to predict the maximum operating conditions (normal load and sliding velocity) on which dry sliding ceramic systems can operate safely without a significant amount of wear (mild wear). The prediction of the crack growth, by which one can determine the maximum load - velocity regime for the designed ceramics dry sliding system, will be discussed in chapter 2 of this thesis.

Table 1.3: Tribological characteristics in relation to the types of materials [13].

Mass density	$\rho_{polymer} < \rho_{ceramics} < \rho_{metal}$
Hertzian pressures	$p_{polymer} < p_{metal} < p_{ceramics}$
Friction-induced temperature increase	$\Delta T_{metal} < \Delta T_{polymer} < \Delta T_{ceramics}$
Adhesion energy	$Ad_{polymer} < Ad_{metal} < Ad_{ceramics}$
Abrasion	$Ab_{ceramics} < Ab_{metal} < Ab_{polymer}$
Tribochemical reactivity	$R_{polymer}, R_{ceramics} < R_{metal}$

1.4.1 Friction and wear of oxide ceramics at room temperature

At room temperature, oxides ceramics (Al_2O_3 and ZrO_2) exhibit high friction ($f \approx 0.5$-0.9,) and a varying specific wear rate ($k \approx 10^{-7} - 10^{-4}$ $mm^3N^{-1}m^{-1}$) depending on the applied normal load and sliding velocity [5, 10, 11, 13, 19, 20]. The friction and wear of zirconia at high contact pressure and high sliding velocity is too high ($f > 0.6$, $k > 10^{-5}$ $mm^3N^{-1}m^{-1}$) and not acceptable for many applications, especially for medical applications [21], while alumina shows very little wear at moderate pressure.

The grain size of ceramics influences their wear characteristics [20] as well as their mechanical and thermal properties. Therefore, the grain size of ceramics is an important parameter to improve the wear characteristics of ceramics in dry sliding system. By the right processing technique, the grain size of zirconia ceramics can be reduced from several μm down to 100 nm resulting in a wear resistant ceramic material ($k<<10^{-6}$ $mm^3N^{-1}m^{-1}$) [11]. He [11] tested zirconia with various grain sizes and observed that reducing the grain size improves the wear resistance of zirconia significantly (see figure 1.10).

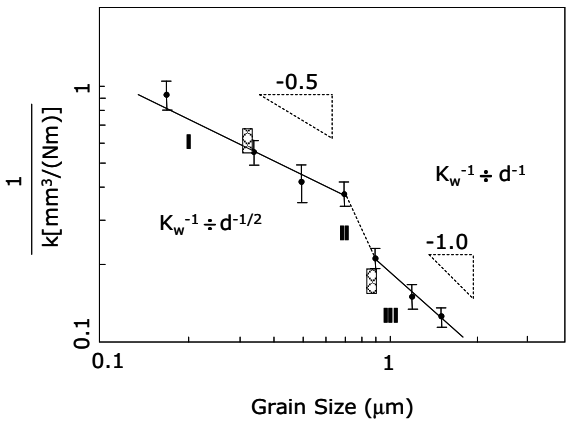

Figure 1.10: Specific wear rate of zirconia as a function of grain size [18].

Besides the grain size of the ceramics, the material of the counter-body also determines the level of friction and wear of oxides ceramics. Self-mating couples of zirconia against zirconia and alumina against alumina usually reveal high friction and high wear. This might be due to the strong adhesion forces between similar materials. It was shown by Morita et al. [21] (and later in chapter 3 in this thesis) that the combination of alumina sliding against zirconia shows lower wear and lower friction compared to a zirconia/zirconia sliding system.

The composite of alumina and zirconia might be promising. Adding zirconia into alumina will result in a zirconia toughened alumina (ZTA) composite. This idea was implemented by Kerkwijk [10]. Kerkwijk showed that the composite of 85 % alumina and 15 % zirconia is extremely wear resistant ($k < 10^{-9}$ $mm^3N^{-1}m^{-1}$). Many machine components [22] and medical applications [23, 24] use the composite of alumina and zirconia for its wear resistance characteristics. However, this material still exhibits high friction ($f > 0.5$).

1.4.2 Influence of humidity and water on friction and wear of oxide ceramics

The presence of moisture can give a significant change in the friction and wear of oxide ceramics. Alumina can react with the moisture forming a hydroxide layer [25]. Eventually the hydroxide layer is beneficial to reduce friction if the formation and the wearing out of the layer are stable. However, at high pressure and high sliding velocity, friction causes an increase in temperature. A high contact temperature will accelerate the formation of the hydroxide layer and at a certain critical thickness, this protective layer will be delaminated from the surface and consequently significant wear occurs in the system [25-28]. This kind of phenomenon is also observed at non-oxide sliding ceramic couples [27, 28]. The sliding test of self mated silicon nitride and silicon carbide systems, for instance, shows a low friction ($f < 0.2$) in water. The low friction is achieved by the presence of a silica layer that provides easy shear in the contact [27]. The load and the velocity as well as the surrounding temperature determines the lifetime of the interfacial layer and once the thickness of the silica layer reaches the critical thickness, the friction and wear becomes high again due to the rougher surface as the result of the delamination of the layer.

The friction of alumina is reduced from 0.6 to 0.4 by increasing the relative humidity from 0 % RH to 90 % RH. The specific wear rate is reduced from 10^{-7} $mm^3N^{-1}m^{-1}$ to 10^{-9} $mm^3N^{-1}m^{-1}$ when alumina slides against alumina at 0 % RH to 90 % RH [29]. In water, the coefficient of friction of self-mated alumina is about 0.3 and the specific wear rate is very low, 10^{-10} $mm^3N^{-1}m^{-1}$.

In contrast with zirconia, humidity does not have a significant influence on friction and wear. The coefficient of friction stays at a value of 0.6 and the wear rate is about 10^{-6} $mm^3N^{-1}m^{-1}$ for the whole humidity range of 0 % – 90 % RH [30]. In water, the coefficient of friction of self-mated zirconia is about 0.4 –

0.5 [19, 30]. The friction and wear of pure zirconia will also be discussed further in chapter 3 of this thesis.

At room conditions (23°C and 45 % RH), Ajayi and Ludema [31] observed the formation of transfer films in continuously sliding systems of alumina, zirconia, silicon nitride and silicon carbide combinations. Depending on the normal load and velocity, the coefficient of friction of these various sliding couples varied from 0.4 to 0.7.

1.4.3 Influence of temperature on friction and wear of oxide ceramics

At elevated temperatures, ceramics also reveal high friction (f = 0.4 – 0.9) and high wear rates (k = 10^{-6} $mm^3N^{-1}m^{-1}$ to 10^{-4} $mm^3N^{-1}m^{-1}$) depending on the temperature and the operating conditions (normal load and velocity) [33-36]. Various combinations of sliding couples (Al_2O_3/ ZrO_2, Al_2O_3/ SiC, Si_3N_4/ ZrO_2 and SiC / ZrO_2) were tested by Yust and Carignan [32] at room temperature and at elevated temperatures. Their experimental results showed that all the tested sliding couples revealed high wear (k > 10^{-6} $mm^3N^{-1}m^{-1}$). The wear tracks ware investigated and the authors [32] observed that the wear debris were entrapped and compacted in the wear track due to repeated sliding.

Sliding tests of alumina against alumina shows that the coefficient of friction increases from 0.4 to 0.82 as the temperature increases from room temperature to 600°C and decreased to a value of 0.4 at 800-1000°C [33]. By means of a series of experimental data, Dong et al. [33] proposed a wear map of self-mated alumina at elevated temperatures as shown in figure 1.11.

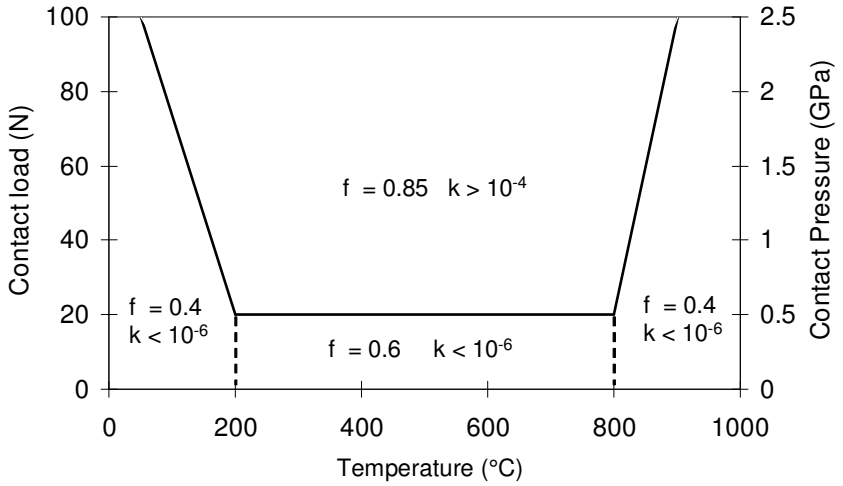

Figure 1.11: Wear map of self-mated alumina at elevated temperatures [33].

The coefficient of friction of self-mated zirconia at elevated temperatures is reported to be between 0.3 and 1 depending on the temperature and sliding velocity [34, 35]. The specific wear rate decreases from 10^{-6} $mm^3N^{-1}m^{-1}$ to 10^{-5} $mm^3N^{-1}m^{-1}$ as the temperature increases [35].

1.4.4 Friction and wear of oxide ceramics in vacuum

Hisakado and co-workers [37-39] investigated the friction and wear behaviour of ceramics against ceramics and metals in vacuum. The coefficient of friction of zirconia and alumina in vacuum increases from 0.5 to more than unity as the temperature increases (25 to 600°C). The specific wear rate also increases (10^{-7} to 10^{-4} $mm^3N^{-1}m^{-1}$) as the temperature increases. Again, ceramics reveal high friction and wear in vacuum.

1.4.5 Ceramics sliding against metal

When a ceramic is brought into sliding contact with a metal, strong adhesion will occur resulting in high friction and metal transfer to the ceramic material [40-42]. As the amount of metal transferred to the ceramic increases then the tribosystem of the ceramic-metal will change into a metal-metal tribosystem resulting in high friction and high wear [42]. The friction coefficient is reported to be about 0.4 to 1 depending on the type of ceramic and metal used as counter body and the operating conditions.

1.4.6 Concluding remarks and the objective of this thesis

The friction and wear of dry sliding contact of oxide ceramics in various environments (various humidities, high temperature and vacuum) are in general high. Only in some cases is wear found to be mild. Therefore, wear resistant and low friction oxide ceramics are needed. An attempt to make low friction oxide ceramics was carried out by Kerkwijk et al. [43] resulting in a patent of ceramics doped with CuO [44]. Under certain condition, the authors [43] showed that by adding copper oxide to alumina and zirconia ceramics the coefficient of friction was significantly reduced from 0.7 to 0.4.

The objective of this thesis is to carry out an investigation on the frictional behaviour of alumina and zirconia doped with CuO in the mild regime. The investigation was based on the principle that the presence of a soft interfacial (patchy) layer be responsible for reducing the friction. This investigation led also to the development of a contact and friction model of a layered surface that will be discussed further in this thesis.

1.5 Outline of this thesis

In this chapter, a review on friction and wear of oxide ceramics has been described. Chapter 2 reports the experimental results and a model for determining the range of the operating conditions (normal load and sliding velocity) as a function of the material properties at which sliding ceramic couples can operate safely, i.e. mild wear. In chapter 3, further investigation results on the friction and wear of oxides ceramics doped by CuO are described. The influence of humidity, water and temperature will be discussed. This chapter will also discuss the friction mechanism that is responsible for reducing the friction. In chapter 4, based on the observation described in chapter 3 that low friction in the ceramics doped with CuO is due to the presence of a soft interfacial layer, a general contact model is developed to predict the contact behaviour of a rough surface against a flat layered surface. Further, in chapter 5, the contact model is extended to a friction model. In chapter 6, the prediction of the coefficient of friction of zirconia doped with CuO sliding against alumina is presented based on the friction model presented in chapter 5 and the possible layer formation mechanism will be discussed in this chapter. Finally, conclusions and recommendations for future research are given in chapter 7.

The results of this investigation are reported in the literature [45-53].

References

[1] D.W. Richerson, The magic of ceramics, American Ceramic Society, 2000.
[2] Y. Liang and S.P. Dutta, Application trend in advanced ceramic technologies, Technovation 21 (2001) 61-65.
[3] K. Kato, Tribology of ceramics, Wear 136 (1990) 117-133.
[4] R.J. Brook, Concise encyclopedia of advanced ceramic materials, Pergamon Press, 1991.
[5] H.S.C. Metselaar, Thermally induced wear transition in ceramics, PhD Thesis, University of Twente, The Netherlands, 2001.
[6] F.P. Bowden and D. Tabor, Friction and lubrication of solids, Clarendon Press, Oxford, 1950.
[7] I.M. Hutchings, Tribology: friction and wear of engineering materials, Edward Arnold, 1992.
[8] E. Rabinowicz, Friction and wear of materials, John Wiley, 1965.
[9] N.P. Suh and N. Saka, Fundametals of tribology, MIT Press, 1978.
[10] B. Kerkwijk, Wear and friction of nanostructured zirconia and alumina ceramics and composites, PhD Thesis, University of Twente, The Netherlands, 1999.
[11] Y. He, Tribological and mechanical properties of fine-grained zirconia and zirconia-alumina ceramics, PhD Thesis, University of Twente, The Netherlands, 1995.
[12] J. Archard, Contact and rubbing of flat surfaces, Journal of Applied Physics 24(1953) 981-988.
[13] H. Czichos, H. Klaffke, E. Santner and W. Woydt, Advances in tribology: the materials point of view, Wear 190 (1995) 155-161.
[14] M.G. Gee, Wear testing and ceramics, Proceeding of the Institution of Mechanical Engineers, 208 (1994) 153-166.
[15] A.G. Evans and D.B. Marshall, Wear mechanisms in ceramics, in Fundamental of friction and wear of materials, edited by D.A. Rigney, ASM International, pp.439-452, 1981.
[16] K. Adachi, K. Kato and N. Chen, Wear map of ceramics, Wear 203-204 (1997) 291-301.
[17] Y.S. Wang, C. He, B.J. Hockey, P.I. Lacey and S.M. Hsu, Wear transitions in monolithic alumina and zirconia-alumina composites, Wear 181-183 (1995) 156-164.
[18] H.S.C. Metselaar, B. Kerkwijk, E.J. Mulder, H. Verweij and D.J. Schipper, Wear of ceramics due to thermal stress: a thermal severity parameter, Wear 249 (2002) 962-970.
[19] G.W. Stachowiak and G.B. Stachowiak, Environmental effects on wear and friction of toughened zirconia ceramics, Wear 160 (1993) 153-162.
[20] K.-H. Zum Gahr, Modeling and microstructural modification of alumina ceramic for improved tribological properties, Wear 200 (1996) 215-224.
[21] Y. Morita, K. Nakata and K. Ikeuchi, Wear properties of zirconia/alumina combination for joint prostheses, Wear 254, (2003) 147-153.

[22] C. Kaya and E. G. Butler, Zirconia-toughened alumina ceramics of helical spring shape with improved properties from extruded sol-derived pastes, Scripta Materialia 48 (2003) 359-364.
[23] S. Deville, J. Chevalier, G. Fantozzi, J. F. Bartolomé, J. Requena, J. S. Moya, R. Torrecillas and L.A. Díaz, Low-temperature ageing of zirconia-toughened alumina ceramics and its implication in biomedical implants, Journal of the European Ceramic Society 23 (2003) 2975-2982.
[24] B.I. Ardlin, Transformation-toughened zirconia for dental inlays, crowns and bridges: chemical stability and effect of low-temperature aging on flexural strength and surface structure, Dental Materials 18 (2002) 590-595.
[25] M.G. Gee, The formation of alumina hydroxide in the sliding wear of alumina, Wear 153 (1992) 201-227.
[26] T.F.J. Quinn, Review of oxidational wear, Part I : The origins of oxidational wear, Tribology International 16 (1983) 257-271.
[27] T.F.J. Quinn, Review of oxidational wear; Part II : Recent developments and future trends in oxidational wear research, 16, 6 (1983) 305-315.
[28] J. Xu and K. Kato, Formation of tribochemical layer of ceramics sliding in water and its role for low friction, Wear 245 (2000) 61-75.
[29] S. Sasaki, Tribochemistry in friction and wear of ceramics, Japanese Journal of Tribology 36 (1991) 699-707.
[30] S. Sasaki, Effects of environment on friction and wear of ceramics, Bulletin of Mechanical Engineering Laboratory, Japan, 1992.
[31] O.O. Ajayi and K.C. Ludema, Mechanism of transfer film formation during rapeat pass sliding of ceramic materials, Wear 140 (1990) 191-206.
[32] C.S. Yust and F.J. Carignan, Observations on the sliding wear of ceramics, ASLE Transactions 28, 2 (1984) 245-252.
[33] X. Dong, S. Jahanmir and S.M. Hsu, Tribological characteristics of α-alumina at elevated temperatures, Journal of American Ceramic Society. 74 (1991) 1036-1044.
[34] M. Woydt and K.-H Habig, High temperature tribology of ceramics, Tribology International 22 (1989) 75-87.
[35] G.W. Stachowiak and G.B. Stachowiak, Unlubricated wear and friction of toughened zirconia ceramics at elevated temperatures, Wear 143 (1991) 277-295.
[36] S. Jahanmir, Wear Transitions and tribochemical reactions in ceramics, Proceeding of the Institution of Mechanical Engineers, 217 (2002) 371-383.
[37] T. Hisakado and H. Tani, Effects of elevated temperature and topographies of worn surfaces on friction and wear of ceramics in vacuum, Wear 224 (1999) 165-172.
[38] T. Hisakado and K. Akiyama, Mechanisms of friction and wear of metals against ceramics in vacuum, Wear 224 (1999) 274-281.
[39] T. Hisakado and N. Hashizume, Effects of normal loads on the friction and wear properties of metals and ceramic against cermet in vacuum, Wear 237 (2000) 98-106.

[40] K. Miyosi, Fundamental considerations in adhesion, friction and wear for ceramic-metal contacts, Wear 141 (1990) 35-44.
[41] T. Hisakado, H. Suda and H. Watanabe, The friction and wear mechanisms between ceramics and metals, Wear 155 (1992) 251-268.
[42] Y.J. He, A.J.A. Winnubst, D.J. Schipper, P.M.V. Bakker, A.J. Burggraaf and H. Verweij, Friction and wear behavior of ceramic-hardened steel couples under reciprocating sliding motion, Wear 184 (1995) 33-43.
[43] B. Kerkwijk, M. García, W.E. van Zyl, A.J.A. Winnubst, E.J. Mulder, D.J. Schipper and H. Verweij, Friction behaviour of solid oxide lubricants as second phase in Al_2O_3 and stabilised ZrO_2 composites, Wear 256, (2004) 182-189.
[44] B. Kerkwijk, M. García, E.J. Mulder, D.J. Schipper and H. Verweij, Patent Int. Appl. WO 2001017926 A1, 2001.
[45] H.R. Pasaribu, J.W. Sloetjes and D.J. Schipper, Friction reduction by adding copper oxide into alumina and zirconia ceramics, Wear 255 (2003) 699-707.
[46] H.R. Pasaribu, J.W. Sloetjes and D.J. Schipper, The transition of mild to severe wear of ceramics, Wear 256 (2004) 585-591.
[47] A.J.A. Winnubst, S. Ran, K.W. Wiratha, D.H.A. Blank, H.R. Pasaribu, J.W. Sloetjes and D.J. Schipper, A wear-resistant zirconia ceramic for low friction applications, Key Engineering Materials, Vol. 264-268 (2004) 809-812.
[48] H.R. Pasaribu and D.J. Schipper, Deterministic contact model of a rough surface against a flat layered surface, Proceeding of 2004 ASME/STLE joint Tribology Conference, TRIB2004-64014.
[49] H.R. Pasaribu and D.J. Schipper, Application of a deterministic contact model to analyse the contact of a rough surface against a flat layered Surface, Accepted for publication in ASME Journal of Tribology, 2005.
[50] H.R. Pasaribu and D.J. Schipper, Deterministic friction model of a rough surface sliding against a flat layered surface, Tribology Letters Vol. 17 (2004) 967-976.
[51] H.R. Pasaribu, J.W. Sloetjes, D.J. Schipper, S. Ran, K.W. Wiratha, A.J.A. Winnubst and D.H.A. Blank, Wear-resistant CuO-doped zirconia ceramic with low friction, Extended abstract in the proceeding of International Symposium on Inorganic and Environmental Materials, October 18-21, 2004, Eindhoven, The Netherlands.
[52] H.R. Pasaribu, J.W. Sloetjes, D.J. Schipper and A.J.A. Winnubst, Nanoscale wear resistant and low friction oxide ceramics, Abstract in Proceeding of Material Research Conference, 22-23 May 2003, Veldhoven, the Netherlands.
[53] H.R. Pasaribu, K.M. Reuver, D.J. Schipper, S. Ran, K.W. Wiratha and A.J.A. Winnubst, Friction and wear characteristic of Zirconia doped with CuO, Submitted for publication to Journal of Refractory Metals and Hard Materials, 2005.

Chapter 2
The Transition from Mild to Severe Wear of Ceramics

2.1 Introduction

Ceramics will experience wear when used as components in dry sliding systems. Depending on the operating conditions (normal load, velocity and temperature) and material properties (grain size, mechanical and thermal properties), the wear of ceramics can be mild or severe. Mild wear is indicated by a very small amount of material loss, and a mild wear track looks smooth as a result of a running-in process. Severe wear can be recognized by a rough wear track and a lot of material loss. Severe wear should be avoided because it often quickly leads to system failure. Therefore, an engineer needs to know the operating conditions applicable to a ceramic material combination in order to operate safely, i.e. so that no severe wear takes place.

Many wear maps were proposed to predict wear of ceramics [1-3]. Most of the proposed wear maps were constructed by plotting the experimental results as a function of the operational conditions (normal load, sliding velocity or temperature). For example, Dong et al. [1] introduced a wear map of α-alumina ceramics as a function of normal load and temperature, while Hsu and co-workers [2, 3] introduced wear maps of various ceramics as a function of normal load and velocity. Unfortunately, Dong et al. [1] and Hsu & co-workers [2, 3] did not give any direct relation between the operating conditions and material properties with the type of wear experienced by ceramics under dry sliding conditions.

Adachi et al. [4] introduced a relation between the operating conditions (normal load or velocity) and material properties to determine the wear type of dry sliding ceramic systems. They proposed a non-dimensional wear map for sliding circular contacts which was derived based on the maximum tensile stress needed to initiate propagation of pre-existing cracks in the surface. For a sliding circular contact, the maximum tensile stress induced by mechanical loading (normal force and firction force) was calculated by Adachi et al. [4] based on the work of Hamilton [5] and the thermal stress due to frictional heating was determined based on the maximum temperature rise in a dry sliding contact as proposed by Ashby et al. [6]. By inserting, separately, the maximum tensile stress due to mechanical loading or thermal loading into the linear fracture mechanics for crack growth (see section 2.2), Adachi et al. [4] defined a non-

dimensional mechanical severity parameter ($S_{c,m}$) and a non-dimensional thermal severity parameter ($S_{c,t}$). If the calculated values of the severity parameters of a ceramic sliding circular contact exceed a critical value, the wear type is predicted to be severe wear and vice versa. This model was validated experimentally by testing ceramics against itself to simplify the heat partitioning problem which is not covered by the model of Ashby et al. [6]. As a consequence, this model is limited to self-mated ceramic contacts.

Metselaar et al. [7] improved the model of Adachi et al. [4] by introducing a new thermal severity parameter in which the heat partitioning problem was taken into account. Metselaar et al. [7] used the analytical solution proposed by Bos [8] to calculate the maximum temperature rise in a sliding circular contact which was further used to calculate the tensile stress at a crack tip due to frictional heating. Following the procedure introduced by Adachi et al. [4], Metselaar et al. [7] derived a new thermal severity parameter, Ξ. The new thermal severity parameter enables one to use the model for various combinations of ceramic sliding couples. The experimental results performed by Metselaar et al. [7] show that the new thermal severity parameter improved the prediction of wear transition of ceramics under conditions in which the wear is dominated by thermally induced wear.

The model of Adachi et al. [4] and Metselaar et al. [7] were used to predict the type of wear in dry sliding ceramic systems for the condition in which the wear is dominated by mechanically induced wear (high contact pressure but very low sliding velocity) or for conditions in which wear is dominated by thermally induced wear (low contact pressure but high sliding velocity). These models therefore overestimate the wear type of dry sliding ceramic systems operating at a moderate pressure and a moderate sliding velocity in which wear is induced by both mechanical loading and thermal loading at the same time.

In this chapter, the derivation of mechanical and thermal severity parameters of circular sliding contact introduced by Adachi et al. [4] and Metselaar et al. [7] will be revisited and generalized to elliptical and line contacts. Further, a combined mechanical and thermal severity parameter for a certain condition (Peclet number, P_e, higher than 2) will be introduced. The combined mechanical and thermal severity parameter will enable one to predict the mild to severe wear transition of ceramics for the condition in which mechanically and thermally induced wear occurs almost equally. Experimental validation of the combined mechanical and thermal severity parameter will also be reported and discussed in this chapter.

2.2 Mechanical and thermal severity parameter

2.2.1 Crack growth

During the processing of ceramics, imperfections like grain boundary cracks in the material and at the surface cannot be avoided. Mechanical and thermal loading will introduce stresses at the crack tip. If these stresses are high

enough, crack propagation along the grain boundary will occur and most probably the propagated crack will end up at the surface resulting in wear debris. The wear debris can be entrapped in the wear track which may cause three-body abrasive wear that make the surface rougher, i.e. severe wear occurs. So, the operating condition that initiates the crack to grow, leading to severe wear, is defined as the criterion to determine the wear type of ceramics.

For the analysis of crack growth, it is assumed that:

- Pre-existing micro-cracks at the grain boundary are the necessary requirements for micro-crack propagation. Their length is proportional to the grain size.

- Inter-granular fracture is caused by the propagation of these micro-cracks, which may be enhanced by friction.

Based on these assumptions, the fracture mechanism model can be used. The critical condition for crack growth to occur then can be expressed by the following equation [9]:

$$Y\sigma_{max}\sqrt{\pi d} \geq K_{IC} \tag{2.1}$$

in which σ_{max} is the maximum tensile stress at the tip of the crack, d is the pre-existing crack length, K_{IC} is the fracture toughness, and Y is a dimensionless constant that depends on the crack geometry [9].

For ceramics, the existence of tensile stresses is more important for yield than the value of the maximum shear stress. Therefore, in the following section, the calculation of maximum tensile stress for a sliding circular, elliptical and line contact will be outlined. Further, by inserting the maximum tensile stress into equation (2.1), a non-dimensional mechanical and thermal severity parameter will be derived.

2.2.2 Mechanical severity parameter

In practice, the shape of the contact area of curved bodies can be circular, elliptical or even a line (strip) (see figure 2.1). A circular contact can be observed in the contact of a spherical capped follower with the flat part of a cam. An elliptic contact can be seen in the contact of a ball with the inner and outer rings of a ball bearing and a line contact can be observed in the contact between spur gears (see figure 2.1).

Hertz [10] introduced the solution to calculate the deformation, the contact area and the contact pressure of circular contact. Further, Hertz's solutions were extended for the case of elliptical and line contacts [11-13]. A summary of Hertzian solutions for circular, elliptical and line contacts is given in appendix A.

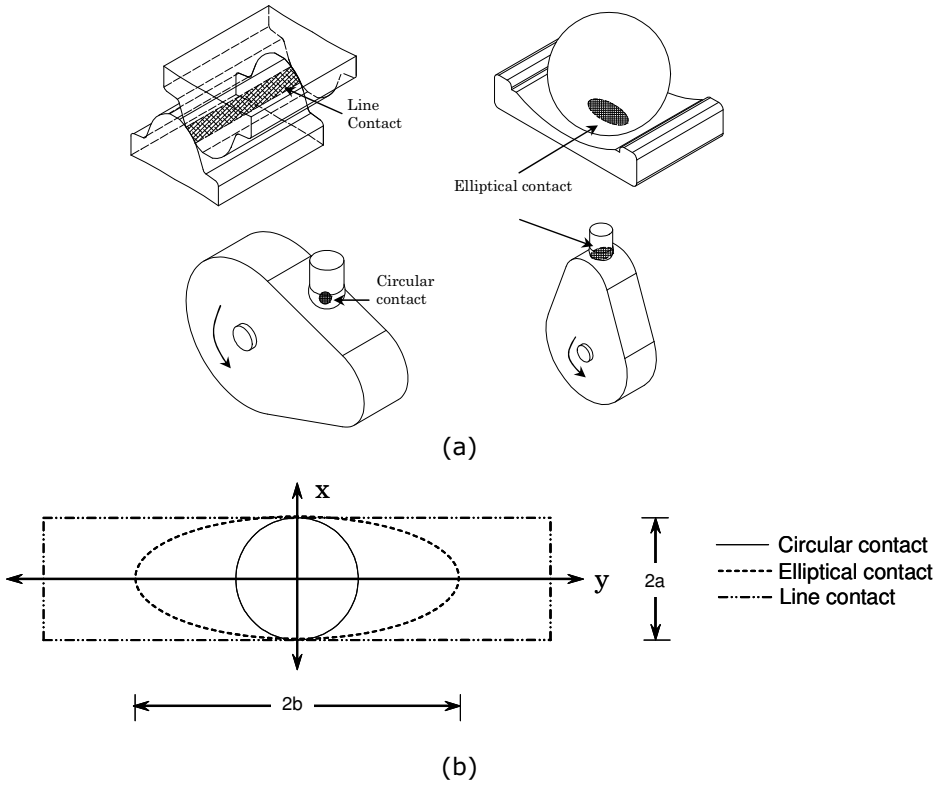

Figure 2.1: Circular, elliptical and line contacts, (a) physical condition and (b) the shape of the contact area.

Hamilton [5] derived a closed form formula to calculate the stress field beneath a sliding circular contact. According to Hamilton [5] the maximum tensile stress occurs at the circumference of the contact (see figure 2.2). The effect of friction is to add a compressive stress to the leading edge of the contact and to intensify the tensile stress at the trailing edge. This maximum tensile stress ($\sigma_{m,C}^{mech}$) is given by:

$$\sigma_{m,C}^{mech} = P_o\left[\frac{1-2v}{3} + \frac{4+v}{8}\pi f\right] \qquad (2.2)$$

in which P_o is the maximum Hertzian pressure (see appendix A), v is Poisson's ratio and f is the coefficient of friction.

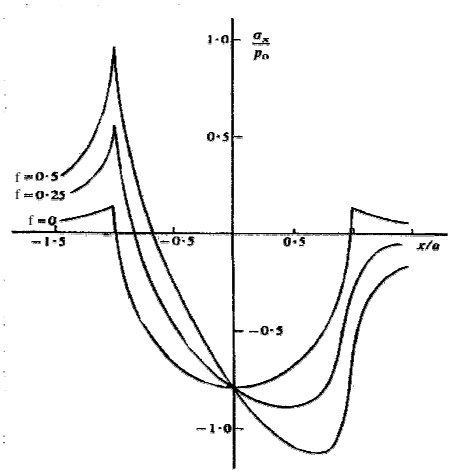

Figure 2.2: The distribution of the stress (σ_x) at the surface for a range of the coefficient of friction [5].

The stress field beneath a sliding elliptical contact was derived by Sackfield and Hills [14]. They also observed that the maximum tensile stress occurs at the trailing edge of the contact. Suppose the direction of sliding is parallel to the x-axis (see figure 2.1), the maximum tensile stress due to normal loading ($\sigma_{P,E}$) at the trailing edge of a sliding elliptical contact can be calculated as:

$$\sigma_{P,E} = \begin{cases} P_o(1-2v)\dfrac{k}{e^2}\left(1-\dfrac{k}{e}\tan^{-1}\left(\dfrac{e}{k}\right)\right) & \text{, if } a \le b \\ P_o(1-2v)\dfrac{k}{e^2}\left(\dfrac{1}{e}\tanh^{-1}(e)-1\right) & \text{, if } b \le a \end{cases} \tag{2.3}$$

with:

$$k = \frac{a}{b} \tag{2.4}$$

$$e = \begin{cases} \left(1-k^2\right)^{0.5} & ; \quad \text{if} \quad b > a \\ \left(1-\dfrac{1}{k^2}\right)^{0.5} & ; \quad \text{if} \quad a > b \end{cases} \tag{2.5}$$

where a and b are respectively the minor and major axes of the contact ellipse (see figure 2.1), e is the eccentricity and P_o is the maximum Hertzian pressure for elliptical contact (see appendix A). In the presence of friction, the tensile

stress due to friction ($\sigma_{f,E}$) at the trailing edge of a sliding elliptical contact can be calculated as (Sackfield and Hills [14]):

$$\sigma_{f,E} = \frac{-2fkP_o}{e^2}\left[\left(e^2 + v\right)I_1 - vk^2 I_2\right] \tag{2.6}$$

where I_1 and I_2 are the elliptical integrals defined as:

$$I_1 = \int_0^\infty \frac{dw}{\left(1 + w^2\right)^{3/2}\left(k^2 + w^2\right)^{1/2}} \tag{2.7}$$

$$I_2 = \int_0^\infty \frac{dw}{\left(1 + w^2\right)^{1/2}\left(k^2 + w^2\right)^{3/2}} \tag{2.8}$$

So the total maximum tensile stress at the trailing edge of a sliding elliptical contact ($\sigma_{m,E}^{mech}$) due to normal loading and tangential loading can be calculated as:

$$\sigma_{m,E}^{mech} = \sigma_{f,E} + \sigma_{P,E} \tag{2.9}$$

For a line contact, the maximum tensile stress due to normal loading and tangential loading ($\sigma_{m,L}^{mech}$) was derived by Johnson [11]:

$$\sigma_{m,L}^{mech} = 2\,f\,P_o \tag{2.10}$$

The calculation of the tensile stress (σ_{max}^{mech}) at the trailing edge of a circular, elliptical or line contact, can in fact, be written in a general equation as the summation of the tensile stress due to normal loading and the tensile stress due to tangential loading for an elliptical contact:

$$\sigma_{max}^{mech} = P_o\left((1 - 2v)\,C_1 + fC_2\right) \tag{2.11}$$

where P_o is the maximum Hertzian contact pressure, f is the coefficient of friction, C_1 is a proportionality constant to calculate tensile stress at the trailing edge due to normal load and C_2 is a proportionality constant to calculate the tensile stress due to a tangential load. For a circular contact, equation (2.11) must yield to equation (2.2) by setting the ratio between the minor and major radii (see equation (2.4)) equal to unity, whereas for line contact, equation (2.2) must yield to equation (2.10) by setting the ratio of the minor and major radii to zero or infinity. Therefore, C_1 in equation (2.11) can be defined based on equation (2.3) as:

$$C_1 = \begin{cases} \dfrac{k}{e^2}\left(1 - \dfrac{k}{e}\tan^{-1}\left(\dfrac{e}{k}\right)\right) & \text{, if } a \le b \\ \dfrac{k}{e^2}\left(\dfrac{1}{e}\tanh^{-1}(e) - 1\right) & \text{, if } b \le a \end{cases} \qquad (2.12)$$

The possible value of constant C_1 is shown in figure 2.3.

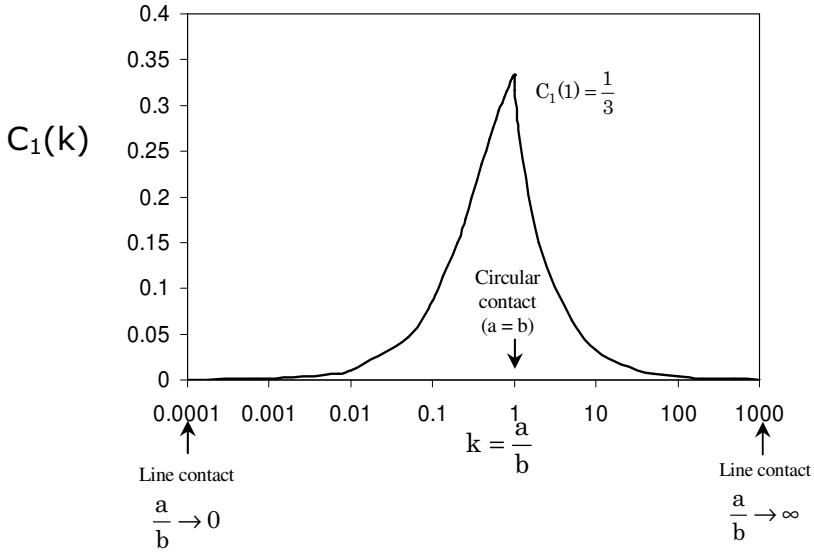

Figure 2.3: Constant C_1 as a function of the ratio between the minor axis and the major axis (a/b) of an elliptical contact.

The constant C_2 can be calculated using equation (2.6). As shown in figure 2.4 for different values of the Poisson's ratio, the value of C_2 does not vary much. Therefore, the value of C_2 can be calculated using equation (2.13) which was obtained by fitting the numerical results given by equation (2.6). The curve fitting equation can calculate the value of C_2 with an error less than 8 %.

$$\frac{\sigma_f}{fP_o} = C_2 = 2\tanh\left[\sinh^{-1}\left(\frac{7}{4}\left(\frac{a}{b}\right)^{\frac{5}{7}}\right)\right] \qquad (2.13)$$

Since the tensile stress at the trailing edge of the contact area can be calculated, one can find that by inserting equation 2.11 into equation (2.1), the crack will start to grow if the following equation is fulfilled:

$$M = \frac{P_o\left((1-2v)\,C_1 + fC_2\right)\sqrt{d}}{K_{IC}} \geq \frac{1}{Y\sqrt{\pi}} \tag{2.14}$$

where M is a dimensionless number defined as the mechanical severity parameter.

For a circular contact, using the assumption that the Poisson's ratio is 0.25, equation (2.2) can be simplified to:

$$\sigma_{max}^{mech} = \frac{3P}{2\pi a^2}\left[\frac{1+10f}{6}\right] \tag{2.15}$$

By substituting equation (2.15) into equation (2.1), Adachi et al. [4] defined the mechanical severity ($S_{c,m}$) of a sliding circular contact as follows:

$$S_{c,m} = \frac{3P\left(1+10f\right)\sqrt{d}}{2\pi a^2 K_{IC}} \geq C_m \tag{2.16}$$

in which $C_m = 6/\left(Y\sqrt{\pi}\right)$.

Consequently, the relation between the mechanical severity parameter defined by Adachi [4], $S_{c,m}$ and the general mechanical severity parameter (M) is:

$$M = \frac{S_{c,m}}{6} \tag{2.17}$$

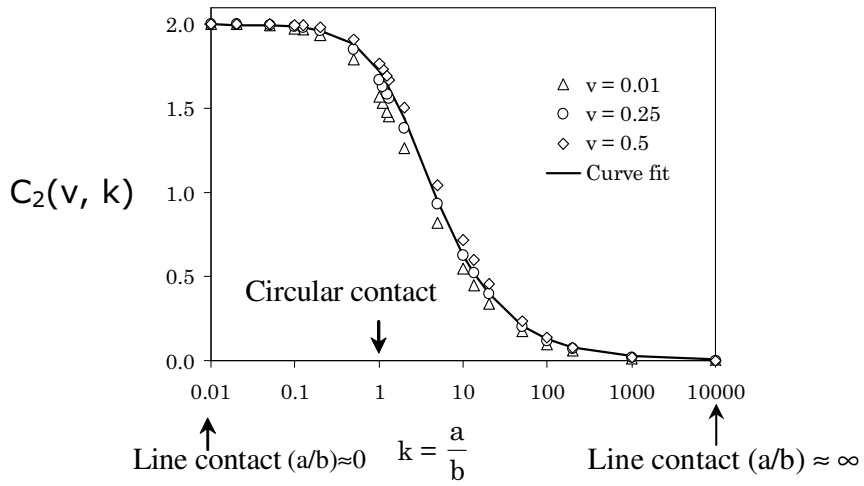

Figure 2.4: Constant C_2 as a function of the ratio between the minor axis (a) and the major axis (b).

2.2.3 Thermal severity parameter

When a sliding contact passes a spot on a stationary surface, the temperature on the surface will rise due to frictional heating, followed by rapid cooling down due to heat dissipation. The temperature rise will induce thermal strain and therefore compressive stress at the surfaces. While it is cooling down, a tensile stress will be induced in the surface. The maximum temperature rise due to frictional heating has been derived by Bos [8], resulting in:

$$\Delta T = \frac{fPV}{\sqrt{ab}} \frac{1}{\sum_i (K_i/\theta_i)} \tag{2.18}$$

where f is the coefficient of friction, P is the normal load, V is the sliding velocity, a and b are the minor and major axes respectively, K is the thermal conductivity, θ is the flash temperature number [8] and subscript i refers to the bodies in contact.

For sliding, where one of the contacted bodies is stationary and the other is moving, equation (2.18) can be written as [8]:

$$\Delta T = \frac{fPV}{\sqrt{ab}} \frac{1}{\frac{K_{mov}}{\theta_{mov}} + \frac{K_{sta}}{\theta_{sta}}} \tag{2.19}$$

with:

$$\theta_{mov} = \left[\{\theta_l S(\phi)\}^s + \left(\frac{\theta_r}{\sqrt{\phi P_{ei}}} \right)^s \right]^{\frac{1}{s}} \tag{2.20}$$

$$\theta_{sta} = \theta_l \tag{2.21}$$

and:

$$s = 0.5 \exp\left(1 - \frac{b}{a}\right) - 2.5 \tag{2.22}$$

$$P_{ei} = \frac{\rho c a V}{K_i} \tag{2.23}$$

$$\theta_r = 0.375 \qquad \theta_l = 0.589 \tag{2.24}$$

where s is the shape factor [8], P_e is the Peclet number, ρ is the density, c is the specific heat, θ_r and θ_l are constants obtained from numerical results performed by Bos [8].

For a circular contact, where a is equal to b, Metselaar et al. [7] defined:

$$\Delta T = \frac{fPV}{aK_{eff}} \tag{2.25}$$

in which $K_{eff} = 2.667[K_2+(K_1^2+0.4Va\rho_1c_1K_1)^{0.5}]$, K_{eff} is the effective thermal conductivity for a sliding circular contact. Next, the maximum stress due to this maximum temperature rise in the contact can be given by:

$$\sigma_{max}^{thermal} = \frac{E\alpha}{1-v}\Delta T \tag{2.26}$$

in which α is the thermal expansion coefficient and E is the elastic modulus. Substitution of equation (2.26) into equation 2.1 leads to:

$$\frac{\Delta T}{\frac{(1-v)K_{IC}}{E\alpha\sqrt{\pi d}}} \geq \frac{1}{Y} \tag{2.27}$$

The material properties in equation (2.27) can be related to the thermal shock resistance of the material with the following linear relation (see Adachi et al. [4]):

$$\Delta T_s = \Delta T_{so} + m\frac{(1-v)K_{IC}}{E\alpha\sqrt{\pi d}} \tag{2.28}$$

where m is a proportionality constant and ΔT_{S0} is an offset value. When $(1\text{-}v)K_{Ic}/[E\alpha(\pi d)^{0.5}] \rightarrow 0$, then the thermal shock resistance of the material $\Delta T_S \rightarrow 0$, and as a consequence $\Delta T_{S0} \approx 0$.

Combining equation (2.27) and equation (2.28), the thermal severity parameter (Γ) in general can be calculated as:

$$\Gamma = \frac{\Delta T}{\Delta T_S} \geq \left[\frac{1}{mY}\right] \tag{2.29}$$

For a circular contact (a = b), equation 2.29 can be written as [7]:

$$\Xi = \frac{fPV}{aK_{eff}\Delta T_S} \geq \left[\frac{1}{mY}\right] \tag{2.30}$$

where Ξ is the thermal severity parameter for a circular contact defined by Metselaar et al. [7].

2.3 Combined mechanical and thermal severity parameter

An analytical solution to determine the surface temperature distribution due to frictional heating is not available yet. However, numerical calculation shows that the maximum surface temperature due to frictional heating moves from the centre of the contact area, for Peclet number (P_e) equal to zero, to the trailing edge for higher Peclet numbers, say $P_e > 2$. This is based on the results presented by various authors [15-19].

So for P_e larger than 2, it can be assumed that the maximum temperature rise due to frictional heating occurs at the trailing edge of the contact area (see figure 2.5). Based on this assumption, the maximum tensile stress due to frictional heating and the maximum tensile stress due to mechanical loading (normal force and friction force) coincide at the trailing edge of the contact area. The total maximum tensile stress can be calculated as a summation of these maximum stresses. By using equation (2.1), the following expression can be derived for the crack growth due to a combined mechanical loading and thermal heating, using equations (2.11) and (2.26):

$$Y\sigma_{max}\sqrt{\pi d} \geq K_{IC}$$

$$Y\left\{\sigma_{max}^{mech} + \sigma_{max}^{Thermal}\right\}\sqrt{\pi d} \geq K_{IC}$$

$$Y\left\{P_o\left((1-v)C_1 + fC_2\right) + \frac{E\alpha}{(1-v)}\Delta T\right\}\sqrt{\pi d} \geq K_{IC}$$

$$M + \frac{m}{\sqrt{\pi}}\Gamma \geq \frac{1}{Y\sqrt{\pi}} \qquad (2.31a)$$

For a circular contact, equation (2.31a) can be expressed as:

$$Y\left\{\frac{3P}{2\pi a^2}\left[\frac{1+10f}{6}\right] + \frac{E\alpha\, fPV}{(1-v)aK_{eff}}\right\}\sqrt{\pi d} \geq K_{IC}$$

$$\frac{1}{6}S_{c,m} + \frac{m}{\sqrt{\pi}}\Xi \geq \frac{1}{Y\sqrt{\pi}} \qquad (2.31b)$$

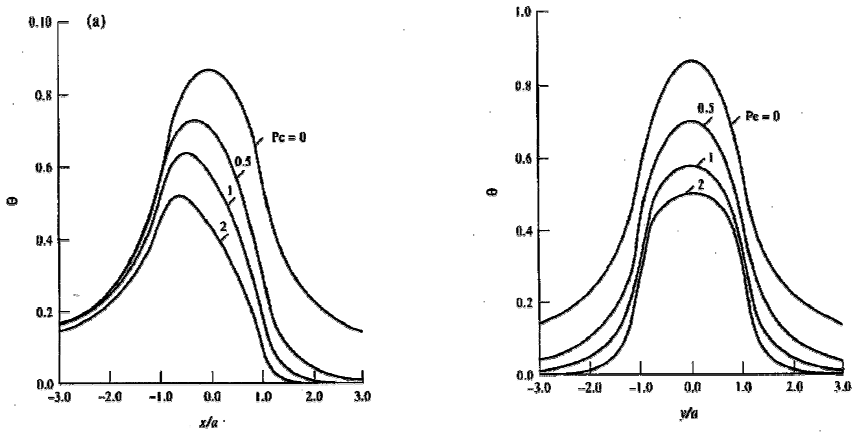

Figure 2.5: Dimensionless steady surface temperature distribution along the x-axis (moving direction) and along the y-axis (perpendicular to direction of motion of the frictional heat source) [16].

Based on experimental results, according to Adachi et al. [4], a mild to severe wear transition due to mechanical loading will occur at $S_{c,m} \approx 6$ and according to Metselaar et al. [7] mild to severe wear transition due to thermal loading will occur at $\Xi \approx 2.7$. Substitution of these results into equation (2.31b) and by using the value of Y = 0.71 [9] and c = 0.47 [7], one finds that severe wear will occur when the following expression is fulfilled:

$$2.7\,S_{c,m} + 6\,\Xi \geq 16.2 \tag{2.32}$$

2.4 Experimental procedure

To evaluate the transition from mild to severe wear of ceramic sliding circular contacts, experiments were performed on a pin-on-disc tribometer (see figure 2.6). The ball on disc geometry is chosen to avoid misalignment problems. The tribotester (CSEM, Switzerland) used for these experiments and the schematic setup of the pin on disc are shown in figure 2.6.

The disc is mounted on a holder that is driven by a motor. The motor is controlled by a controller connected to a personal computer, and by using built in software a user can determine the sliding velocity and the distance or the number of revolutions applied to the test. A ball shape counter body is mounted in a ball holder that is attached to a very stiff arm (see figure 2.6) in the normal direction which is held by two elastic joints. The friction force is obtained from the displacement experienced at the end of the elastic joints (see figure 2.6). The normal load is applied by placing a corresponding mass on top of the pin. In

order to obtain constant test conditions the tribometer was placed in a controlled environment with the temperature set at 23°C and the relative humidity at 40%.

Alumina ceramic was chosen as disc material for its high conductivity to be able to operate in the mild wear regime at high contact pressures and high Peclet numbers. They were made from commercially available, high purity α-alumina powder. In addition, discs made of zirconia doped with CuO, on which low friction was observed (will be explained later in chapter 3), were also tested. The discs had a diameter of 36 mm and a thickness of 4 mm. The discs were polished to a RMS value of less than 0.1 μm. Commercially available 10 mm diameter Al_2O_3, Y-TZP, Si_3N_4 and SiC balls were used as counter surface. Both discs and balls were cleaned ultrasonically in ethanol for 30 minutes and dried at 120°C prior to use. Properties of the ceramics used are listed in table 2.1. Velocities and loads used in the experiments are listed in table 2.2. Each test was carried out for 10 km sliding distance.

The surface topography of the specimens before and after each experiment was measured using the MicroMap interference microscope (ATOS, Germany). The principle of the apparatus is shown in figure 2.7. This apparatus operates on the bases of the white light interferometry imaging measurement technique. This technique allows the apparatus to instantly measure the topography of a surface.

This apparatus can be used to measure surface topography of a certain area and depending on the chosen magnification, the measured area ranges between 0.1×0.085 mm^2 to 4.42×3.45 mm^2. The measured surface is represented by 304×228 data points and the height resolution is better than 1 nm. The digital data provided by this apparatus allows the user to treat the data using a computer by which one can determine the radii and heights of the asperities of a measured surface which are parameters needed to calculate the contact between rough surfaces (see chapter 4).

Tabel 2.1: Properties of materials used.

			Disc		**Pin**			
Property	**Symbol**	**Unit**	**Al_2O_3**	**ZrO_2**	**Al_2O_3**	**ZrO_2**	**Si_3N_4**	**SiC**
Grain size	d	[μm]	1.8	0.18	6	4	na*	na*
Fracture Toughness	K_{IC}	[MPa.m$^{1/2}$]	3.5	7	3.5	10	8	4
Young's Modulus	E	[GPa]	390	210	390	210	320	430
Poisson's Ratio	v	[-]	0.23	0.3	0.23	0.31	0.24	0.17
Density	ρ	[kg/m^3]	3900	5700	3900	6050	3100	3200
Thermal Expantion Coeff.	α	[10^{-6}K^{-1}]	8	9	8	9.8	3	na*
Thermal Conductivity	K	[W/(m.K)]	29	2.5	29	3	35	110
Spesific Heat	c	[J/(kg.K)]	600	400	600	400	800	1000
Thermal Shock Resistance	ΔTs	[K]	200	280	200	250	600	380

* not available

Table 2.2: Velocities and loads used in the experiments

Pin	Velocity (m/s)	Load (N)	P_{max}(MPa)
Al_2O_3	0.35-0.85	2-20	870-1875
3Y-TZP	0.7-0.85	1-2	555-700
Si_3N_4	0.65-0.85	2-3	814-932
SiC	0.45-0.85	2-10	892-1524

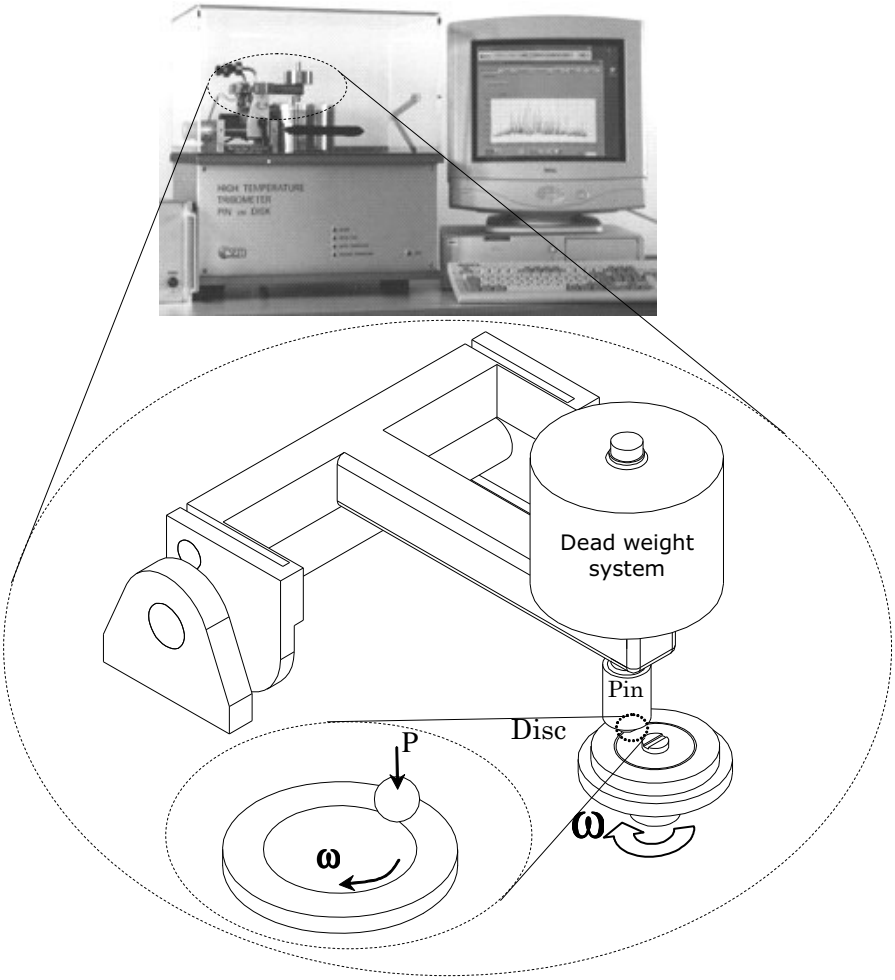

Figure 2.6: The pin-on-disc tribotester used in this thesis.

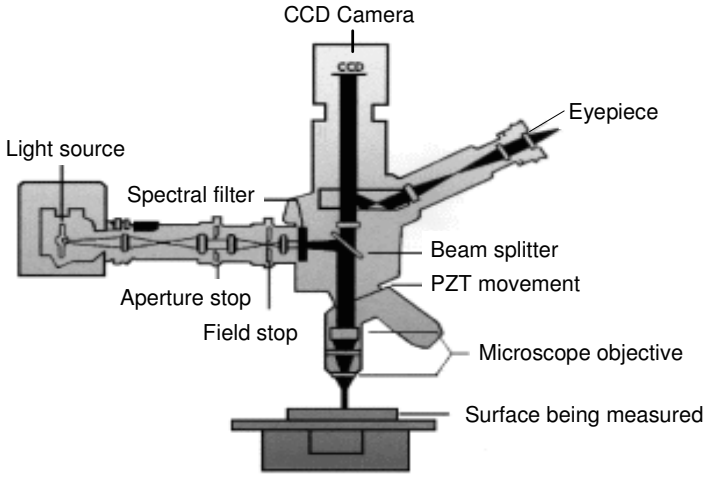

(a)

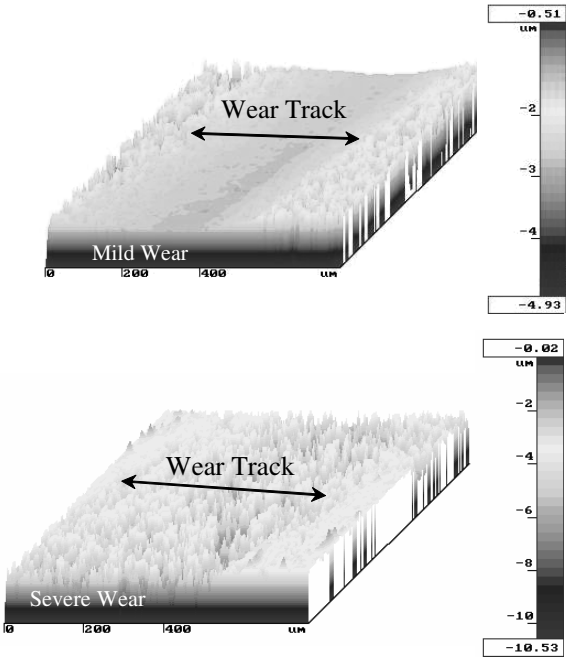

(b)

Figure 2.7: The principle of MicroMap measurement (a). Examples of measured surfaces (mild and severe wear) obtained by the MicroMap surface interferometer which are displayed in 3D view (b).

2.5 Results

2.5.1 Specific wear rate

For all the tests performed, both mild and severe wear, besides through the obtained specific wear rate (k), could be recognized easily by the naked eye. Mild wear always shows a shiny and smooth wear track as a result of running-in. Severe wear shows a rough surface accompanied by a lot of wear debris beside the wear track. Typical wear track profiles for mild and severe wear are shown in figure 2.8. Figure 2.9 shows the distribution of wear data for mild and severe wear of ceramics tested. It was found that severe wear will occur for a specific wear rate higher than 10^{-6} $mm^3N^{-1}m^{-1}$ [4] for the alumina disc and 3×10^{-6} $mm^3(N^{-1}m^{-1})$ [7] for the zirconia disc. Here, mild wear was defined when a relatively smooth wear track was formed with a specific wear rate less than $10^{-6}mm^3N^{-1}m^{-1}$ for the alumina disc and a specific wear rate less than 3×10^{-6} $mm^3N^{-1}m^{-1}$ for the zirconia disc while severe wear was defined when a rough wear track was formed with a specific wear rate larger than 10^{-6} $mm^3N^{-1}m^{-1}$ for the alumina disc and 3×10^{-6} $mm^3N^{-1}m^{-1}$ for the zirconia disc.

2.5.2 Wear map

Figure 2.10a shows the transition from mild to severe wear of ceramics on a logarithmic scale. The present experimental results are plotted together with data taken from Adachi et al. [4] and Metselaar et al. [7] as well as the transition defined by them (dotted lines). In addition, the experimental results on zirconia doped with CuO (see chapter 3) reported by Reuver [20] are also plotted. The combined mechanical and thermal severity parameter shows improvement in predicting the mild to severe wear transition of ceramics, particularly in the region in which the wear is induced by both mechanical loading and thermal loading. Figure 2.10b, in which the results are plotted on a linear scale, shows the improvement more clearly.

2.6 Discussions

A combined mechanical and thermal severity parameter for a Peclet number higher than 2 was introduced in this chapter. The transition from mild to severe wear is in good agreement with the experimental results. The experimental data taken from Adachi et al. [4] and Metselaar et al. [7] also fit to the improved transition boundary. Moreover, some results which it seemed could not be explained by their transition models now fit nicely with the improved transition boundary. Furthermore, this model is valid for various combinations of ceramics.

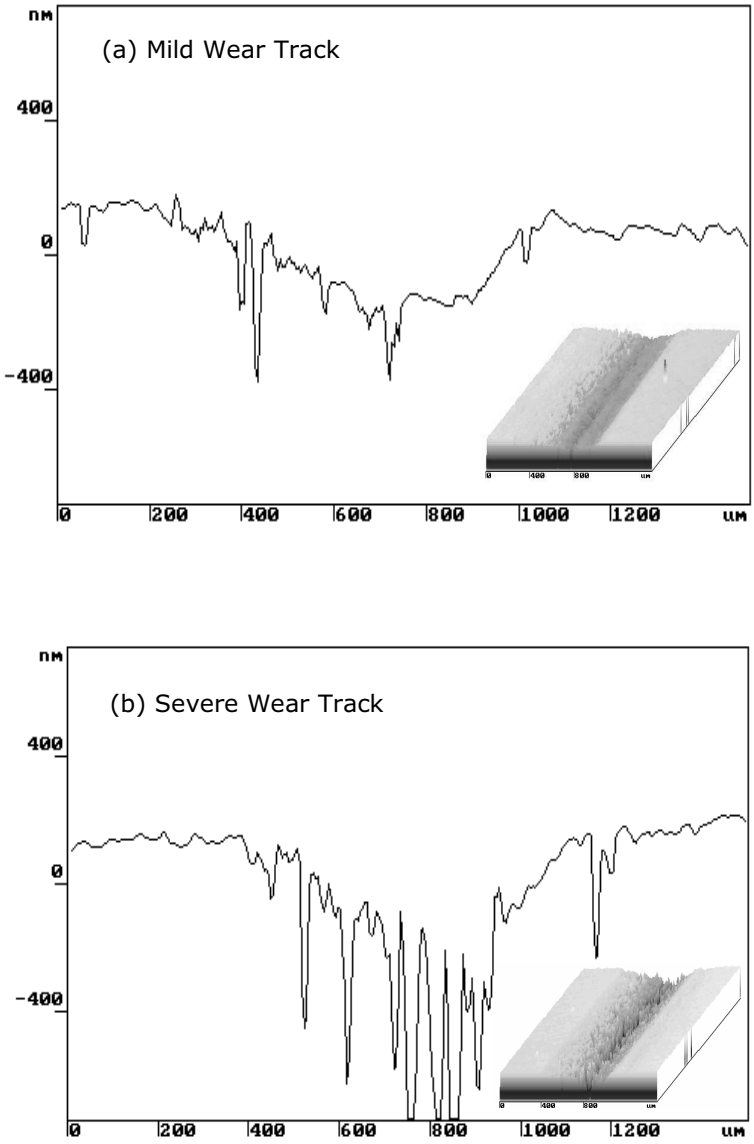

Figure 2.8: Cross-section profiles of (a) mild and (b) severe wear. (see also figure 2.7).

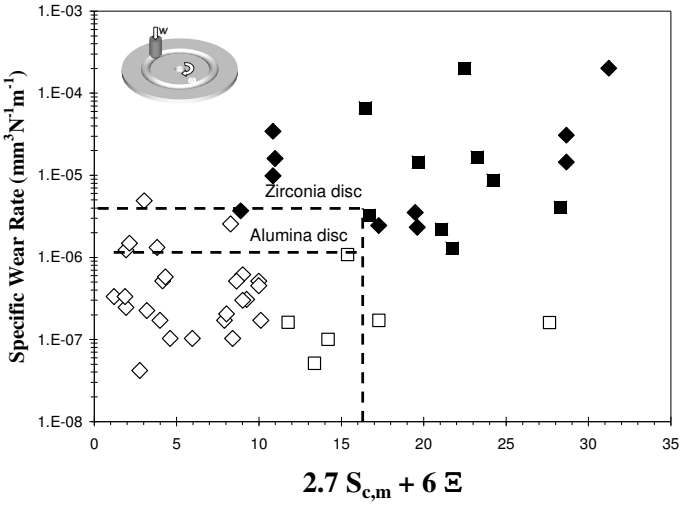

Figure 2.9: Specific wear rate determining mild and severe wear.

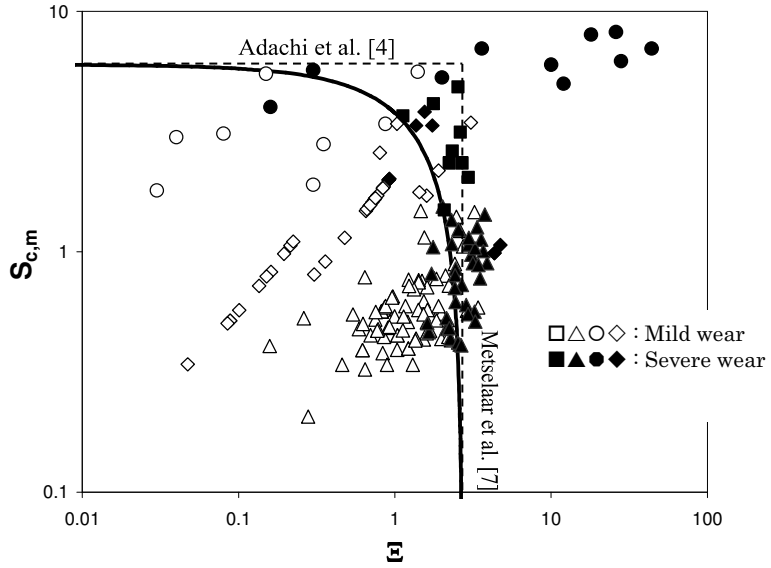

Figure 2.10a: Wear map of ceramics presented on logarithmic scale. Present experimental results: (□,■), Adachi et al. [4]:(○,●) Metselaar et al. [7]: (△,▲), and Reuver [20]: (◇,◆).

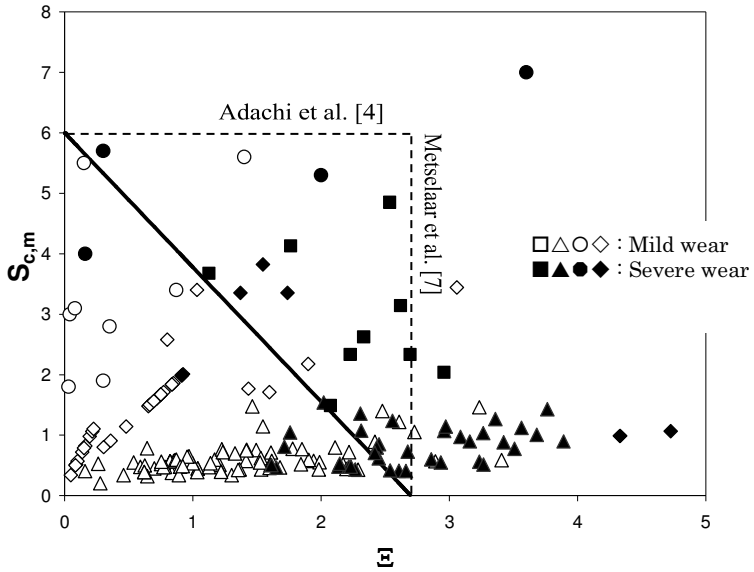

Figure 2.10b: Wear map of ceramics presented on linear scale. Present experimental results: (□,■), Adachi et al. [4]:(○,●) Metselaar et al. [7]: (△,▲), and Reuver [20]: (◇,◆).

As shown by the transition equation (equation (2.31)), the coefficient of friction has a significant influence in determining the wear type of the ceramic. Therefore, low friction ceramics are needed to extend operating conditions such as normal load (P) and velocity (V).

The influence of reducing friction on the extension of the operating conditions can be shown in the following example. Consider a 10 mm diameter alumina ball sliding against zirconia. The coefficient of friction of zirconia against various ceramics ranges from 0.55 to 0.85 depending on the normal load and the sliding velocity (see figure 2.11) [21]. Taking a coefficient of friction of 0.7, the maximum allowable normal load - sliding velocity regime for the system of 10 mm diameter ball (alumina or zirconia) sliding against a flat oxide ceramic can be calculated based on equation (2.31) and the properties given in table 1.1. This result is given in figure 2.12. The same calculations performed for a coefficient of friction of 0.2, is plotted in figure 2.12 (dotted line).

Figure 2.12, in which the mild to severe wear transition is given as a function of the coefficient of friction, clearly shows that the coefficient of friction is an important parameter that determines the maximum allowable normal load - sliding velocity regime.

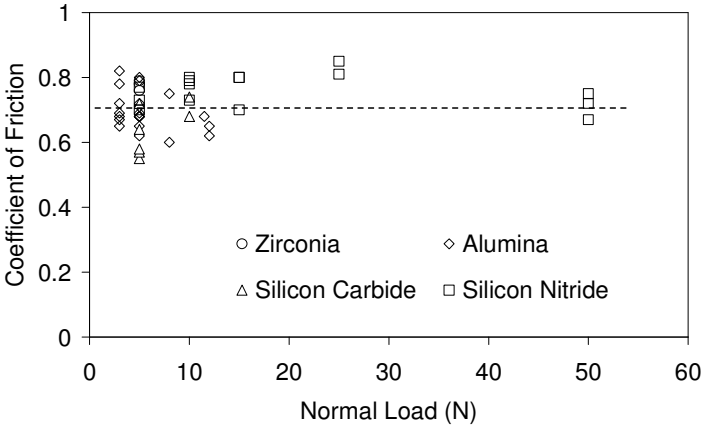

Figure 2.11: Coefficient of friction of as a function of normal load of zirconia sliding against various ceramics [21].

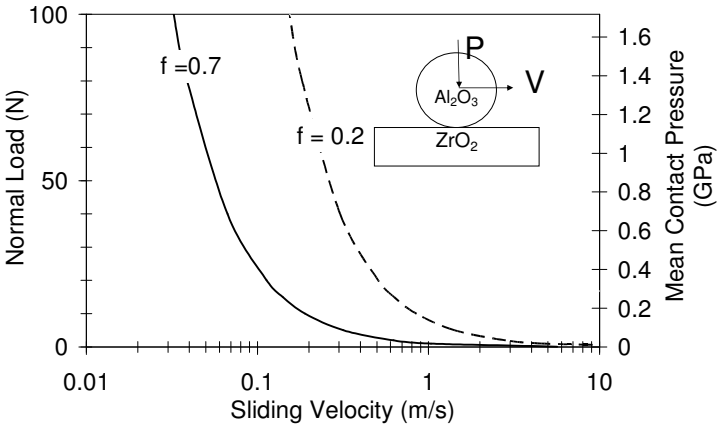

Figure 2.12: The maximum allowable normal load and velocity of 10 mm diameter alumina ball sliding against zirconia disc.

2.7. Concluding remarks

In this chapter, a relation between the operating conditions and the wear type (mild or severe) of ceramics has been discussed. The experimental results showed that the model can quite accurately predict the transition between the

region of mild and severe wear. With the proposed model, one can predict whether a sliding ceramic system will experience mild wear or severe wear.

In the following chapter, an attempt to reduce the friction of dry sliding ceramic systems will be presented.

References

[1] X. Dong, S. Jahanmir and S.M. Hsu, Tribological characteristics of α-alumina at elevated temperature, Journal of American Ceramic Society 74 (1991) 1036-1044.

[2] S.M. Hsu and M.C. Shen, Ceramic wear map, Wear 200 (1996) 154-175.

[3] S.M. Hsu, M.C. Shen, T.N. Ying, Y.S. Wang and S.W. Lee, Tribology of silicon ceramics, Ceramic Transactions 42 (1994) 189-205.

[4] K. Adachi, K. Kato and N. Chen, Wear Map of Ceramics, Wear 203-204 (1997) 291-301.

[5] G.M. Hamilton, Explicit equations for the stresses beneath a sliding spherical contact, Proceeding of the Institution of Mechanical Engineers 197C, 1983.

[6] M.F. Ashby, J. Abulawi and H. Kong, Temperature maps for frictional heating in dry sliding, Tribology Transactions (34) 577-587(1991).

[7] H.S.C. Metselaar, B. Kerkwijk, E.J. Mulder, H. Verweij and D.J. Schipper, Wear of ceramics due to thermal stress: a thermal severity parameter, Wear 249 (2001) 962-970.

[8] J. Bos, Frictional Heating of Tribological Contacts, Ph.D. Thesis, University of Twente, The Netherlands, 1995.

[9] H.L. Ewalds and R.J.H. Wanhill (1989), Fracture Mechanics, revised edition, Delftse Uitgeverij Maatschappij, The Netherlands, 1989.

[10] H. Hertz, Über die Berührung fester elastischer Körper. J. Reine Angew. Math. 92 (1882) 156–171.

[11] K.L. Johnson, Contact Mechanics, Cambridge University Press, Cambridge, UK, 1995.

[12] D.A. Hills, D. Nowell and A. Sackfield, Mechanics of elastic contacts, Butterworth-Heinemann, 1993.

[13] H. Moes, Lubrication and beyond, University of Twente, Enschede, The Netherlands, 2000.

[14] A. Sackfield and D.A. Hills, Some useful results in the tangentially loaded Hertzian contact problem, Journal of Strain Analysis, Vol. 18 (1983) 107-197.

[15] B. Vick, M.J. Furey and K. Iskandar, Theoretical surface temperatures generated from sliding contact of pure metallic elements, Tribology International, 33 (2000) 265-271.

[16] A. Yuftushenko and S. Koniechny, Similarity solutions of stationary thermoelasticity with frictional heating, International Journal of Heat and Mass Transfer 42 (1999) 3539-3544.

[17] Z. Neder, K. Varady and L. Man, Numerical and finite element contact temperature analysis of steel-bronze real surfaces in dry sliding contact, ASME/STLE Tribology Conference, 1998.

[18] A.A. Yuvtushenko, E.G. Ivanyk and O.M. Ukhanska, Transient temperature of local moving areas of sliding contact, Tribology International 30 (1997) 209-214.

[19] Z.B. Hou and R. Komanduri, General solutions for stationary/moving plane heat source problems in manufacturing and tribology, International Journal of Heat and Mass Transfer 43 (2000) 1679-1698.
[20] K.M. Reuver, Friction and wear of ceramics (doped with CuO) sliding against ceramics and steel, M.Sc. Thesis, University of Twente, The Netherlands, 2004.
[21] H.S.C. Metselaar, Thermally induced wear of ceramics, Ph.D. Thesis, University of Twente, The Netherlands, 2001.

Chapter 3
Friction Reduction by Adding Copper Oxide into Alumina and Zirconia Ceramics

3.1 Introduction

Chapter 2 has clearly shown that the coefficient of friction influences the wear type of dry sliding ceramic couples. This means that a reduction of friction is necessary to extend the operational conditions of dry sliding ceramic couples in which no severe wear take place. In this chapter, attempts to reduce the coefficient of friction of dry sliding ceramics couples will be reviewed. Further, investigation results focused on the influence of CuO doped in alumina and zirconia ceramics in reducing the coefficient of friction will be reported and discussed.

3.2 Attempts to reduce friction of dry sliding ceramic couples

The friction of a system is determined by the real contact area and the interfacial shear strength of the contact between the two opposing bodies. Liquid lubrication is the most widely used method to reduce the interfacial shear strength and as a result reduction of friction and wear. The liquid lubricant forms a film between the surfaces providing low interfacial shear strength resulting in a low friction system. However, in some applications like biomedical applications, a synthetic lubricant is not permitted for medical reasons. In addition, at temperatures higher than 300°C, most liquid lubricants and greases are not chemically stable [1].

For dry sliding applications, high temperature applications in particular, friction is usually reduced using a solid lubricant either by covering the surfaces with a soft thin layer or by a self-lubricating composite in which second phase particles are dispersed within the base material. Due to sliding, however, a soft thin layer will experience wear and this will consequently limit the lifetime of the layer. Once the soft thin layer is completely removed, the coefficient of friction rises to the level of friction of the substrate material. In addition, the thickness of the coating must also be optimized in order to obtain an optimum low friction system.

To have a long-life low friction dry sliding system, a self-lubricating composite is preferred. Alexeyev and Jahanmir [2] investigated the friction behaviour of self-lubricating composites of 20% weight tin (Sn) dispersed in aluminium. Their investigation results revealed that due to the high contact pressure, the second phase soft metal particles were squeezed out of the matrix and plastically smeared by harder asperities of the counter surface, which then form a soft interfacial layer resulting in a low friction system.

An interesting dry sliding system should have a constant low friction, $f \approx 0.2$, and specific wear rate, k, less than $10^{-6} mm^3 N^{-1} m^{-1}$ [3]. Some articles [4-11] reported that depending on the normal load and the sliding velocity, the coefficients of friction of dry sliding alumina and zirconia ceramics range between 0.5 and 0.9 which is unacceptably high for practical applications. Therefore, low friction dry sliding ceramic systems are needed not only to extend the operating conditions but also to reduce energy losses due to friction.

Microstructure modification like grain size reduction shows a significant improvement of the wear resistant properties of ceramics [4, 5, 9]. However, reducing the grain size does not show any significant contribution in reducing the level of friction of dry sliding ceramic systems.

Wang et al. [12] investigated the friction behaviour of zirconia ceramic covered with a copper oxide layer of 50 nm thickness. Dry sliding tests conducted on this material showed a coefficient of friction lower than 0.2. Unfortunately, they only performed the sliding tests for 3.6 meters.

The idea of adding soft second phase particles into oxide ceramics was implemented by Kerkwijk et al. [13] and Sekulic [14]. Kerkwijk et al. [13] doped 5 % wt of soft metal oxides (CuO, MgO, MnO_2, ZnO and B_2O_3) into alumina and zirconia. Dry sliding tests were carried out on these composite materials and the experimental results showed that only CuO between these soft metal oxides could contribute significantly in lowering the coefficient of friction. Kerkwijk et al [13] reported that the addition of CuO into oxide ceramics reduced the coefficient of friction from 0.65 to 0.45. Seculic [14] added many other additives into alumina and zirconia. She added 5% weight of CuO, TiO_2, B_2O_3, V_2O_5, MoO_3, In_2O_3, SnO_2 and Cr_2O_3 into the alumina and zirconia ceramics. Her investigation results confirmed the results reported by Kerkwijk et al. [13] that CuO doped in alumina and zirconia can significantly reduce the coefficient of friction of dry sliding alumina and zirconia ceramic systems. However, the friction mechanism responsible for reducing friction in the tribosystem of dry sliding oxide ceramics doped with CuO is not yet clear.

Further investigation results on friction and wear of alumina and zirconia doped with CuO in various environmental conditions are presented in this chapter. Also, the mechanism of low friction will be discussed.

3.3 Material preparation

Various weight percentages (0.5 % wt, 1 % wt and 5 % wt) of commercially available copper oxide powder (Alfa Chemicals, Germany) were added to α-alumina powder (AKP50, Sumitomo, Japan). The composite of CuO and α-alumina was sintered at 1500°C for four hours.

Also, various weight percentages (1 % wt and 5 % wt) of the copper oxide powder were added to 3Y-TZP powder (Tosoh, Japan) [15]. The composite of CuO and 3Y-TZP was sintered at various sintering temperatures resulting in various specimens with different densities (see table 3.1).

Table 3.1: List of specimens made of zirconia doped with CuO sintered at various temperatures [15].

Specimen	Composition 3Y-TZP + x wt % CuO	Sintering temp. (°C) Sintering time (hours)	Density
1	5%	1350, 4	68%
2	1%	1400, 4	Not measured
3	5%	1400, 4	70%
4	5%	1450, 4	78%
5	5%	1500, 4	92%
6	5%	1550, 8	95%

The material ready for investigation was cut into discs of 36 mm diameter and 4 mm thickness. The discs were polished to a centreline surface roughness (Ra) of 0.1 μm.

3.4 Testing procedure

The dry sliding tests were performed by using a pin-on-disc tribometer (CSEM, Switzerland, see chapter 2 section 2.4). In order to obtain given test conditions the tribometer was placed in a climate chamber by which the temperature (up to 80°C) and the relative humidity (18 % - 95 %) could be set. The tests at elevated temperature (up to 800°C) were performed using a high temperature pin-on-disc tribometer (CSEM, Switzerland). Sliding tests on the materials were conducted with various normal loads (1 - 10 N) and various velocities (0.1-0.5 m/s). All the tests were performed for at least 1 km sliding distance. Commercially available 10 mm diameter Al_2O_3, ZrO_2, SiC and Si_3N_4 ceramics balls were used as a stationary counter-body. The discs and the balls were cleaned ultrasonically in ethanol for 30 minutes and dried at 120°C prior to use.

3.5 Friction and wear of alumina and zirconia doped with CuO at room temperature

3.5.1 Alumina doped with CuO

Overall results of the sliding tests conducted on alumina doped with CuO against alumina are summarized in table 3.2. Figure 3.1 clearly shows that the addition of 5% wt CuO into alumina (when sliding against an alumina ball) can reduce the coefficient of friction from 0.65 to 0.45. At the first 100 m sliding distance, the coefficient of friction of various percentages of CuO in alumina sliding against alumina balls started at a value of approximately 0.25 and slowly increased up to 0.4 after 100 meters as shown in figure 3.2. The low coefficient of friction for the first 100 meters was probably due to the presence of hydroxide on the specimens [16]. After 1000 meters sliding distance, the variation of the percentage of CuO in alumina does not show much influence in reducing the coefficient of friction (see table 3.2), the coefficient of friction stayed at the same level of about 0.45. The experimental results also show that the variation in normal load and sliding velocity does not much influence the value of the coefficient of friction ($f \approx 0.45$).

Alumina doped with CuO sliding against zirconia, silicon carbide and silicon nitride ceramic balls does show a significant contribution in reducing the coefficient of friction (see table 3.3). The coefficients of friction in these tests have a value of about 0.55 or higher.

Tabel 3.2: Coefficient of friction (steady state, i.e. after 1000 m sliding distance) of various percentage of CuO doped in alumina sliding against alumina ceramic balls at various normal loads and sliding velocities.

Normal Load [N]; (P_{max} [GPa])	**Sliding Velocity [m/s]**	**Coefficient of Friction**			
		Al_2O_3 + 0 % wt CuO	**Al_2O_3 + 0.5 % wt CuO**	**Al_2O_3 + 1 % wt CuO**	**Al_2O_3 + 5% wt CuO**
5 ; (1.17)	0.1	-	0.45	0.40	0.47
	0.2	-	0.43	0.39	0.43
	0.4	-	0.45	0.44	0.43
10 ; (1.48)	0.1	0.7	0.45	0.47	0.43

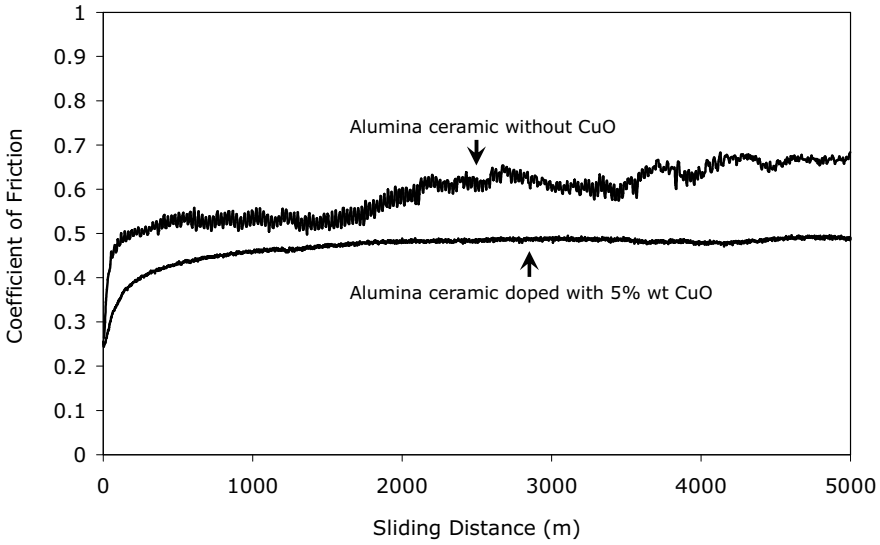

Figure 3.1: Coefficient of friction as a function of sliding distance of alumina disc without copper oxide and alumina disc doped with 5 % weight of CuO sliding against an alumina ball at 10 N normal load and 0.1 m/s sliding velocity.

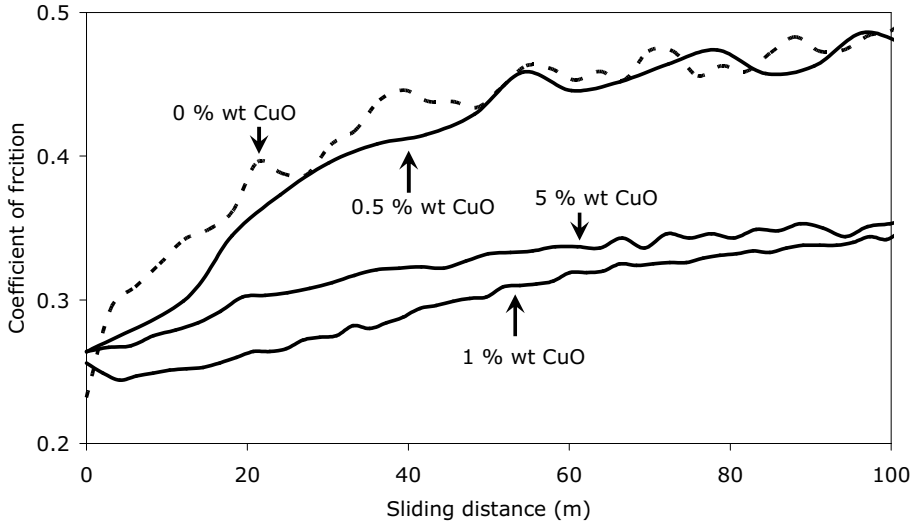

Figure 3.2: Coefficient of friction as a function of sliding distance of alumina disc without copper oxide and alumina disc doped with 0.5 %, 1 % and 5 % wt of CuO sliding against alumina balls respectively, at 10 N normal load and 0.1 m/s sliding velocity (the first 100 m).

Table 3.3: Coefficient of friction of 1 % wt CuO in alumina sliding against various ceramic balls at various normal loads and sliding velocities.

Balls	Normal Load [N]; (P_{max} [GPa])	Velocity [m/s]	Coefficient of Friction	
			Al_2O_3 + 0 % wt CuO	Al_2O_3 + 1 % wt CuO
Al_2O_3	5 ; (1.17)	0.1	0.70	0.40
		0.15	-	0.38
		0.2	-	0.39
		0.4	-	0.44
		0.5	-	0.45
	10 ; (1.48)	0.1	0.65	0.47
		0.2	-	0.45
		0.3	-	0.50
		0.4	-	0.52
		0.5	-	0.71
ZrO_2	5 ; (0.93)	0.1	0.85	0.52
		0.2	0.80	0.59
	10 ; (1.17)	0.1	-	0.62
SiC	5 ; (1.2)	0.2	0.78	0.65
		0.3	-	0.70
Si_3N_4	5 ; (1.1)	0.2	-	0.60
		0.3	-	0.80
		0.5	-	0.90

In general, the wear of alumina doped with CuO sliding against alumina is mild ($k < 10^{-7}$ $mm^3N^{-1}m^{-1}$). Only at high contact pressures and high sliding velocities, i.e. table 3.3 for normal load 10N and sliding velocity 0.5 m/s, high friction and severe wear occurs.

3.5.2 Zirconia doped with CuO

Figure 3.3 shows the coefficient of friction of zirconia doped with 5 % wt CuO sintered at various temperatures sliding against alumina. The steady state coefficients of friction for the first 1 km sliding distance of all the specimens with 5 % wt CuO (see figure 3.3) show that the specimens sintered at 1500°C give the lowest coefficient of friction. However, at a sliding distance more than 1 km, the coefficient of friction of the specimen sintered at 1500°C suddenly increased to a value of 0.7 accompanied by a sudden transition in wear. This phenomenon was also observed in the sliding tests of zirconia doped with 1 % wt CuO sintered at 1400°C (see figure 3.4). This transition phenomenon will be discussed further in section 3.9. For these cases, there was no significant wear observed when the coefficients of friction were lower than 0.25 (mild wear) but a lot of wear was observed (severe wear) after the transition in the coefficient of friction.

The tests of all the specimens listed in table 3.1 sliding against ZrO_2, SiC and Si_3N_4 ceramic balls did not show a low value of the coefficient of friction (f ≈ 0.6 to 0.8).

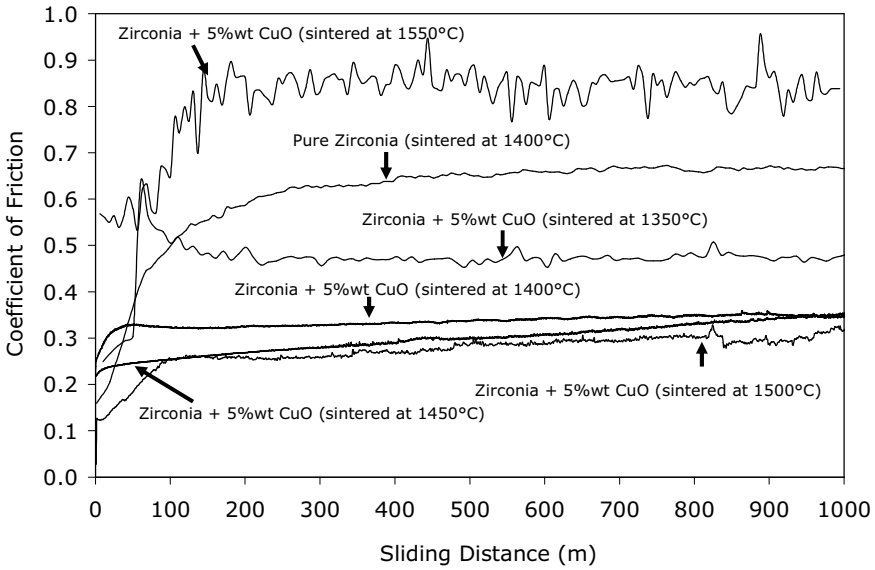

Figure 3.3: Coefficient of friction as a function of sliding distance of specimens listed in table 3.1 sliding against alumina (normal load 5N and sliding velocity 0.1 m/s).

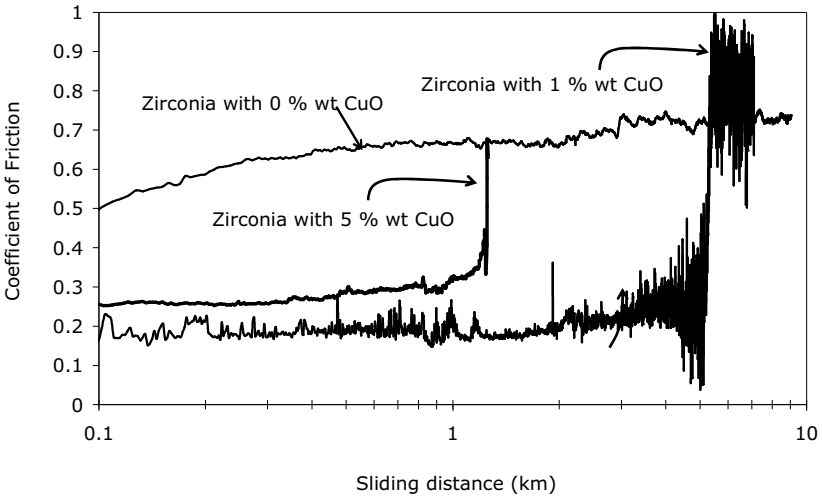

Figure 3.4: Coefficient of friction as a function of sliding distance of zirconia doped with 1 % wt CuO and zirconia doped with 5 % wt CuO sintered at 1500°C sliding against alumina (normal load 5N and sliding velocity 0.1 m/s).

The coefficient of friction varies as the normal load changes. The variation of the coefficient of friction for various loads can be seen clearly in table 3.4. In general, for low loads the coefficient of friction tends to be low and as the load increases the coefficient of friction increases and as a result, the wear changes from mild to severe wear.

Table 3.4: Coefficient of friction of various 1 % wt CuO and 5 % wt CuO in zirconia sliding against alumina at various normal loads and 0.1 m/s sliding velocity.

	Coefficient of Friction		
Normal Load [N]; (P_{max} [GPa])	**ZrO_2 + 0 % wt CuO**	**ZrO_2 + 1 % wt CuO**	**ZrO_2 + 5 % wt CuO**
1 ; (0.55)	-	0.29	0.35
2 ; (0.69)	-	0.28	0.35
3 ; (0.79)	0.68	-	-
5 ; (0.94)	0.7	0.2 (up to 4 km) & 0.8 (after 4.2 km)	0.25
7 ; (1.05)	-	-	0.27
8 ; (1.1)	0.75	-	0.35
9 ; (1.15)	-	-	0.42
10 ; (1.19)	-	0.6	0.43

3.6 Friction and wear of alumina and zirconia doped with CuO at various humidities

Alumina doped with 5 % wt CuO was also tested against alumina in high humidity environments. At high humidity, the coefficient of friction of dry sliding alumina doped with 5 % wt CuO sliding against alumina is reduced but not significantly (see figure 3.5). This phenomenon was also observed by Gee [16] for pure alumina tested at various humidities. According to Gee [16], low friction occurs due to the presence of hydroxide that forms during sliding.

There was hardly any wear observed for all the tests performed at high humidity of alumina doped with 5 % wt CuO sliding against alumina ($k << 10^{-7}$ $mm^3N^{-1}m^{-1}$).

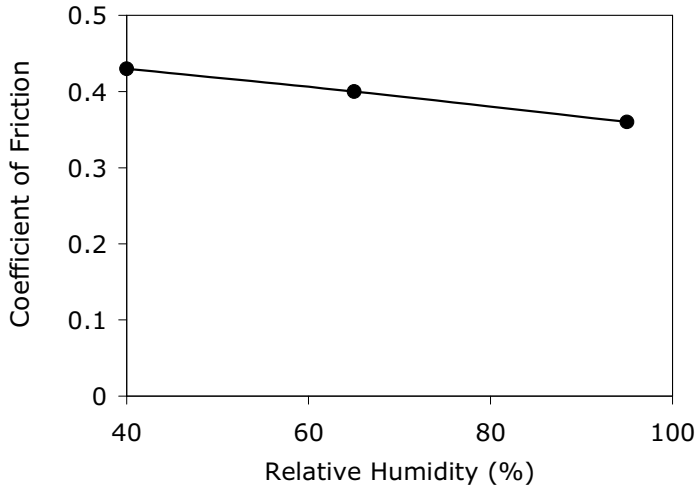

Figure 3.5: Coefficient of friction of alumina doped with 5 % wt CuO sliding against alumina as a function of the relative humidity (normal load 5N and sliding velocity 0.1 m/s).

In contrast with zirconia doped with CuO, the effect of humidity on friction is really significant (see figure 3.6a and 3.6b). In general, the coefficient of friction of zirconia doped with CuO decreases as the relative humidity increases, but humidity does not show a significant effect on friction and wear of pure zirconia (see figure 3.6c). The coefficients of friction as a function of sliding distance in general follow a certain characteristic. At the start, the coefficient of friction is low for a certain sliding distance then gradually increases and stays at a high value. The low coefficient of friction at high humidity may be caused by the formation of a soft tribochemistry layer during sliding, [17].

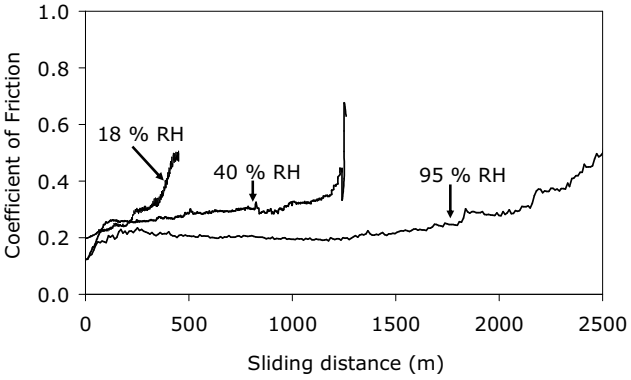

(a)

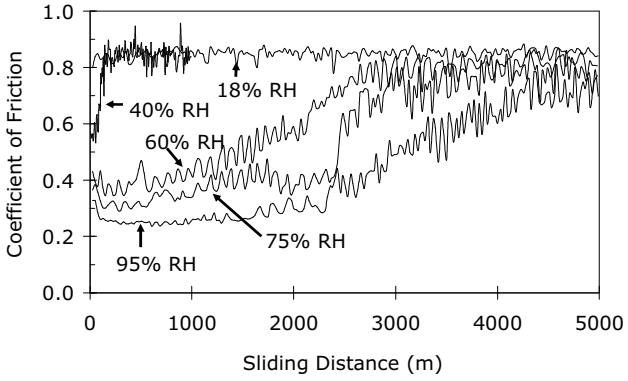

(b)

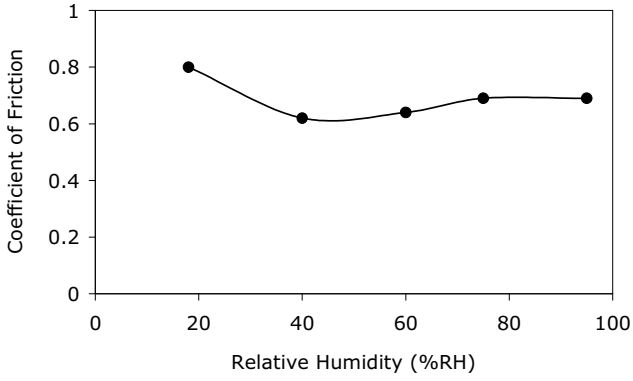

(c)

Figure 3.6: Coefficient of friction of zirconia doped with CuO sintered at 1550°C (a), zirconia doped with CuO sintered at 1500°C (b) and pure zirconia (c) at various humidities (normal load 5N and sliding velocity 0.1 m/s).

3.7 Friction and wear of alumina and zirconia doped with CuO at elevated temperatures

At elevated temperatures (up to 500°C), alumina doped with 5 % wt CuO sliding against alumina shows an increase in friction. The coefficient of friction increases from 0.4 to 0.8 as the temperature increases (see figure 3.7). The values of the coefficient of friction are in the same range with the values observed by Dong et al. [18] where the coefficient of friction of pure alumina increased from 0.4 to 0.8 as the temperature increased from 100°C to 800°C.

Specific wear rates, $k < 10^{-7}$ $mm^3N^{-1}m^{-1}$, were observed in the sliding tests of alumina doped with CuO sliding against alumina at elevated temperatures.

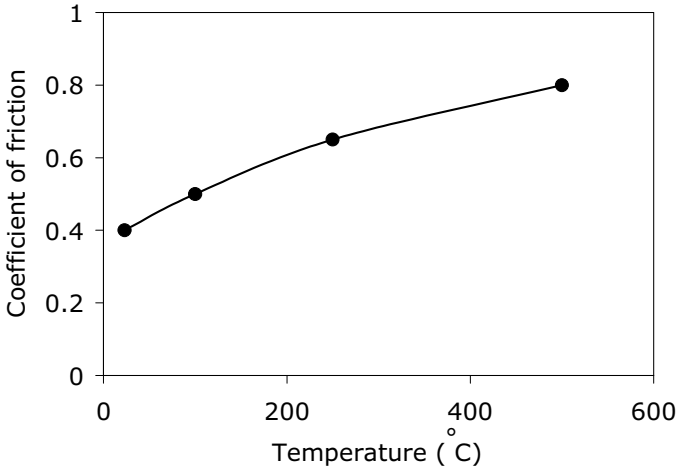

Figure 3.7: Coefficient of friction of alumina doped with 5 % wt CuO sliding against alumina at elevated temperatures.

The steady state coefficients of friction of zirconia doped with CuO sliding against alumina tested at elevated temperatures are shown in figure 3.8. At elevated temperatures, the coefficients of friction of zirconia doped with CuO are at about the same value as that of pure zirconia. In addition a lot of wear (severe wear) was observed when zirconia doped with CuO was tested at elevated temperatures. For pure zirconia, Stachowiak [19] observed that the coefficient of friction increased from 0.55 to 0.7 when the temperature was increased from room temperature to 400°C. Stachowiak [19] also reported high wear of zirconia tested at elevated temperatures.

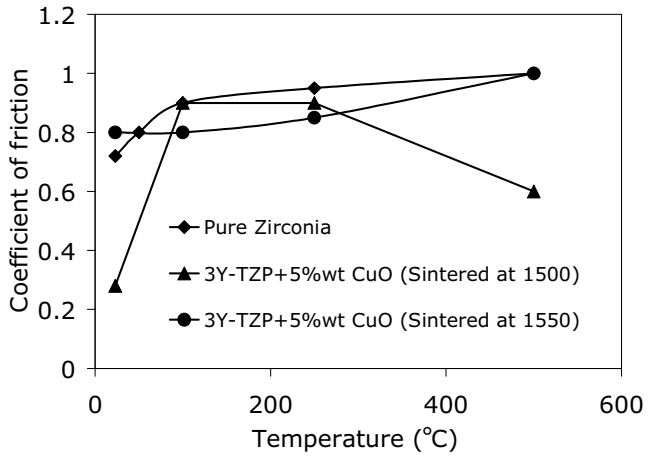

Figure 3.8: Steady state coefficient of friction of pure zirconia and zirconia doped with CuO sliding against alumina at elevated temperatures.

3.8 Friction and wear of alumina and zirconia doped with CuO sliding against steel

If alumina doped with 5 % wt CuO is tested against steel, the coefficient of friction ranges from 0.55 to 0.65 depending on the sliding velocity (see figure 3.9). It was observed that the steel wears a lot whereas alumina doped with 5 % wt CuO does not wear at all and some of the worn metal is transferred onto the ceramic surfaces which in fact create a metal-metal tribosystem [9].

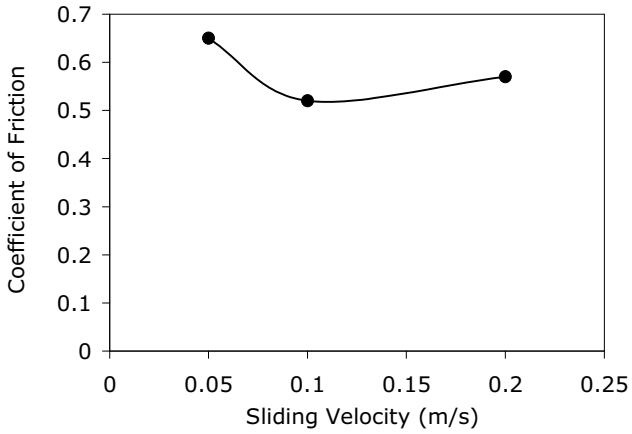

Figure 3.9: Coefficient of friction as a function of sliding velocity of alumina doped with 5 % wt CuO sliding against steel (normal load 1N).

Pure zirconia and zirconia doped with CuO were tested against ball bearing steel under dry sliding conditions and lubricated conditions using a transmission oil. The results show (see figure 3.10) that in dry and lubricated systems, the addition of CuO does not make any contribution to lowering the coefficient of friction but on the contrary, a somewhat higher friction is observed. The presence of CuO in zirconia increases the adhesion force with steel which causes a higher coefficient of friction. Observations on the discs after dry sliding revealed that a lot of metal was transferred onto the ceramic surface which also indicates the strong adhesion between the metal and the ceramic. Therefore, after a certain sliding distance a lot of metal transfer occurs, and the tribosystem is no longer a ceramic-metal system but a metal-metal system [9]. In the lubricated situation, the coefficient of friction of pure zirconia and zirconia doped with CuO shows a slight difference at higher velocities (0.1 and 0.2 m/s). This is due to the fact that the shear in the contact was partly taking place in the lubricant.

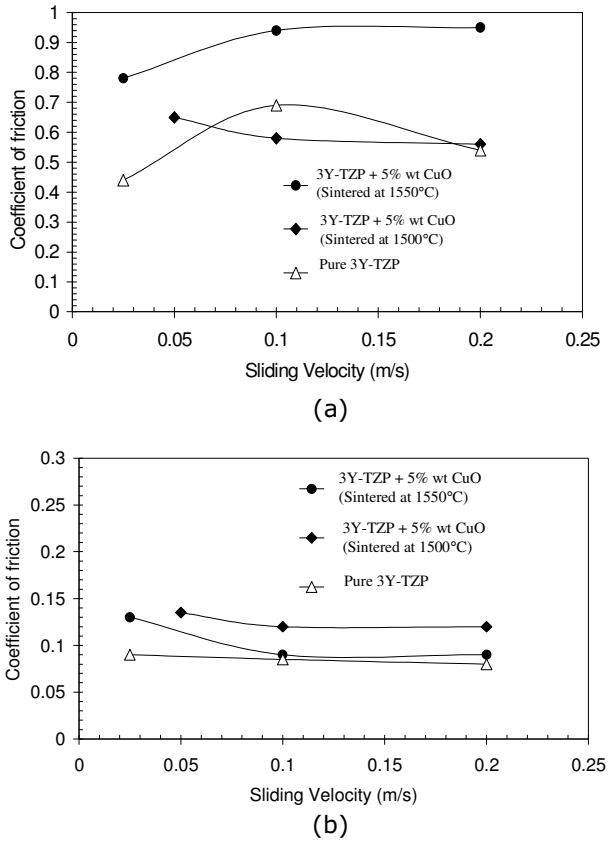

Figure 3.10: Coefficient of friction of zirconia doped with CuO sliding against alumina (a) dry and (b) lubricated.

3.9 Low friction mechanism

SEM pictures taken from the wear track of alumina doped with CuO sliding against alumina (see figure 3.11) show that after a short sliding distance, a small number of grains are in contact which carry the load. These grains are cut microscopically which creates debris as the system slides on. In time, the debris is trapped in the wear track, then compacted to form a smooth patchy layer. Further sliding causes the patchy contact area to increase and stabilize to a certain value, which also indicates the stable steady-state coefficient of friction.

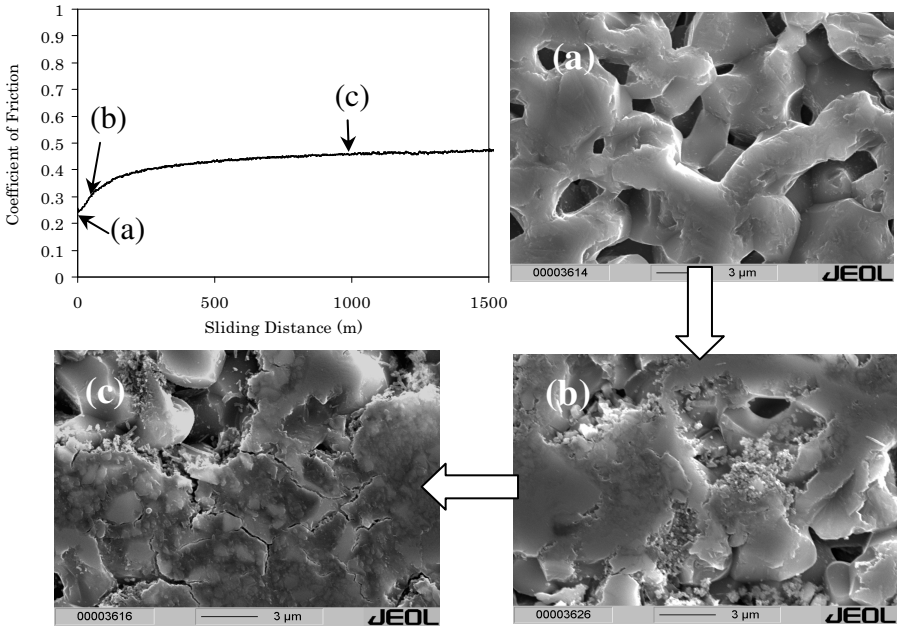

Figure 3.11: SEM pictures of (a) the bulk material before testing, (b) the wear track at a low coefficient of friction (f ≈ 0.25) and (c) the wear track at a higher value of the coefficient of friction (f ≈ 0.45) of alumina ceramic doped with 1 % wt CuO sliding against alumina at 5N normal load and 0.1 m/s sliding velocity.

The SEM pictures (figure 3.12) were taken in each specific region of the coefficient of friction versus the sliding distance graph: low friction region, transition region and high friction region. The SEM pictures show that an interfacial layer was formed. The layers are not uniform but patchy. Surface profile measurement across the wear track using the surface interferometer shows that a very smooth wear track is formed (see figure 3.13). The patchy layer is formed during sliding and a self-lubrication mechanism is generated. It appears that the surface deforms plastically and creates an interfacial layer in

the contact. This layer is removed gradually (the transition region) which causes the wear track to be rougher as well as an increase in the coefficient of friction.

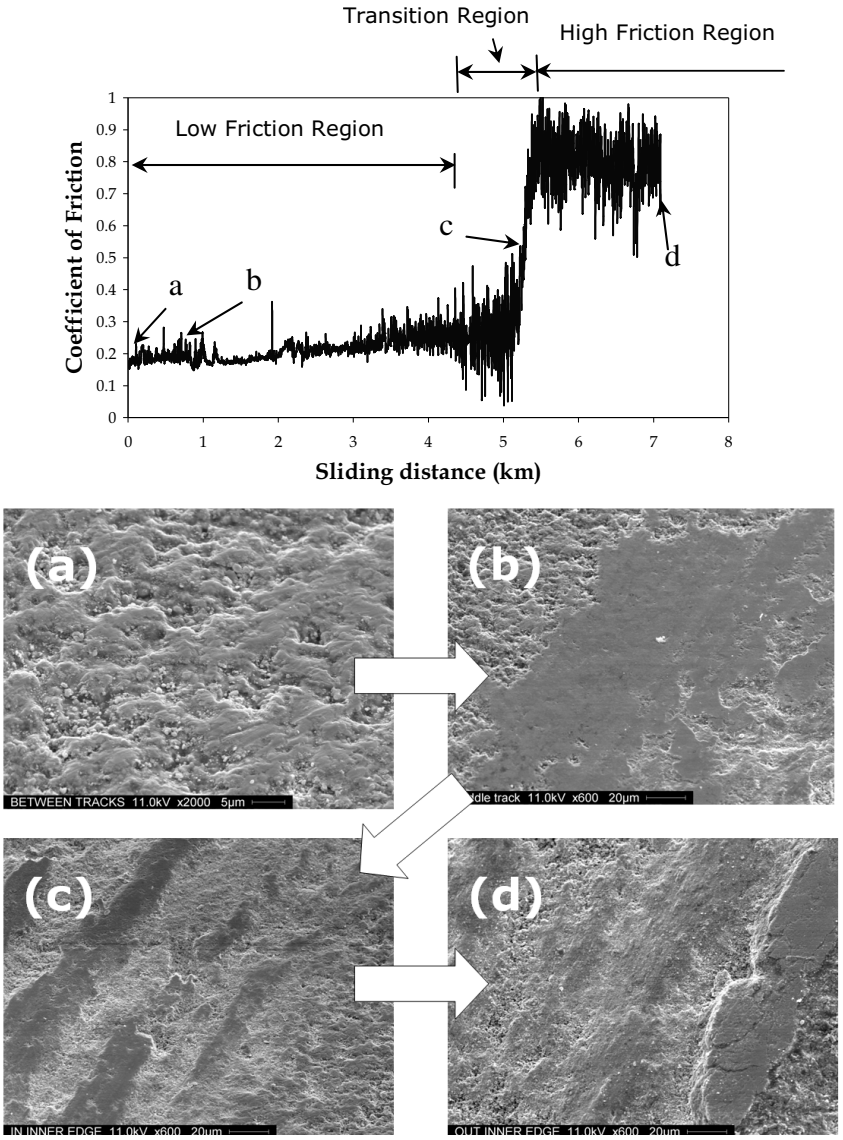

Figure 3.12: SEM pictures of the genesis of the wear track of a zirconia disc doped with 1 % wt CuO sliding against an alumina ball at 5 N normal load and 0.1m/s sliding velocity. (a) SEM picture of bulk material before the test (b) after 500 m of sliding ($f \approx 0.2$) (c) after slide for 4 km of sliding ($f \approx 0.45$) and (d) after 7 km of sliding ($f \approx 0.8$).

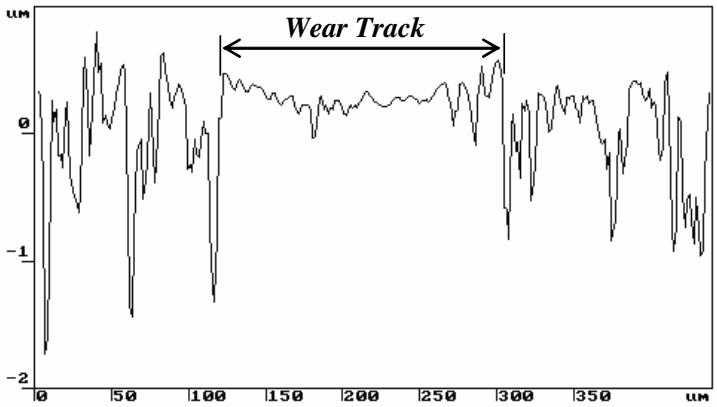

(a)

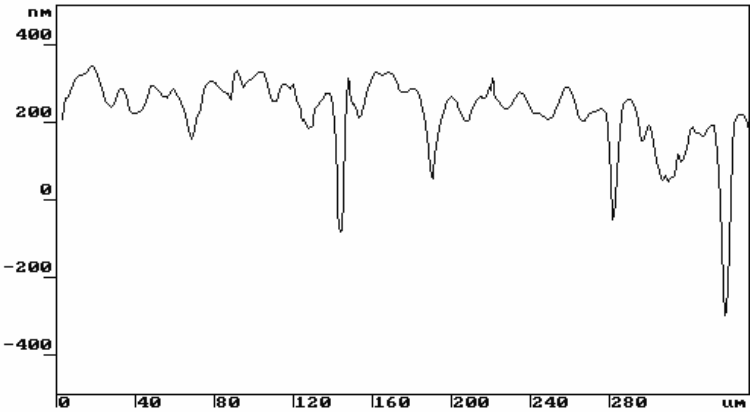

(b)

Figure 3.13: Wear track profiles of zirconia doped with 1 % wt CuO sliding against an alumina ball. (a) Across the wear track (b) along the wear track.

Nano-hardness measurements (see appendix B) were conducted on alumina and zirconia doped with CuO, both in the wear track (at the patchy layer) as well as outside the wear track (bulk material). The hardness measurement results as a function of the penetration depth are presented in figure 3.14.

For the zirconia doped with CuO, the hardness of the surface inside the track (patchy layer) and outside the track for low indentation depths have almost the same value. This might indicate that a soft layer is formed when polishing the disc. This layer may also be the reason that the coefficient of

friction at the start of each experiment is rather low. The measurement results also show that the hardness of the patchy layer (H ≅ 6 GPa) is much less than the hardness of the bulk (H ≅ 14 GPa). This soft interfacial layer behaves as a solid lubricant layer that reduces the resistance to motion and as a result lowering the coefficient of friction.

In contrast with zirconia doped with CuO, the hardness measurement results of alumina doped with CuO showed that the patchy layer is harder than the hardness of the bulk material itself. It might be that during the formation of the patchy layer it continuously compacted resulting in a hard layer.

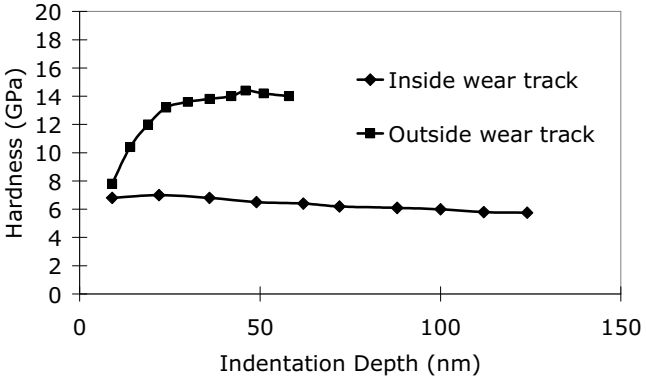

(a)

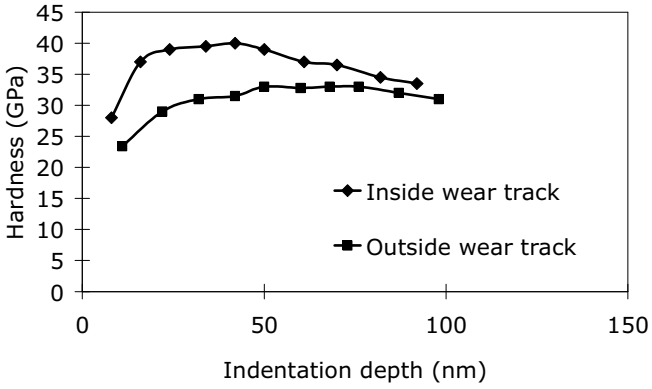

(b)

Figure 3.14: Hardness as a function of penetration depth of (a) zirconia doped with CuO and (b) alumina doped with CuO sliding against alumina.

The XRD analysis of zirconia doped with CuO (sintered at 1500°C) shows that a strong peak of copper is observed in the wear track where low friction was observed (see figure 3.15) but is not really pronounced in the bulk material. These results confirm that the presence of a copper rich layer, which is soft, is present in the wear track of zirconia doped with CuO.

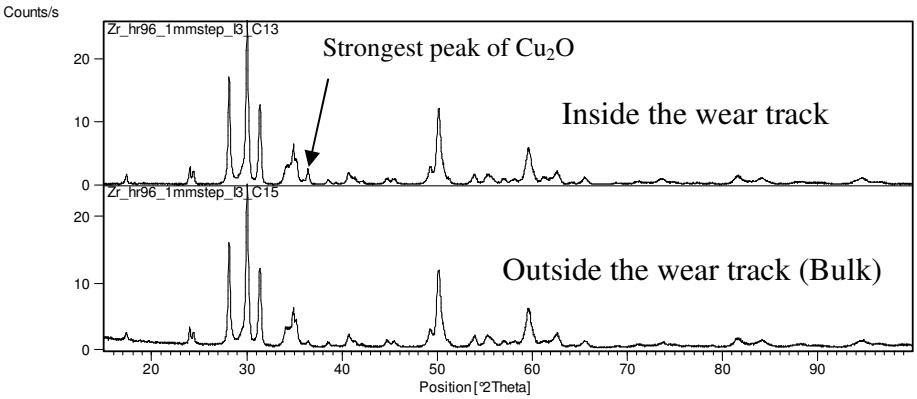

Figure 3.15: XRD pattern of the wear track where low friction was observed and the bulk of zirconia doped with 5 % wt CuO sintered at 1500°C sliding against alumina.

3.10 Concluding remarks

This chapter has shown the influence of CuO in reducing the friction of alumina and zirconia for the dry sliding contact situation. The effects of load, velocity, humidity and temperature on friction are shown. Low coefficients of friction, between 0.15 to 0.25 for a sliding distance of 1 km and more, were observed in the tribosystem of zirconia doped with CuO sliding against alumina. The SEM pictures and hardness measurements suggest that a smooth patchy layer is present in the wear track and for the case of zirconia doped with CuO, the patchy layer is softer which indicates a self-lubricating mechanism. In chapter 4, a contact model of a rough surface in contact with a flat layered surface will be presented followed by friction model in chapter 5.

References

[1] H.E. Sliney, Solid lubricant materials for high temperatures – a review, Tribology International 15 (1982) 303-314.

[2] N. Alexeyev and S. Jahanmir, Mechanics of friction in self-lubricating composite materials, I: Mechanics of second phase deformation and motion, Wear, 166 (1993) 41-48.

[3] H. Czhichos, D. Klaffke, E. Santner and M. Woydt, Advances in tribology: The material point of view, Wear, 190 (1995) 53-56.

[4] K.-H. Zum Gahr, Modeling and microstructural modification of alumina ceramic for improved tribological properties, Wear, 200 (1996) 215-224.

[5] K.-H. Zum Gahr, Effect of grain size on friction and sliding wear of oxide ceramics, Wear, 162-164 (1993) 269-279.

[6] K.-H. Zum Gahr, Ch. Bogdanow and J. Schneider, Friction and wear reduction of Al_2O_3 ceramics by laser-induced surface alloying, Wear 181-183 (1995) 118-128.

[7] M. Woydt, J. Kadoori, K.-H. Habig and H. Hausner, Unlubricated sliding behaviour of various zirconia-based ceramics, Journal of the European Ceramic Society, 7 (1991) 135-145.

[8] G.W. Stachowiak and G.B. Stachowiak, Environmental effects on wear and friction of toughened zirconia ceramics, Wear, 160 (1993) 153-162.

[9] Y. He, Tribological and mechanical properties of fine-grained zirconia and zirconia-alumina ceramics, PhD Thesis, University of Twente, The Netherlands, 1995.

[10] B. Kerkwijk, Wear and friction of nanostructured zirconia and alumina ceramics and composites, PhD Thesis, University of Twente, The Netherlands, 1999.

[11] H.S.C. Metselaar, Thermally induced wear transition in ceramics, PhD Thesis, University of Twente, The Netherlands, 2001.

[12] Y. Wang, F.J. Worzala and A.R. Lefkow, Friction and wear properties of partially stabilized zirconia with solid lubricant, Wear, 167 (1993) 23-31.

[13] B. Kerkwijk, M. García, W.E. van Zyl, A.J.A. Winnubst, E.J. Mulder, D.J. Schipper and H. Verweij, Friction behaviour of solid oxide lubricants as second phase in -Al2O3 and stabilised ZrO2 composites, Wear 256, (2004) 182-189.

[14] J. Sekulic, Wear resistant ceramics with low friction, Final Report 00372/CT31/js, Inorganic Materials Science Group, University of Twente, 2000.

[15] S. Ran, CuO doped 3Y-TZP ceramics with low friction, First half year report, Inorganic Materials Science Group, University of Twente, The Netherlands, 2003.

[16] M.G. Gee, Wear testing and ceramics, Proceeding of the Institution of Mechanical Engineers 208 (1994) 153-166.

[17] S. Sasaki, Effects of environment on friction and wear of ceramics, Bulletin of Mechanical Engineering Laboratory, No. 58, Japan, 1992.

[18] X. Dong, S. Jahanmir and S.M. Hsu, Tribological characteristics of α-alumina at elevated temperatures, Journal of American Ceramic Society 74 (1991) 1036-1044.
[19] G.W. Stachowiak and G.B. Stachowiak, Unlubricated wear and friction of toughened zirconia ceramics at elevated temperatures, Wear 143 (1991) 277-295.

Chapter 4
Deterministic Contact Model of a Rough Surface in Contact with a Flat Layered Surface

4.1 Introduction

Chapter 3 has shown that a tribosystem of zirconia doped with CuO sliding against alumina exhibits a low coefficient of friction ($f \approx 0.15$-0.25). The nano-indentation results (see figure 3.14a) and the SEM pictures (see figure 3.12) reveal that a soft thin layer is present in the wear track. This soft thin layer provides easy shear that principally reduces friction. So, in fact, the tribosystem of zirconia doped with CuO sliding against alumina is a soft layer on top of a hard substrate in contact with a hard counter-surface. To model this tribosystem, in this chapter, a general contact model of a rough surface in contact with a flat layered surface will be outlined. This contact model will be developed further in chapter 5 to predict the friction of a rough surface sliding against a flat layered surface. Further, in chapter 6, the prediction of the coefficient of friction of zirconia doped with CuO sliding against alumina will be presented and discussed.

4.2 Overview of contact models

4.2.1 Statistical contact model of Gaussian surfaces

The work of Greenwood and Williamson [1] was among the first to provide a significant contribution to the research of contact between rough surfaces. They developed a statistical model to analyze the contact behaviour of rough surfaces by modelling a rough surface as an array of spherically capped asperities with the same radius, and the asperities' heights varied randomly following a Gaussian distribution. Their work has been cited in many articles and has experimentally been proven [2] for the case of elastic contact. However, the experimental results show a significant deviation from the theoretical calculation when the contact situation is no longer elastic, i.e. elastic plastic or fully plastic.

The work of Greenwood and Williamson [1] in studying the contact of two nominally flat surfaces for an elastic contact situation has been extended by Zhao et al. [3] by incorporating the contribution of the elastic-plastic and fully plastic contact situations. Zhao et al. [3] followed the assumption of Greenwood

and Williamson [1] by assuming a rough surface to be an array of spherically capped asperities with the same radius (β) the heights of which vary randomly following a Gaussian distribution (statistical model). They also assumed that there is no interaction between the neighbouring asperities and the deformation is solely at the asperity level. Based on this assumptions, if a rough surface is in contact with a perfectly smooth surface and these two surfaces are separated by a distance d, then the number of asperities in contact (n), the real contact area (A_e) and the load carried by the asperities in contact (P_e) in an elastic contact situation can be calculated respectively as follows [3]:

$$n = \eta A_{nom} \int_{h}^{\infty} \phi^*(s)ds \tag{4.1}$$

$$A_e = \pi\eta A_{nom}\beta\sigma \int_{h}^{h+\omega_{c1}^*} (s-h)\phi^*(s)ds \tag{4.2}$$

$$P_e = \frac{4}{3}\eta A_{nom} E^* \beta^{0.5}\sigma^{1.5} \int_{h}^{h+\omega_{c1}^*} (s-h)^{1.5}\phi^*(s)ds \tag{4.3}$$

with:

$$E^* = \frac{E_1\ E_2}{E_1(1-v_2^2) + E_2(1-v_1^2)} \tag{4.4}$$

$$\phi^*(s) = \frac{1}{\sqrt{2\pi}} \exp\left(-\frac{1}{2}s^2\right) \tag{4.5}$$

where η is the asperity density, A_{nom} is the nominal contact area, σ is the standard deviation of the asperity height, h is the standardized separation (d/σ), E is the elasticity modulus, v is the Poisson ratio, ω^*_{c1} is the standardized onset of yielding (see equation 4.7) and subscripts 1 and 2 denote the two bodies in contact.

The contact situation can change from elastic to elastic-plastic if the load is sufficient to initiate the onset of yielding. Tabor [4] observed that for metals, the onset of yielding occurs when the maximum Hertzian contact pressure reach 0.6 times the hardness of the material deformed. Based on the work of Tabor [4], Greenwood and Williamson [1] defined the critical indentation depth (ω_{c1}) at which the onset of yielding occurs as:

$$\omega_{c1} = 0.89\beta\left(\frac{H}{E^*}\right)^2 \tag{4.6}$$

where H is the hardness of the softer material in contact.
In standardized form, equation 4.6 can be written as:

$$\omega_{c1}^{*} = \frac{\omega_{c1}}{\sigma} = 0.89 \frac{\beta}{\sigma} \left(\frac{H}{E^{*}} \right)^{2} \tag{4.7}$$

Further deformation after the onset of yielding will lead to an elastic-plastic contact situation. The range of the elastic-plastic contact area is significant and the critical indentation depth (ω_{c2}) at which the transition from the elastic-plastic to fully plastic contact situation occurs is a few times more than the onset of yielding:

$$\omega_{c2} = c\ \omega_{c1} \quad ; \quad \omega_{c2}^{*} = c\ \omega_{c1}^{*} \tag{4.8}$$

Based on the work of Johnson [5], Zhao et al. [3] suggested that the fully plastic contact situation will occur when an asperity is deformed more than 54 times the onset of the first yielding (c = 54). According to Jackson and Green [6], based on the finite element simulations they performed, the value of the constant c in equation (4.8) can be about 110. A different value of constant c will certainly lead into a significant difference in calculating the contact area and the total load carried by the asperities. However, Jackson and Green [6] reported in their paper that they observed an error of up to 17% between the Hertzian contact area obtained from their finite element simulations and the analytical solution. Depending on the penetration depth, the contact area calculated by using the model of Jackson and Green [6] shows about 0 to 20 % difference from the contact area calculated using the model of Zhao et al. [3]. This error is in the range of difference between the contact area calculated with the model of Zhao et al. [3] and the contact area calculated with the model of Jackson and Green [6]. Therefore in this thesis the calculation of the contact area is carried out based on the work of Zhao et al. [3].

Zhao et al. [3] defined a smooth transition from the elastic to the fully plastic contact situation based on a third order polynomial template (see figure 4.1). According to Zhao et al. [3], the real contact area (A_{ep}) and the load carried by asperities at the elastic-plastic contact situation (P_{ep}) can be calculated as:

$$A_{ep} = \pi \eta A_{nom} \beta \sigma \times \int_{h+\omega_{c1}^{*}}^{h+\omega_{c2}^{*}} (s-h) \left[1 - 2 \left(\frac{(s-h)-\omega_{c1}^{*}}{\omega_{c2}^{*}-\omega_{c1}^{*}} \right)^{3} + 3 \left(\frac{(s-h)-\omega_{c1}^{*}}{\omega_{c2}^{*}-\omega_{c1}^{*}} \right)^{2} \right] \phi^{*}(s) ds \tag{4.9}$$

$$P_{ep} = \pi\eta A_{nom} H\beta\sigma \int_{h+\omega_{c1}^*}^{h+\omega_{c2}^*} \left[1 - 0.6\frac{\ln\omega_{c2}^* - \ln(s-h)}{\ln\omega_{c2}^* - \ln\omega_{c1}^*}\right] \times$$
$$(s-h)\left[1 - 2\left(\frac{(s-h)-\omega_{c1}^*}{\omega_{c2}^* - \omega_{c1}^*}\right)^3 + 3\left(\frac{(s-h)-\omega_{c1}^*}{\omega_{c2}^* - \omega_{c1}^*}\right)^2\right]\phi^*(s)ds \quad (4.10)$$

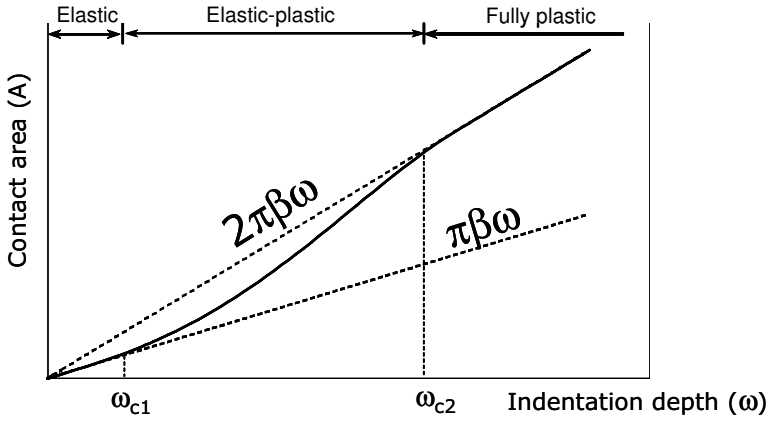

Figure 4.1: Contact area as a function of the indentation depth as proposed by Zhao et al. [2].

At fully plastic contact, the contact area (A_p) and the load carried by asperities (P_p) can be calculated as [2]:

$$A_p = 2\pi\eta A_{nom}\beta\sigma \int_{\omega_{c2}^*}^{\infty} (s-h)\phi^*(s)ds \quad (4.11)$$

$$P_p = 2\pi\eta A_{nom}\beta\sigma H \int_{\omega_{c2}^*}^{\infty} (s-h)\phi^*(s)ds \quad (4.12)$$

So, the total real contact area (A_{tot}) and the total load carried by asperities (P_{tot}) can be calculated by summarizing respectively the contact area and the load carried at elastic, elastic-plastic and fully plastic contact situation:

$$A_{tot} = A_e + A_{ep} + A_p \quad (4.13)$$

$$P_{tot} = P_e + P_{ep} + P_p \quad (4.14)$$

4.2.2 Statistical contact model of non-Gaussian surfaces

In practice, many engineering surfaces do not have a Gaussian height distribution. Kotwal and Bushan [7] attempted to solve the problem of the contact between non-Gaussian surfaces. Instead of using the Gaussian probability density function (equation (4.5)) they used for non-Gaussian surfaces a curve fitting equation of the real probability density function. So basically, for the case of the contact between non-Gaussian surfaces, one can calculate the total contact area (A_{tot}) and the total load carried by asperities in contact (P_{tot}) by substituting the real probability density function instead of the Gaussian probability density function into equations (4.2), (4.3), (4.9)-(4.14).

The model of Kotwal and Bushan [7] covered the effect of a non-Gaussian distribution of the asperity heights. However, their model still assumed that the asperities have the same radius, which is, in fact, not true. Therefore, a deterministic contact model that takes into account the effect of non-Gaussian distribution of the asperities heights as well as the effect of asperities with different radii should be used in order to calculate the real contact of rough surfaces more accurately.

4.2.3 Deterministic contact model

As discussed above, in reality the radius of each asperity present on a surface is not the same and in many cases the asperity height distribution does not follow the Gaussian distribution. Therefore, in this thesis, a rough surface is modelled as an array of asperities with different radii and heights (deterministic model).

Nowadays, there are many kinds of commercial three dimensional surface topography measurement apparatus available, e.g. MicroMap interference microscope, ATOS, Germany (see figure 2.7a). This apparatus provides the user with digital data of the measured surface, which enables the user to treat the data using the computer. Using a good method, for example the 9-points method used by de Rooij [8], the radius and the height of every single asperity on the measured surface can be obtained. Once the data of the radius and height of each single asperity are obtained, one can determine the number of asperities in contact, the contact area and the load carried by each asperity as a function of the separation between the contacting surfaces. The total contact area and the total load can be calculated by summarizing respectively the contact area and the load carried by each individual asperity. The present model will diminish the assumption of an average radius and enable one to calculate the contact of non-Gaussian surfaces more accurately.

Suppose n asperities are present on a rough surface. It is assumed in this thesis that the asperities, at least near the summits, are spherical and the interactions among the neighbouring contacting asperities are negligible. The asperities have different radii (β_i) and heights (z_i) which are measured from a mean plane (see figure 4.2). When the rough surface approaches a flat surface,

some asperities might make contact with the flat surface (if $z_i > d$) and some might not (if $z_i < d$) depending on the separation (d) between the two surfaces (see figure. 4.2). Assuming that the deformation solely occurs at asperity level, the local indentation depth of each asperity (ω_i) is determined by:

$$\omega_i = z_i - d \tag{4.15}$$

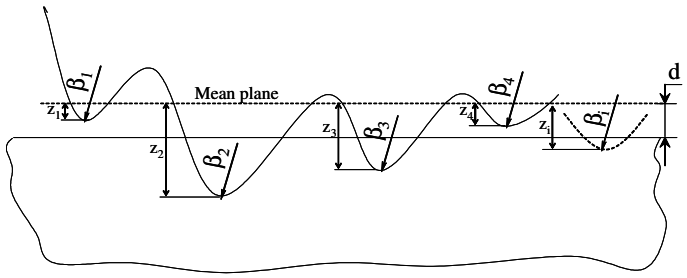

Figure 4.2: Contact model of a rough surface with a flat surface.

Depending on the indentation depth (ω_i), the contact situation of every single asperity can be elastic, elastic-plastic or plastic. Adopting the transition from the elastic to the elastic-plastic contact situation (ω_{c1}, equation 4.7) proposed by Greenwood and Williamson [1] and the transition from the elastic-plastic to the fully plastic contact situation (ω_{c2}, equation 4.8) proposed by Zhao et al. [3], the contact area of each asperity (A_i) at the elastic (A_{ie}), elastic-plastic (A_{iep}) or fully plastic (A_{ip}) contact situation can be calculated as:

$$A_i(\omega_i) = \begin{cases} A_{ie}(\omega_i) & \text{if} \quad \omega_i < \omega_{c1}(\omega_i) \\ A_{iep}(\omega_i) & \text{if} \quad \omega_{c1}(\omega_i) < \omega_i < \omega_{c2}(\omega_i) \\ A_{ip}(\omega_i) & \text{if} \quad \omega_{c2}(\omega_i) < \omega_i \end{cases} \tag{4.16}$$

where:

$$A_{ie}(\omega_i) = \pi \beta_i \omega_i \tag{4.17}$$

$$A_{iep}(\omega_i) = \pi \beta_i \omega_i \left[1 - 2\left(\frac{\omega_i - \omega_{c1}}{\omega_{c2} - \omega_{c1}} \right)^3 + 3\left(\frac{\omega_i - \omega_{c1}}{\omega_{c2} - \omega_{c1}} \right)^2 \right] \tag{4.18}$$

$$A_{ip}(\omega_i) = 2\pi \beta_i \omega_i \tag{4.19}$$

The load carried by each asperity (P_i) in the elastic (P_{ie}), elastic-plastic (P_{iep}) or fully plastic (P_{ip}) contact situation can be calculated as:

$$P_i(\omega_i) = \begin{cases} P_{ie}(\omega_i) & \text{if} \quad \omega_i < \omega_{c1}(\omega_i) \\ P_{iep}(\omega_i) & \text{if} \quad \omega_{c1}(\omega_i) < \omega_i < \omega_{c2}(\omega_i) \\ P_{ip}(\omega_i) & \text{if} \quad \omega_{c2}(\omega_i) < \omega_i \end{cases} \tag{4.20}$$

where:

$$P_{ie} = \frac{4}{3} E^* \beta_i^{0.5} \omega_i^{1.5} \tag{4.21}$$

$$P_{iep} = \left[H - 0.6H \frac{\ln \omega_{c2} - \ln \omega_i}{\ln \omega_{c2} - \ln \omega_{c1}} \right] A_{iep} \tag{4.22}$$

$$P_{ip} = H A_{ip} \tag{4.23}$$

The total real contact area (A_{tot}) and the total load (P_{tot}) carried by the interacting asperities can be calculated by summing up the individual contact areas and the loads carried by each individual asperity:

$$A_{tot} = \sum_i^n A_i \quad ; \quad P_{tot} = \sum_i^n P_i \tag{4.24}$$

4.2.4 Comparison between the statistical model and the deterministic model

To compare the statistical model and the deterministic model, two different surfaces are used with surface parameters as shown in table 4.1. These surfaces consist of asperities with different radii (β_i) and heights (z_i) relative to a mean height plane (see figure 4.3). Suppose these two rough surfaces (E_1 = 210 GPa, H_1=7.6 GPa, v_1 = 0.3) are brought into contact with a flat surface (E_2 = 210 GPa, H_2 = 7.6 GPa, v_2 = 0.3), the dimensionless separation (d/σ) as a function of dimensionless load ($P_{tot}/(A_{nom}E^*)$) calculated by the present model and the statistical model [3, 7] are presented in figure 4.4.

Table 4.1: Surface parameters of the two surfaces used.

Case	β_{avg} [m]	σ [m]	η [m^{-2}]
1	2×10^{-5}	4.8×10^{-8}	6×10^{10}
2	1.58×10^{-6}	2.63×10^{-7}	8.98×10^{10}

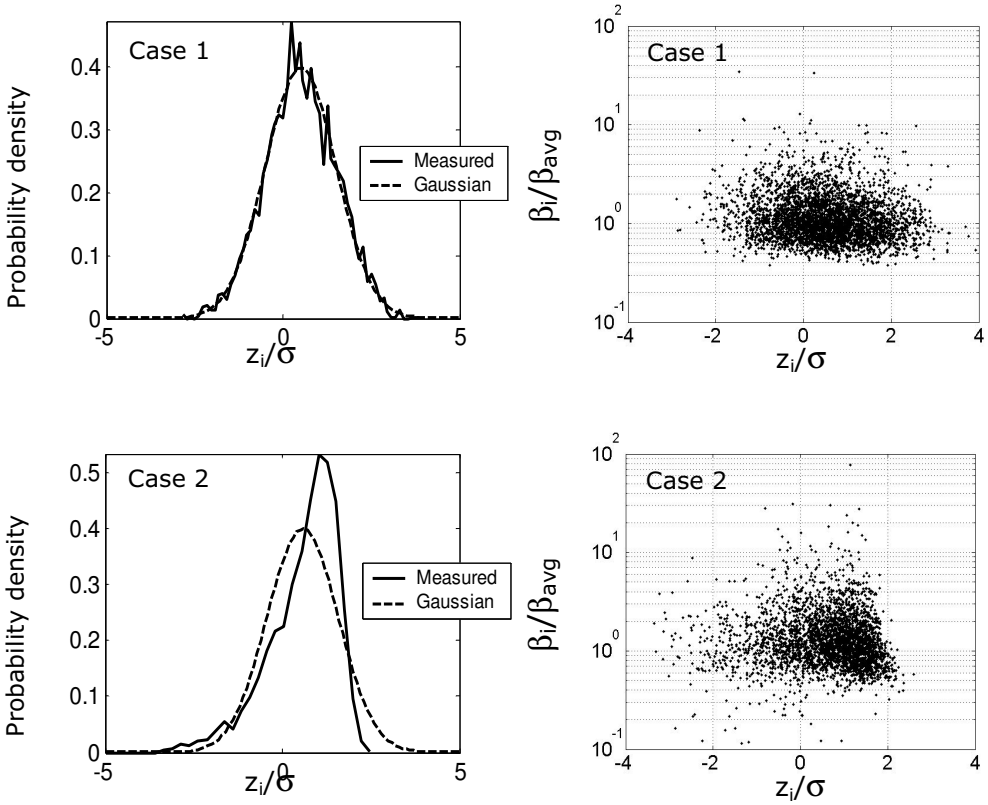

Figure 4.3: The asperity height distribution and radius distribution of the two surfaces, i.e. radius ratio (β_i/β_{avg}) as a function of normalized height (z_i/σ).

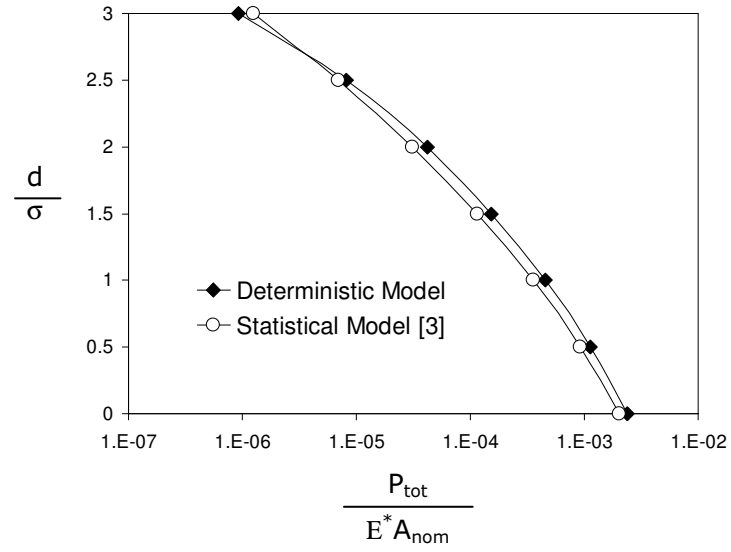

(a)

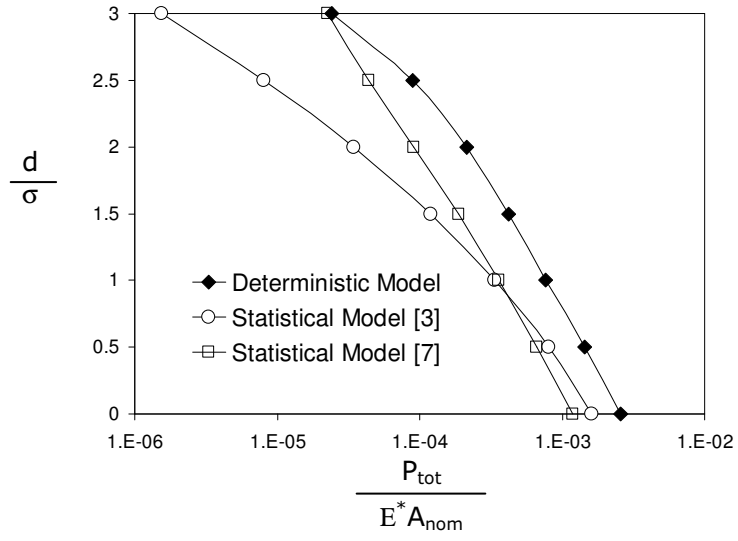

(b)

Figure 4.4: Comparison of the deterministic model and the statistical model for the two surfaces in contact with a flat surface, case 1 (a) and case 2 (b).

It is clear from figure 4.4 that for the two cases studied in this chapter, the results obtained with the deterministic model and the statistical model show a difference. The difference in calculating the separation is more pronounced (see figure 4.4b) for the non-Gaussian surface (case 2). For the non-Gaussian surface (case 2), even when the real distribution function [7] is used, the difference in calculating the standardized separation and the normalized load is significant. This is due to the fact that the asperities have different radii (see figure 4.3), therefore, each asperity has its own transition from elastic to plastic contact conditions and by this, obviously for the same indentation, the load carried and the contact area calculated by the statistical model and the deterministic model will reveal different values. Clearly, the radius of each asperity is a very important parameter and should be taken into account since assuming an average radius in analyzing the contact of rough surfaces will lead into a significant difference in calculating the separation.

4.3 Contact of a rough surface with a flat layered surface

As outlined in the previous section, in order to analyze the contact behaviour between two surfaces, one needs to know the topography and the mechanical properties (Poisson's ratio (v), elasticity modulus (E) and hardness (H)) of the contacting surfaces. Gao et al. [9] derived an analytical solution to calculate an effective Poisson's ratio (v_{eff}) of a layered surface. Further, by adopting the work of Gao et al. [9], Swain & Mecik [10] proposed a simple equation, which they also validated experimentally, to calculate an effective elasticity modulus (E_{eff}) of a layered surface. The effective hardness (H_{eff}) of a layered surface can be calculated using an equation proposed by Bhattacharaya & Nix [11], which was obtained by fitting the finite element simulations they performed. Depending on the indentation depth (ω), the values of the effective mechanical properties of a layered surface range between the value of the mechanical properties of the layer itself and the value of the mechanical properties of the substrate.

Since the three effective mechanical properties of a layered surface can be determined as a function of indentation depth, a flat layered surface can be modeled as a solid which has an effective elasticity modulus [10], effective hardness [11] and effective Poisson's ratio [9] as a function of the indentation depth. This will allow one to treat the contact of a rough surface with a flat layered surface like the contact of a rough surface with a flat surface in which the mechanical properties of the flat surface are varied as a function of the local indentation depth.

4.3.1 Contact of a sphere with a flat layered surface (single asperity model)

By assuming that the layer is perfectly bounded to the substrate, a layered surface is modelled like a solid that has effective mechanical properties ($v_{eff}(\omega)$ [9], $E_{eff}(\omega)$[10] and $H_{eff}(\omega)$ [11]) as a function of indentation depth (ω). The model is schematically illustrated in figure 4.5.

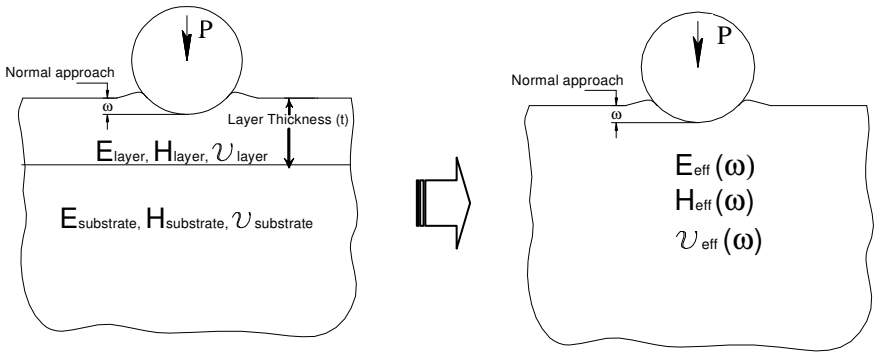

Figure 4.5: Contact model of a sphere with a flat layered surface.

4.3.1.1 Elastic contact

Swain & Mencik [10] proposed an equation to calculate an effective elasticity modulus (E_{eff}) for a layered surface based on the weight function ($I_0(\xi)$) derived by Gao et al. [9] as:

$$E_{eff}(\omega) = E_s + (E_l - E_s) I_0(\xi(\omega)) \tag{4.25}$$

where:

$$I_0(\xi(\omega)) = \frac{2}{\pi}\tan^{-1}\left(\xi(\omega)\right) + \frac{1}{2\pi(1-v_{eff}(\omega))}\left[\left(1-2v_{eff}(\omega)\right)\xi(\omega)\ln\frac{1+\xi(\omega)^2}{\xi(\omega)^2} - \frac{\xi(\omega)}{1+\xi(\omega)^2}\right] \tag{4.26}$$

with:

$$\xi(\omega) = \frac{t}{a(\omega)} \tag{4.27}$$

$$a(\omega) = \beta^{0.5}\omega^{0.5} \tag{4.28}$$

in which E_s is the elasticity modulus of the substrate E_l is the elasticity modulus of the layer, v_{eff} is the effective Poisson's ratio of a layered surface, t is the layer thickness, a is the Hertzian contact radius, β is the radius of the sphere and ω is the indentation depth.

The effective Poisson's ratio of a layered surface according to Gao et al. [9] is:

$$v_{eff}(\omega) = v_s + (v_l - v_s) I_1(\xi(\omega)) \tag{4.29}$$

with:

$$I_1(\xi(\omega)) = \frac{2}{\pi}\tan^{-1}(\xi(\omega)) + \frac{\xi(\omega)}{\pi}\ln\frac{1+\xi(\omega)^2}{\xi(\omega)^2} \tag{4.30}$$

where v_s is the Poisson's ratio of the substrate and v_l is the Poisson's ratio of the layer.

By replacing the elasticity modulus (E_2) and the Poisson's ratio (v_2) in equation (4.4) with the effective elasticity modulus ($E_{eff}(\omega)$, equation (4.25)) and the effective Poisson's ratio ($v_{eff}(\omega)$, equation (4.29)), the reduced elasticity modulus ($E^*(\omega)$) of a flat-layered surface in contact with a sphere (E_1 and v_1) can be calculated as:

$$E^*(\omega) = \frac{E_1\ E_{eff}(\omega)}{E_1(1-(v_{eff}(\omega))^2) + E_{eff}(\omega)(1-v_1^2)} \tag{4.31}$$

The contact area (A_e) and load carried (P_e) for the elastic contact situation of a sphere in contact with a flat layered surface can then be calculated as [5]:

$$A_e(\omega) = \pi\beta\omega \tag{4.32}$$

$$P_e(\omega) = \frac{4}{3}E^*(\omega)\beta^{0.5}\omega^{1.5} \tag{4.33}$$

4.3.1.2 Fully plastic contact

Bhattacharaya & Nix [11] empirically derived the effective hardness (H_{eff}) of a hard layer on a soft substrate (equation (4.34)) and for a soft layer on a hard substrate (equation (4.35)) as a function of the indentation depth (ω) as follows:

$$H_{eff}(\omega) = H_s + (H_l - H_s)\exp\left(-\frac{\sigma_{yl}E_s}{\sigma_{ys}E_l}\left(\frac{\omega}{t}\right)^2\right) \tag{4.34}$$

$$H_{eff}(\omega) = H_s + (H_l - H_s)\exp\left(-\frac{(H_l/H_s)}{(\sigma_{yl}/\sigma_{ys})(E_{yl}/E_{ys})^{0.5}}\left(\frac{\omega}{t}\right)\right) \quad (4.35)$$

where H is the hardness, E is the elasticity modulus, σ_y is the yield stress of the material, ω is the indentation depth, t is the coating thickness and subscript s and l refer to substrate and layer respectively.

The contact area (A_p) and the load carried (P_p) for the fully contact situation of a sphere in contact with a flat layered surface can be calculated as:

$$A_p(\omega) = 2\pi\beta\omega \quad (4.36)$$

$$P_p(\omega) = H_{eff}(\omega)A(\omega) \quad (4.37)$$

4.3.1.3 Elastic-plastic contact

It is assumed in this model that the layered material follows the Hertzian behaviour for the elastic contact situation as described in section 4.2. The critical indentation depth ($\omega_{c1}(\omega)$) to initiate the onset of yielding (which might be in the layer or in the substrate) then can be calculated as:

$$\omega_{c1}(\omega) = 0.89\beta\left(\frac{H(\omega)}{E^*(\omega)}\right)^2 \quad (4.38)$$

The critical indentation depth (ω_{c2}) where the fully plastic contact condition starts to occur is assumed to be the same as that of the surface without layer, thus:

$$\omega_{c2}(\omega) = c\ \omega_{c1}(\omega) \quad (4.39)$$

with c equal to 54 (see section 4.2.1)

Following the transition from the elastic to the fully plastic contact situation as proposed by Zhao et al. [3], the contact area (A_{ep}) and the load carried by the deformed layered surface (P_{ep}) for the elastic-plastic contact situation can be calculated as:

$$A_{ep}(\omega) = \pi\beta\omega\left[1 - 2\left(\frac{\omega - \omega_{c1}(\omega)}{\omega_{c2}(\omega) - \omega_{c1}(\omega)}\right)^3 + 3\left(\frac{\omega - \omega_{c1}(\omega)}{\omega_{c2}(\omega) - \omega_{c1}(\omega)}\right)^2\right] \quad (4.40)$$

$$P_{ep}(\omega) = \left[H_{eff}(\omega) - 0.6H_{eff}(\omega)\frac{\ln \omega_{c2}(\omega) - \ln \omega}{\ln \omega_{c2}(\omega) - \ln \omega_{c1}(\omega)} \right] A_{ep}(\omega) \qquad (4.41)$$

4.3.1.4 Comparison of the single asperity model with the data available in the literature [12-14]

The contact behaviour of a sphere pressed against a flat layered surface was studied experimentally by El-Shafei et al. [12], El-Sherbiney [13] and numerically by using the finite element method by Tangena [14] and Tang & Arnell [15]. The present model, in which the flat layered surface is modelled as a solid with effective mechanical properties, is used to simulate the experimental results of El-Shafei et al [12], El-Sherbiney [13] and the numerical results of Tangena [14] and Tang & Arnell [15]. The material properties, radius of the indenter and the thickness of the coating for the experiment [12, 13] and numerical simulations [14, 15] are summarized in table 4.2 and table 4.3. The normal approach and contact radius as a function of the load for the case of El-Shafei [12], the normal approach as a function of the load for the case of El-Sherbiney [13], the contact area as a function of the load for the case of Tangena [14] and the normal load and mean contact pressure as a function of the indentation depth according to Arnell & Tang [14] are calculated with the present analytical model and the results are plotted together with the experimental data [12, 13] and the numerical simulation results [14, 15] in figures 4.6, 4.7, 4.8 and 4.9 respectively. More comparison between the present model and the experimental data of El-Shafei et al. [12] and El-Sherbiney [13], the finite element simulations performed by Tangena [14] and Tang & Arnell [15] are presented in appendix C.

Table 4.2: Materials, indenter radius and coating thickness used by El-Shafei et al. [12], El-Sherbiney [13], Tangena [14] and Tang & Arnell [15].

	Material			Indenter	Coating
Reference	Indenter	Coating	Substrate	Radius (mm)	Thickness (μm)
El-Shafei et al. [12]	Steel	Lead	Steel	1.59, 3.7	0, 1.5, 3, 6,9, 12
El-Sherbiney [13]	Steel	Lead	Mild Steel	6.35, 12.75	1.2, 15
Tangena [14]	Rigid	lead	Steel	3.175	2, 4, 6
Tang & Arnell [15]	Diamond	ceramic	Steel	0.1	1, 2, 5, 10

Table 4.3: Materials properties used by El-Shafei [12], El-Sherbiney [13], Tangena [14] and Tang & Arnell [15].

	Properties								
	Indenter			Coating			Substrate		
References	E (GPa)	v [-]	H (GPa)	E (GPa)	v [-]	H (GPa)	E (GPa)	v [-]	H (GPa)
El-Shafei et al. [12]	210	0.3	7.6	18	0.35	0.17	210	0.3	7.6
El-Sherbiney [13]	210	0.3	7.6	18	0.35	0.17	140	0.3	1.86
Tangena [14]	1000	0.07	-	14	0.45	0.04	210	0.3	1.2
Tang & Arnell [15]	1141	0.07	-	400	0.3	22.5	200	0.3	7.5

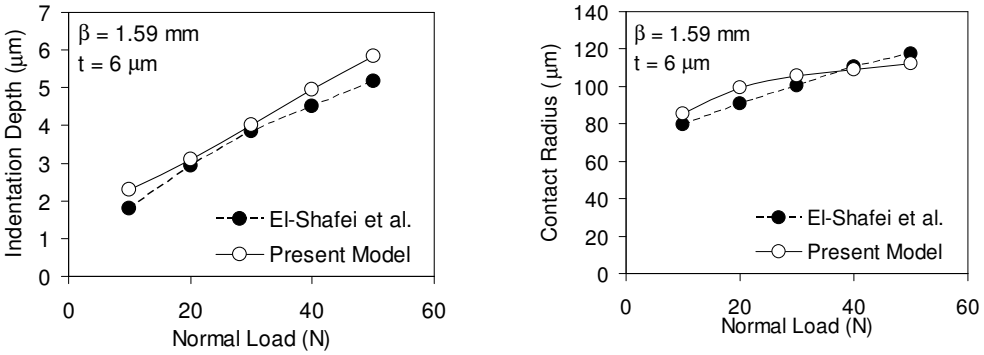

Figure 4.6: Comparison between the experimental data published by El-Shafei et al. [12] and the calculated results using the present model. See appendix C for further comparison between the present model and the experimental data published by El-Shafei et al. [12].

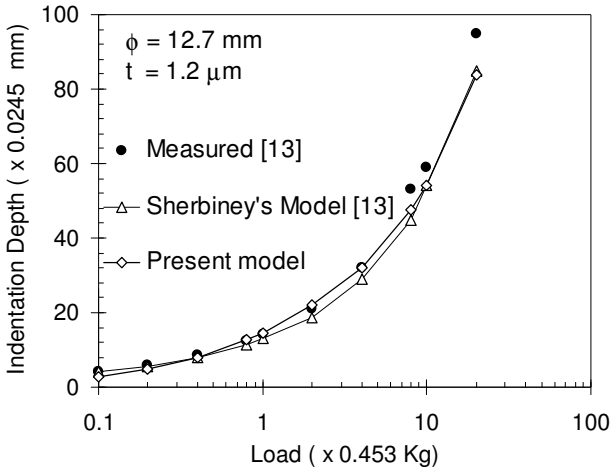

Figure 4.7: The comparison between the experimental data obtained by El-Sherbiney [13], the model of El-Sherbiney [13] and the calculated results using the present model (units along the axis are in accordance with the literature data). See appendix C for further comparison between the present model and the experimental data published by El-Sherbiney et al. [12].

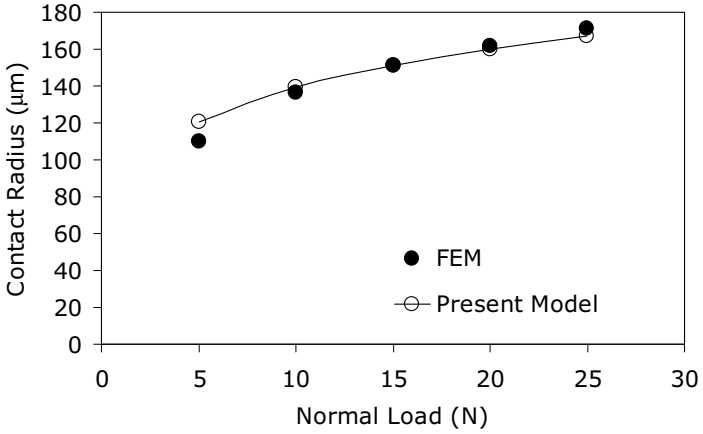

Figure 4.8: The comparison between the finite element simulations performed by Tangena [14] and the calculated results using the present model. See appendix C for further comparison between the present model and the finite element results published by Tangena [14].

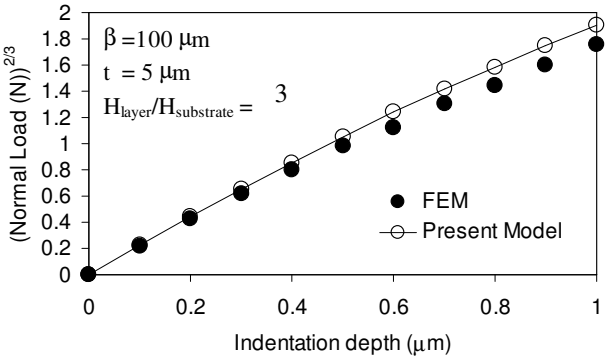

(a)

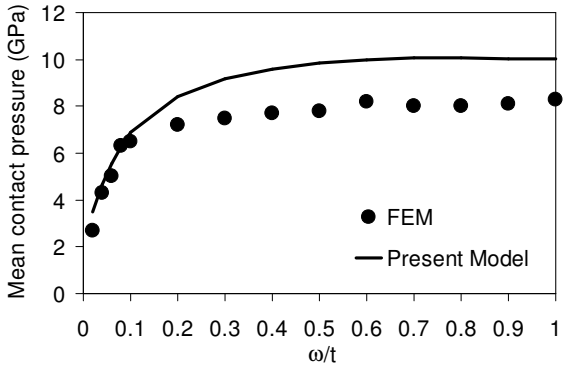

(b)

Figure 4.9: The comparison between the FEM simulations carried out by Tang & Arnell [15] and the present model, (a) normal load as a function of indentation depth (b) mean contact pressure as a function of ration between the indentation depth and the layer thickness. See appendix C for further comparison between the present model and the finite element results published by Tang and Arnell [15].

In general, as shown by figures 4.6 to 4.9, the present model is in good agreement with the experimental data reported by El-Shafei et al. [12] and El-Sherbiney [13] and the finite element simulation presented by Tangena [14] and Tang & Arnell [15]. A small deviation from the calculation is observed in the experimental data reported by El-Shafei et al. [12] and El-Sherbiney [13]. However, the experimental data reported by El-Shafei et al. [12] also reveal a certain deviation from the calculated contact area for the case of a solid without layer. The deviations from the calculations for all combinations of ball radius and layer thickness are of the same order (see appendix C). This difference is due to

the fact that in the calculation the ball is assumed to be perfectly smooth (the roughness of the ball is neglected), and therefore the measured contact area deviates from the calculated value. For the case of finite element simulations performed by Tangena [14], the calculated contact areas of a lead and gold layer on steel using the present model (see appendix C) fit nicely to the finite element simulations results. However, the contact areas of a silver layer on steel calculated using the present model deviate from the results of the finite element simulations. This is due to the fact that Tangena [14] assumed in his simulation that the layer is elastic, and for the case of the silver layer, this assumption is not really valid since silver has a higher hardness value compared to lead and gold. For the same normal load, Tang & Arnell [15] calculated a slightly deeper indentation depth than the indentation depth calculated using the present model.

To calculation friction, the necessary parameters to be calculated are the contact area (to determine the force needed to shear the contact due to adhesion), the deformation (to determine the force needed to plough through a plastically deforming surface) and the mean contact pressure (if the interfacial shear strength is dependent of the mean contact pressure). These three values, for the case of a sphere pressed against a flat layered surface, can be predicted quite well with the present model. Therefore, the presented analytical model of a sphere in contact with a flat layered surface can be extended to contact of a rough surface against a flat layered surface as discussed in the following section and can also be extended to calculate the friction of a rough surface sliding against a flat layered surface (see chapter 5).

4.3.2 Contact of a rough surface with a flat layered surface

Suppose a rough surface is in contact with a flat layered surface as shown in figure 4.10a. The flat layered surface is modeled as a solid which has effective mechanical properties as described in section 4.3.1 (see figure 4.10b). Suppose a large number of asperities is present at the rough surface, and it is assumed that the asperities are, at least at near the summits, spherical with different radii (β_i) and height (z_i). Hence, for a certain separation (d), assuming that there is no interaction between the neighbouring asperities, one can determine the indentation depth of each asperity ($\omega_i = z_i - d$) and calculate the contact area and the load carried by each individual asperity in contact. The total contact area (A_{tot}) and the total load carried (P_{tot}) are then calculated by summing up respectively the contact area and the load carried by each asperity:

$$A_{tot} = \sum_{ie}^{n} A_{ie} + \sum_{iep}^{n} A_{iep} + \sum_{ip}^{n} A_{ip} \qquad (4.42)$$

$$P_{tot} = \sum_{ie}^{n} P_{ie} + \sum_{iep}^{n} P_{iep} + \sum_{ip}^{n} P_{ip} \tag{4.43}$$

$$n = n_{ie} + n_{iep} + n_{ip} \tag{4.44}$$

where n is the number of asperities in contact and subscripts e, ep and p correspond to elastic, elastic-plastic and plastic contacts respectively.

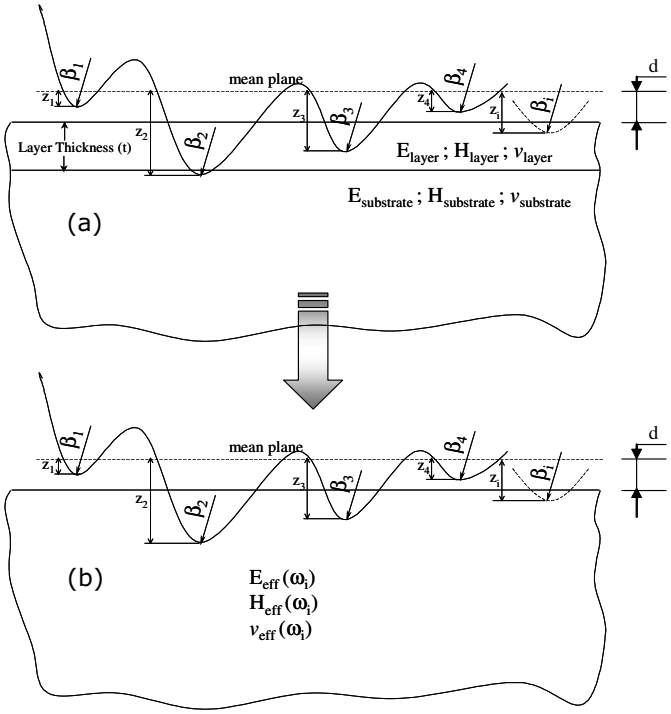

Figure 4.10: Contact model of a rough surface with a flat layered surface.

4.3.3. Results

Suppose a flat surface (E_s = 210 GPa, H_s = 7.6 GPa, v_s=0.3) is covered with a variable thick lead layer (E_l = 18 GPa, H_l = 0.17 GPa, v_l = 0.35). If this flat layered surface is brought into contact with the two rough surfaces listed in table 4.1 (E_1 = 210 GPa, H_1 = 7.6 GPa, v_1 = 0.3), the dimensionless separation (d/σ) and the dimensionless contact area (A_{tot}/A_{nom}) as a function of

dimensionless load ($P_{tot}/(A_{nom}E^*_{t=0})$) for the two cases studied in this chapter (see table 4.1) are shown in figure 4.11.

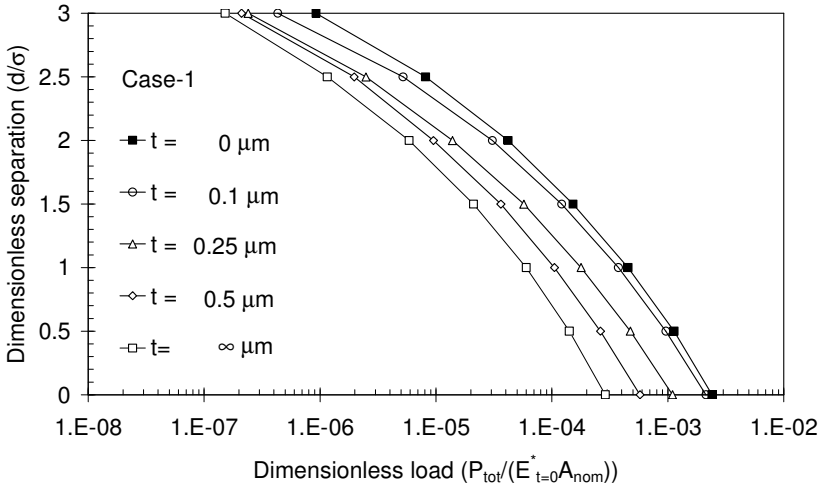

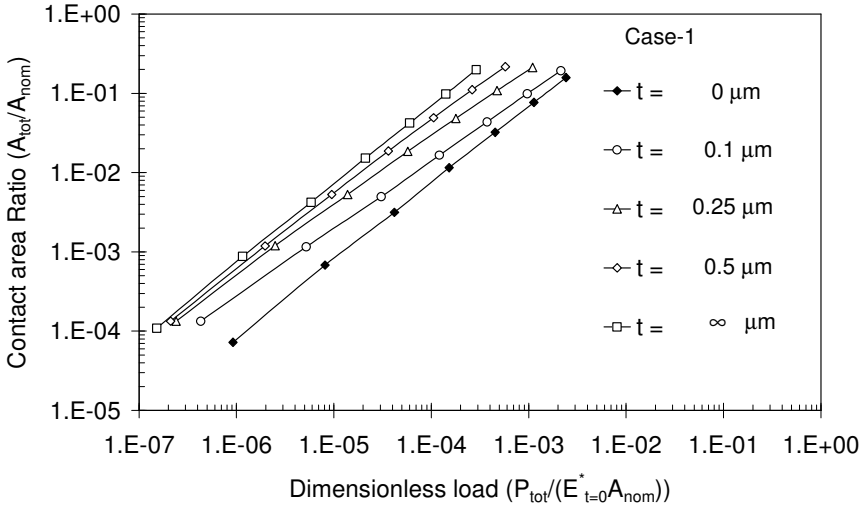

Figure 4.11a: Dimensionless separation (d/σ) and dimensionless real contact area (A_{tot}/A_{nom}) as a function of dimensionless load ($P_{tot}/(A_{nom}E^*_{t=0})$) for various thicknesses (t) of lead layer on a flat surface in contact with a rough surface (case 1).

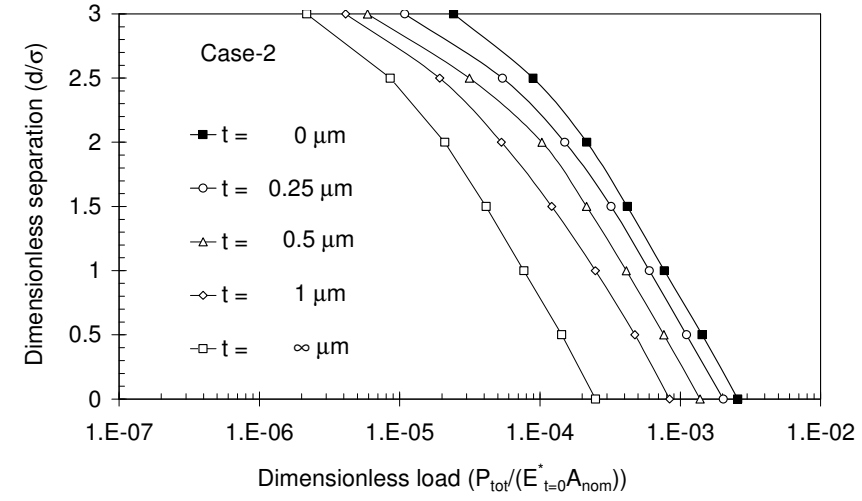

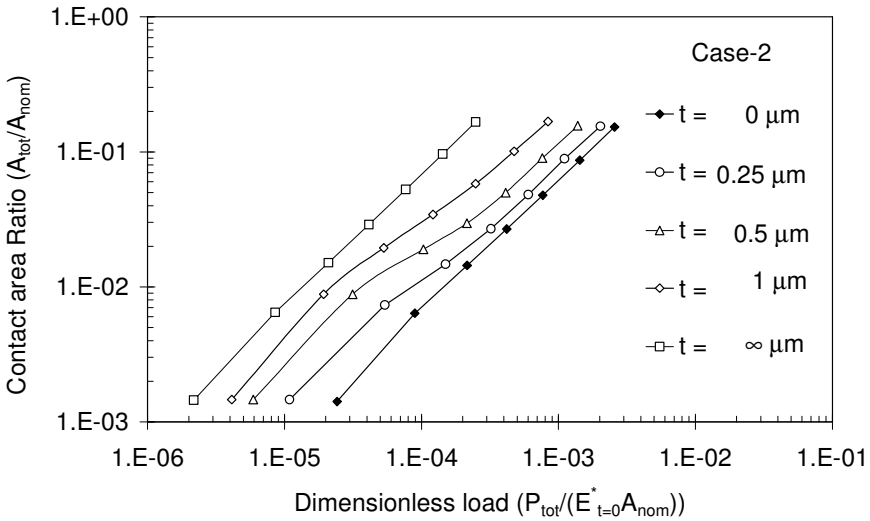

Figure 4.11b: Dimensionless separation (d/σ) and dimensionless real contact area (A_{tot}/A_{nom}) as a function of dimensionless load ($P_{tot}/(A_{nom}E^*_{t=0})$) for various thicknesses (t) of lead layer on a flat surface in contact with a rough surface (case 2).

Figure 4.11 clearly shows that as the steel surface is coated by a certain thickness of lead layer, the value of the dimensionless separation as a function of dimensionless load of the layered system should be between the value of the system without layer (t = 0) and of the system with a very thick layer (t = ∞). Intuitively, one will observe that as the load increases, the indentation depth becomes larger, i.e. the separation is smaller and the contact area for various thicknesses of layer is closer to the value of that of the substrate without a layer. These results show that the effect of the substrate in controlling the contact behaviour is more pronounced as the asperities penetrate deeper into the layer.

4.4. Concluding remarks

A deterministic contact model of a rough surface against a flat layered surface is presented in this chapter. As for the case of a sphere pressed against a flat layered surface (single asperity model), the proposed model shows good agreement with the experimental and the numerical results, one can extend the single asperity model to calculate the contact of a rough surface with a flat layered surface by analysing the contact of each individual asperity (deterministic model). The deterministic contact model allows one to analyse the contact of non-Gaussian surfaces and eliminate the assumption of an average asperity radius, which makes the calculation of the contact area and the load carried more accurate. Based on this deterministic model, a deterministic friction model will be developed and discussed in the following chapter.

References

[1] J.A. Greenwood and J.B.P. Williamson, Contact of nominally flat surface, Proceeding of Royal Society London, Series A 295 (1966) 300-319.

[2] Z.H. Powierza, T. Klimczak and A. Polijanniuk, On the experimental verification of the Greenwood-Williamson model for the contact of rough surfaces, Wear 32 (1992) 115-124.

[3] Y. Zhao, D.M. Maietta and L. Chang, An asperity microcontact model incorporating the transition from elastic deformation to fully plastic flow, ASME Journal of Tribology, 122 (2000) 86-93.

[4] D. Tabor, The hardness of metals, Oxford University Press, 1951.

[5] K.L. Johnson, Contact mechanics, Cambridge University Press, 1995.

[6] R.L. Jackson and I. Green, A finite element study of elasto-plastic hemispherical contact, Proceedings of 2003 STLE/ASME Joint Tribology Conference, 2003TRIB-268, 2003.

[7] C.A. Kotwal and B. Bhushan, Contact analysis of non-Gaussian surfaces for minimum static and kinetic friction and wear, Tribology Transactions, 39 (1996), 890-898.

[8] M.B. de Rooij, Tribological aspects of unlubricated deepdrawing processes, PhD Thesis, University of Twente, 1998.

[9] H. Gao, C. Chui and J. Lee, Elastic contact versus indentation model of multi-layered material, International Journal of Solids and Structures, 29 (1992) 2471-2492.

[10] M.V. Swain and J. Mencik, Mechanical characterization of thin films using spherical tipped indenters, Thin Solid Films, 253 (1994) 204-211.

[11] A.K. Bhattacharaya and W.D. Nix, Analysis of elastic and plastic deformation associated with indentation testing of thin films on substrates, International Journal of Solids and Structures, 24 (1988) 1287-1298.

[12] T.E.S. El-Shafei, R.D. Arnell and J. Halling, An experimental study on the Hertzian contact of surfaces covered by soft metal films," ASLE Transaction 26 (1983) 481-486.

[13] M.G.D. El-Sherbiney, Tribological properties of ion-plated thin-metallic films, PhD Thesis, University of Salford, England, 1975.

[14] A.G. Tangena, Tribology of thin film systems, PhD Thesis, University of Eindhoven, The Netherlands, 1987.

[15] K.C. Tang and R.D. Arnell, Determination of coating mechanical properties using spherical indenters, Thin Solid Films, 355-356 (1999) 263-269.

Chapter 5
Deterministic Friction Model of a Rough Surface Sliding against a Flat Layered Furface

5.1. Introduction

In chapter 4, an analytical model is developed to describe locally the contact behaviour of a rough surface with a flat layered surface. In this chapter, the deterministic contact model described in chapter 4 is extended to a deterministic friction model by analyzing locally the resistance to motion experienced by each asperity for the elastic, elastic-plastic and fully plastic contact situations. These are then summarized as the total friction force, as will be outlined in the following sections.

5.2. Friction of layered surfaces

Dry sliding contact applications require low friction and high wear resistant material combinations to increase the efficiency of these systems. A low friction system can be achieved by having hard materials to support the normal load and a weak interface between the two opposing surfaces to provide easy shear. This idea can be implemented by covering a hard substrate with a soft thin layer or creating a self lubricating composite like zirconia doped with CuO (as discussed in chapter 3) that can generate a soft interfacial layer due to the high contact pressure during sliding contact.

Bowden and Tabor [1] performed experiments on a steel rider with radius 3 mm sliding against various thicknesses of indium layers on steel. They observed that the coefficient of friction of a layered surface varied as a function of the layer thickness (see figure 5.1). For a very thin layer, according to Bowden and Tabor [1], the coefficient of friction of the layered system is about the same as that of the substrate without a layer. As the thickness of the layer increases, the coefficient of friction is reduced to an optimum value after which the coefficient of friction increases again, and for a very thick layer, the value of the coefficient of friction is the same as that of the layer material when used as a bulk material. Therefore, the layer thickness is an important parameter need to be optimized in order to obtain a low friction tribosystem. This means that a

friction model is needed to describe the relation between the coefficient of friction and the layer thickness.

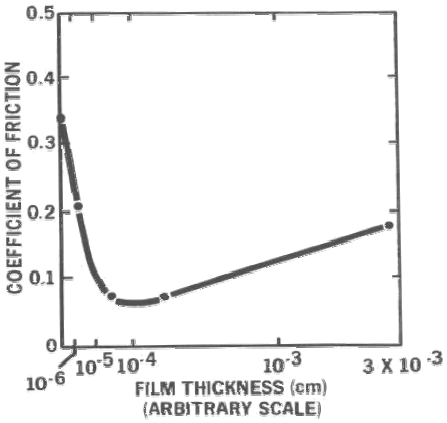

Figure 5.1: Experimental results of Bowden and Tabor [1].

5.3 Halling's Model

Halling [2] developed an analytical friction model of a flat layered surface sliding against a rough surface based on the adhesion theory of Bowden and Tabor [1]. Halling [2] assumed that when a rigid rough surface is in contact with a flat layered surface, all the local contacts are plastic. For the case of a soft layer on a hard substrate, some asperities might penetrate through the layer and have contact with the substrate (see figure 5.2). Halling [2] further assumed that the resistance to motion is only caused by the shear strength of the material in the contact and the effect of ploughing is neglected.

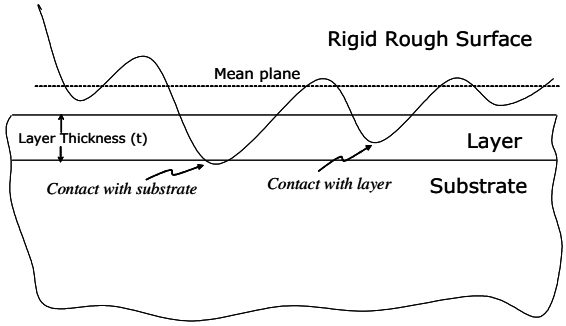

Figure 5.2: Schematic model of Halling [2].

Based on the aforementioned assumptions, the coefficient of friction (f) of a layered surface in contact with a rough surface according to Halling [2] is:

$$f = \frac{\sum_{is} \tau_{is} A_{is} + \sum_{il} \tau_l A_l}{\sum_{is} H_s A_s + \sum_{il} H_e A_l} \tag{5.1}$$

where τ is the interfacial shear strength, A is the contact area, H is the hardness, i is the number of asperities in the contact region, H_e is the effective hardness of the substrate covered by a certain layer thickness, subscripts s and l denote the substrate and the layer respectively.

According to Halling [2], the effective hardness of a layered substrate can be calculated as follows:

$$H_e = H_l + (H_s - H_l)\exp\left(-\frac{ct}{\beta}\right) \tag{5.2}$$

where β is the radius of the asperity, t is the thickness of the layer and c is an empirical constant.

Halling's model [2] showed that the friction of a layered surface varied as a function of the layer thickness, by which one can determine the optimum layer thickness to reduce friction. It is also observed and explained by Halling in his model that for a very thin layer ($t \approx 0$) the coefficient of friction should be the same as that of the substrate without a layer ($f = f_s$) and for a very thick layer the coefficient friction should be the same as that of the layer ($f = f_l$) as also observed by Bowden and Tabor [1].

5.4. Deterministic friction model

As mentioned above that Halling's contact model was based on the assumption that both the layer and the substrate deform plastically, and as a consequence this model is not applicable to predict friction in the elastic and the elastic-plastic contact situations. So, by adding the components of elastic and elastic-plastic contact situations to the model, one could predict more accurately the friction of layered surfaces. In addition, in his model Halling only considered the contribution of adhesion in calculating the friction force. In fact, for the plastic contact situation, a harder asperity will plough through the deforming surface and consequently the asperity experiences resistance to motion (friction force due to ploughing). This idea will be discussed further in the following section.

5.4.1. Contact area of a moving asperity

At static contact, the situation of each single asperity on a rough surface in contact with a flat layered surface can be determined based on the deterministic model described in chapter 4. However, when an asperity starts to move on a plastically deforming surface, the contact area that carries the load ($A_m=\pi\beta\omega_m$) is initially only half of the contact area at the static condition ($A_{st}=2\pi\beta\omega_{st}$). Therefore, the asperity tends to sink deeper ($\omega_m = 2\omega_{st}$) into the plastically deforming surface in order to balance the normal load. When an asperity starts to move on an elastically deforming surface, the contact area during motion is in fact slightly changed due to friction. In this model, the dynamic elastic contact area is assumed to be equal to the static elastic contact area. For the elastic-plastic contact situation of moving asperities, the contact area is assumed to change as shown in figure 5.3. Based on these assumptions, the contact area of a moving asperity in an elastic (A_{iem}), elastic-plastic (A_{iepm}) or fully plastic (A_{ipm}) contact situation can be calculated as follows:

$$A_{iem}(\omega_{im}) = A_{iepm}(\omega_{im}) = A_{ipm}(\omega_{im}) = \pi\beta_i\,\omega_{im} \tag{5.3}$$

with:

$$\omega_{im} = z_i - d \tag{5.4}$$

in which ω_{im} is the penetration depth of the moving asperity, z_i is the height of the asperity measured from the mean plane and d is the separation between the flat surface to the mean height line of the rough surface (see figure 4.10).

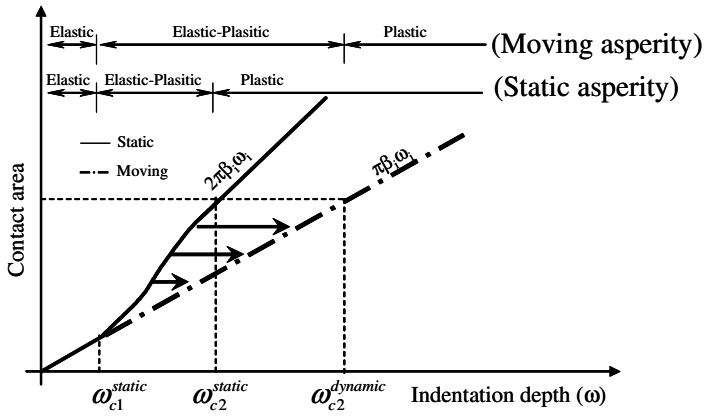

Figure 5.3: Contact area of a single static and moving asperity.

Accordingly, the load carried by moving asperities in the elastic (P_{iem}), elastic-plastic (P_{iepm}) and fully plastic (P_{ipm}) contact situations can be calculated as follows:

$$P_{iem}(\omega_{im}) = \frac{4}{3} E^* \beta_i^{0.5} \omega_{im}^{1.5} \tag{5.5}$$

$$P_{iepm}(\omega_{im}) = \left[H_{eff}(\omega_{im}) \left\{ 1 - 0.6 \frac{\ln \omega_{c2}(\omega_{im}) - \ln \omega_{im}}{\ln \omega_{c2}(\omega_{im}) - \ln \omega_{c1}(\omega_{im})} \right\} \right] \times A_{iepm}(\omega_{im}) \tag{5.6}$$

$$P_{ipm}(\omega_{im}) = H_{eff}(\omega_{im}) A_{ipm}(\omega_{im}) \tag{5.7}$$

5.4.2. Calculation of the separation (d)

For a certain applied normal load (P), an iteration procedure should be performed to determine the corresponding separation of the two contacting surfaces to balance the normal load at the dynamic contact situation. The iteration starts (see figure 5.4) by guessing the value of the separation by which one can determine the penetration depth of each asperity. By using equations 5.5, 5.6 and 5.7, the load carried by each asperity can be calculated and summarized as the total normal load carried by the moving asperities. The guessed value of separation should be increased if the calculated total load carried by the asperities is more than the applied load or vice versa. The iteration continues until the normal load is balanced, i.e.:

$$P = P_{tot}(\omega_{im}) = \sum_{ie} P_{ie}(\omega_{im}) + \sum_{iep} P_{iep}(\omega_{im}) + \sum_{ip} P_{ip}(\omega_{im}) \tag{5.8}$$

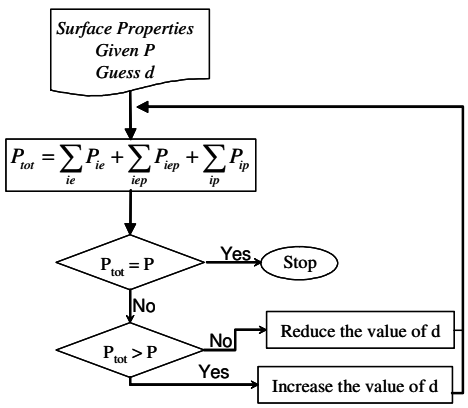

Figure 5.4: Iteration procedure to determine the value of the separation between the opposing surfaces for a corresponding given load.

5.4.3. Contact with substrate and layer ($\omega_i > t$)

Sherbiney [3] performed friction tests of balls covered with lead sliding against steel discs. He observed the evidence that the hard asperity might penetrate through the layer and make contact with the substrate. This condition is schematically shown in figure 5.5. Based on the observation of Sherbiney [3], for the case of a soft layer on a hard substrate, it is assumed in this model that when the indentation depth (ω_i) of an asperity is less than the layer thickness, the asperity makes contact only with the layer whereas when the penetration depth is more than the layer thickness, part of the asperity is in contact with the layer and the remaining part is in contact with the substrate. So, after the calculation of the separation (explained in section 5.4.2) is carried out, the model is transformed back to the real condition. Based on the aforementioned assumption, the number of asperities in contact with the layer and the number of asperities that penetrate through the layer and make contact with the substrate and layer can be determined.

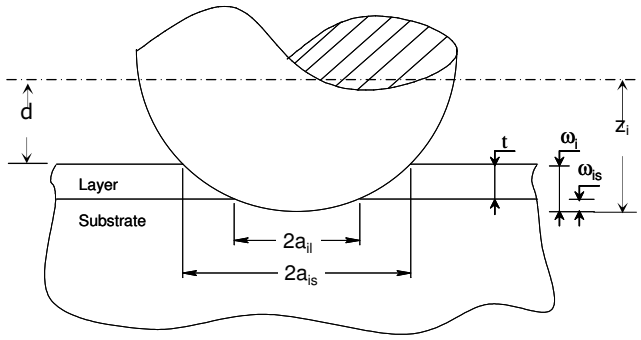

Figure 5.5: Schematic representation of an asperity penetrating through the surface layer.

The contact area (A_{iel}, A_{iepl}, A_{ipl}) and the load carried (P_{iel}, P_{iepl}, P_{ipl}) by the asperities that are only in contact with the layer are similarly obtained as the contact area (A_{ie}, A_{iep}, A_{ip}) and the load carried by asperity (P_{ie}, P_{iep}, P_{ip}) as discussed in section 5.4.1:

$$A_{iel} = A_{iem} \; ; A_{iepl} = A_{iepm} \; ; A_{ipl} = A_{ipm} \tag{5.9}$$

$$P_{iel} = P_{iem} \; ; P_{iepl} = P_{iepm} \; ; P_{ipl} = P_{ipm} \tag{5.10}$$

For asperities that penetrate through the layer and make contact with the substrate, some part of the load will be carried by the substrate and the layer will carry the remaining part. The amount of load carried by the substrate and the amount of load carried by the layer depends on the indentation depth of the

individual asperity into the substrate (ω_{is}). The indentation depth of an asperity into the substrate is defined as:

$$\omega_{is} = z_i - (d + t) \tag{5.11}$$

Depending on the value of ω_{is} the contact condition with the substrate can be elastic, elastic-plastic or fully plastic. The load carried by the substrate for the elastic (P_{ies}), elastic-plastic (P_{ieps}) or fully plastic condition (P_{ips}) respectively can be calculated as follows [4]:

$$P_{ies}(\omega_{is}) = \frac{4}{3} E_s^* \beta_i^{0.5} \omega_{is}^{1.5} \tag{5.12}$$

$$P_{ieps}(\omega_{is}) = \left[H_s - 0.6 H_s \frac{\ln \omega_{c2s} - \ln \omega_{is}}{\ln \omega_{c2s} - \ln \omega_{c1s}} \right] \times \left(\pi \beta_i \omega_{is} \left[1 - 2 \left(\frac{\omega_{is} - \omega_{c1s}}{\omega_{c2s} - \omega_{c1s}} \right)^3 + 3 \left(\frac{\omega_{is} - \omega_{c1s}}{\omega_{c2s} - \omega_{c1s}} \right)^2 \right] \right) \tag{5.13}$$

$$P_{ips}(\omega_{is}) = 2\pi \beta_i \omega_{is} H_s \tag{5.14}$$

with:

$$E_s^* = \frac{E_1 \; E_s}{E_1 (1 - v_s^2) + E_s (1 - v_1^2)} \tag{5.15}$$

$$\omega_{c1s} = 0.89 \beta_i \left(\frac{H_s}{E_s^*} \right)^2 \quad ; \quad \omega_{c2s} = 54 \omega_{c1s} \tag{5.16}$$

The contact areas of a moving asperity in contact with the substrate in the elastic (A_{ies}), elastic-plastic (A_{ieps}) or fully plastic (A_{ips}) condition are then written as:

$$A_{ies} = A_{ieps} = A_{ips} = \pi \beta_i \omega_{is} \tag{5.17}$$

So, as the total normal load (P_i) carried by an asperity that penetrate through the layer is known from the calculation of the separation (d) as described in section 5.3.2, the part of the load carried by the substrate can be calculated by using equations (5.12)-(5.14), and the remaining part of the total load carried by an asperity that penetrate through the layer, which is carried by the layer (P^s_{il}), can simply be calculated as:

$$P_{il}^{s} = P_i - \begin{cases} P_{ies} & , \text{if } \omega_{is} < \omega_{c1s} \\ P_{ieps} & , \text{if } \omega_{c2s} > \omega_{is} \geq \omega_{c1s} \\ P_{ips} & , \text{if } \omega_{is} \geq \omega_{c2s} \end{cases} \tag{5.18}$$

Accordingly, for the case of an asperity penetrating through the layer, the contact area with the substrate can be determined using equation (5.17) and the remaining contact area with the layer (A^{s}_{il}) can be calculated as:

$$\begin{aligned} A_{il}^{s} &= A_i - \begin{cases} A_{ies} & , \text{ if } \omega_{is} < \omega_{c1s} \\ A_{ieps} & , \text{ if } \omega_{c2s} > \omega_{is} \geq \omega_{c1s} \\ A_{ips} & , \text{ if } \omega_{is} \geq \omega_{c2s} \end{cases} \\ &= A_i - \pi\beta_i\omega_{is} \end{aligned} \tag{5.19}$$

Therefore, the total contact area with the layer can be calculated as:

$$A_l = \sum_{iel} A_{iel} + \sum_{iepl} A_{iepl} + \sum_{ipl} A_{ipl} + \sum_{is} A_{il}^{s} \tag{5.20}$$

and the total contact area with the substrate is:

$$A_s = \sum_{ies} A_{ies} + \sum_{ieps} A_{ieps} + \sum_{ips} A_{ips} \tag{5.21}$$

The total real contact area is then:

$$A_{tot} = A_l + A_s \tag{5.22}$$

5.4.4 Friction force due to adhesion

The dynamic contact model described in the previous section enables one to calculate the contact area of each asperity (A_i) in contact. If the interfacial shear strength of each asperity in contact with the substrate and the layer in the elastic (τ_e), elastic-plastic (τ_{ep}) and fully plastic (τ_p) contact situations can be determined or measured, then the friction force due to adhesion can be calculated by:

$$\begin{aligned} F_{ad} = &\sum_{iesm} \tau_{ies} A_{iesm} + \sum_{iepsm} \tau_{ieps} A_{iepsm} + \sum_{ipsm} \tau_{ips} A_{ipsm} + \\ &+ \sum_{ielm} \tau_{iel} A_{ielm} + \sum_{ieplm} \tau_{iepl} A_{ieplm} + \sum_{iplm} \tau_{ipl} A_{iplm} + \sum_{ism} \tau_{ipl} A_{ilm}^{s} \end{aligned} \tag{5.23}$$

5.4.5 Friction force due to ploughing

When a spherical asperity is in contact with the substrate or the layer in a fully plastic condition, the resistance to motion will also be determined by ploughing through the softer material. A schematic representation of the ploughing phenomenon is shown in figure 5.6.

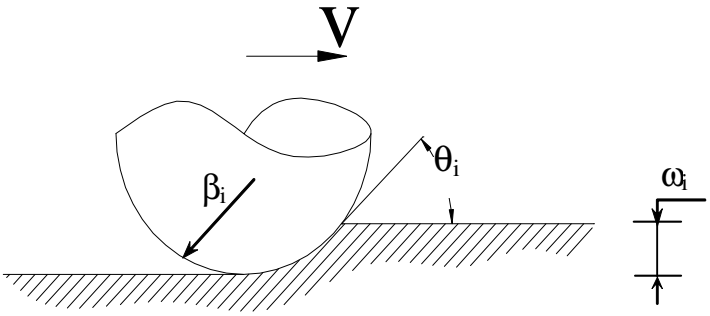

Figure 5.6: Schematic representation of the resistance due to ploughing of a rigid asperity through a plastically deforming surface.

For a certain attack angle (θ_i), the coefficient of friction of a rigid asperity ploughing through a plastically deforming surface can be calculated on the basis of the work of Komvopoulos et al. [5] as:

$$f_{ipl} = \frac{2}{\pi}\frac{\theta_i - \sin\theta_i \cos\theta_i}{\sin^2\theta_i} \tag{5.24}$$

where θ_i can be estimated geometrically as:

$$\theta_i = \begin{cases} \tan^{-1}\left(\dfrac{\sqrt{\omega_i(2\beta_i - \omega_i)}}{\beta_i - \omega_i}\right) & \text{if} \quad \omega_i < \beta_i \\ \dfrac{\pi}{2} & \text{if} \quad \omega_i \geq \beta_i \end{cases} \tag{5.25}$$

In an elastic-plastic contact situation, a harder asperity also experiences resistance to motion due to ploughing. The value of the ploughing force in the elastic-plastic contact situation depends on the penetration depth. When the penetration depth is close to the transition value of the elastic-plastic to the fully plastic contact situation, the coefficient of friction should be close to the coefficient of friction as calculated using equation (5.24), whereas when the penetration depth is close to the transition value of the elastic to the elastic-plastic contact situation, the coefficient of friction due to ploughing is close to zero. Therefore, equation (5.24) can be written in a general form as:

$$f_i = \chi(\omega_i)\frac{2}{\pi}\frac{\theta_i - \sin\theta_i \cos\theta_i}{\sin^2\theta_i} \tag{5.26}$$

where $\chi(\omega_i)$ is defined by:

$$\chi(\omega_i) = \begin{cases} 1 & \text{if} \quad \omega_i > \omega_{c2} \\ \dfrac{\omega_i}{c\,\omega_{c1}} & \text{if} \quad \omega_{c1} < \omega_i < \omega_{c2} \\ 0 & \text{if} \quad \omega_i < \omega_{c1} \end{cases} \tag{5.27}$$

The corresponding friction force due to ploughing can be calculated as follows:

$$F_{ipl} = \sum_i^n f_i \times P_i \tag{5.28}$$

5.4.6 The total friction force

Assuming that the resistances to motion are due to adhesion (F_{ad}) and ploughing (F_{pl}) only, the total friction can be calculated as:

$$F_{tot} = F_{ad} + F_{pl} \tag{5.29}$$

and the coefficient of friction is then calculated as:

$$f = \frac{F_{tot}}{P} \tag{5.30}$$

5.4.7 Friction of a plastically deforming substrate and plastically deforming surface layer

For the case of a plastically deforming layer on plastically deforming substrate, the present model will yield to the model of Halling [2], by assuming that the friction is only caused by adhesion. For this case, the major difference between the present model and the model of Halling [2] is only the way of determining the effective hardness of the layered surface. The present model calculates the effective hardness based on the work of Battacharaya & Nix [6] in which the effective hardness changes as a function of indentation depth while Halling [2] determines the effective hardness only as a function of the layer thickness and the average radius of the asperities while the effective hardness does not change as a function of the indentation depth (see equation 5.2). The advantage of the equation used to calculate the effective hardness as proposed by Battacharaya & Nix [6] is that it only contains the mechanical properties of the

layer and the substrate and does not contain any constant that must be obtained experimentally. The difference in determining the effective hardness of the layered surface will certainly lead to a different value of the contact area and indentation depth at plastic contact particularly when the penetration depth is less than the layer thickness. This effect is described in greater detail in section 5.5.

5.5. Results

5.5.1. Soft layer on hard substrate

Sherbiney [3] performed friction tests on ion plated lead and indium deposited on 6.35 mm diameter hardened steel balls sliding against a hardened steel disc. The properties of the material used by Sherbiney [3] are listed in table 5.1.

Table 5.1: Material properties used (measured by Sherbiney [3]).

Materials	Elasticity Modulus (GPa)	Hardness (GPa)	Poisson Ratio
Hardened steel	200	9.6	0.3
Lead (layer)	18	0.17	0.35
Indium (layer)	11	0.09	0.35

It was observed by Sherbiney [3] that the height of the asperities on the tested surfaces had a Gaussian distribution. The average radius (β_{ave}) of the asperities was reported to be equal to 10 μm and the combined standard deviation (σ) of the two surfaces in contact is 0.14 μm. Unfortunately, the population (η) of the asperities in contact was not reported in his work. Johnson [7] reported that the value of $\eta\beta\sigma$ ranged from 0.03 to 0.05. Based on the observation of Johnson [7], the friction calculation results presented here are based on $\eta = 2.85 \times 10^{10}$ asperities/m^2 or $\eta\beta\sigma$ equal to 0.04. With all the surface parameters described above, a number of asperities can be generated by using the standard Gaussian distribution equation. The apparent contact area can be calculated using the static contact situation of a ball against a flat layered surface as described in section 4.3.1.

As the number of asperities is known, and the heights and the radii, then the calculation of friction due to adhesion and ploughing can be calculated using the equations described in sections 4.3.4 and 4.3.5. To determine the value of the interfacial shear strength the following assumption was used based on the observation of Halling [2] and Bowden & Tabor [1]. When the layer is very thin, many asperities penetrate through the layer and make contact with the substrate. Therefore, for the situation where the contact area is dominated

by the contact of the asperities with the substrate, the coefficient of friction is assumed to be equal to the coefficient of friction of the substrate without a layer. It is also assumed that for a very thick layer, the coefficient of friction is equal to that of the layer used as bulk material.

The coefficient of friction of hardened steel against hardened steel was reported by Sherbiney [3] to be about 0.45, therefore the interfacial shear strength for the elastic contact situation can be estimated. Accordingly, the coefficient of friction of a very thick lead and indium layer on steel against steel is about 0.15 [3]. Hence, the interfacial shear strength can also be estimated. The coefficient of friction as a function of layer thickness of various lead and indium thicknesses on hardened steel can be calculated and the results are plotted together with the results obtained from Halling's model in figures 5.7 and 5.8.

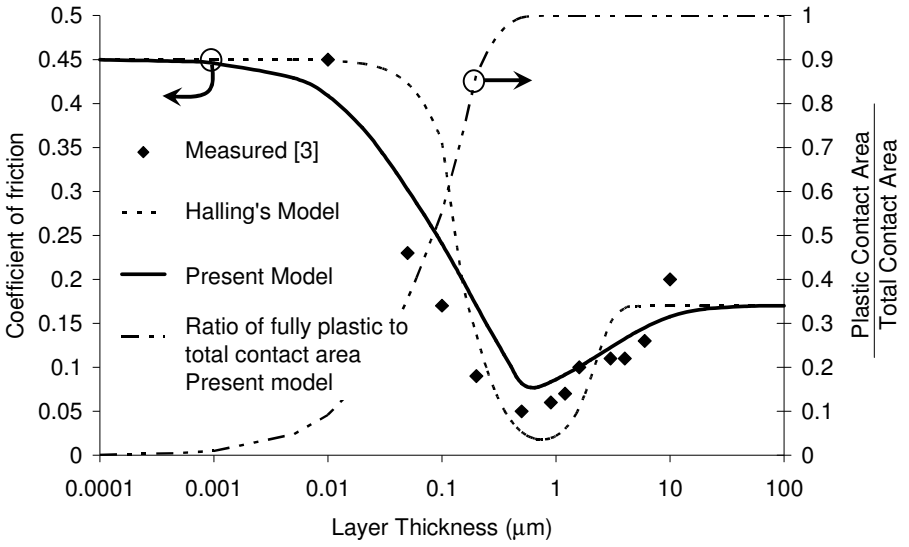

Figure 5.7: Coefficient of friction as a function of layer thickness of a *lead* layer on a hardened steel substrate sliding against hardened steel.

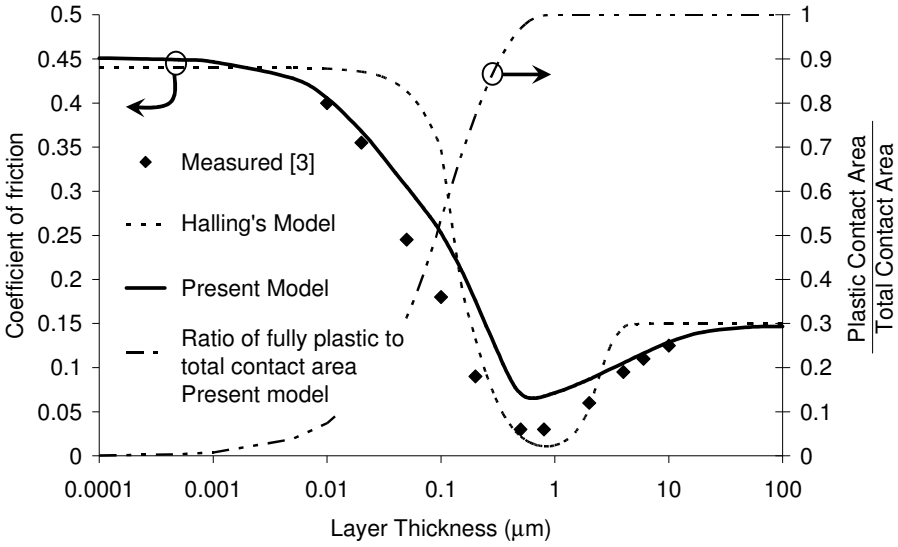

Figure 5.8: Coefficient of friction as a function of layer thickness of an *indium* layer on a hardened steel substrate sliding against hardened steel.

5.5.2. Hard layer on soft substrate

In the work of Wang & Kato [8], silicon substrates were covered with various thicknesses of carbon nitride layers. The layered surfaces were tested against a 10 μm radius diamond indenter. The applied normal load was 80 mN. In their work, they observed that the diamond indenter is rough on a nanometer scale. The average radius of the asperities on the indenter was 150 nm and the standard deviation of the asperity height was 20 nm. The hardness of the silicon was reported to be 6 GPa and the hardness of the carbon nitride was 20 GPa. For the calculation presented here, the elasticity modulus of carbon nitride was assumed to be 200 GPa [9] and the elasticity modulus of Silicon was 127 GPa [6]. The value for the Poisson's ratio was assumed to be 0.23. Following the same procedure as described in section 5.4.1 to determine the shear stress, the coefficient of friction as a function of layer thickness of the experiment performed by Wang & Kato is shown in figure 5.9.

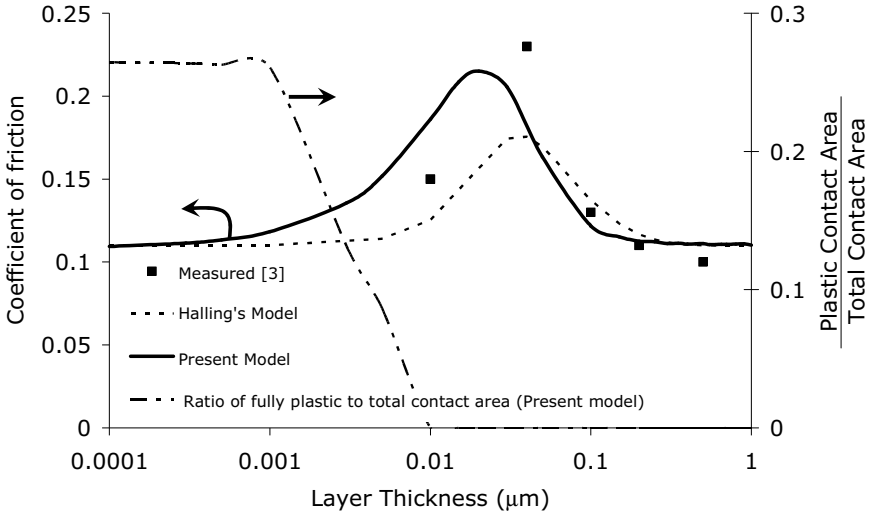

Figure 5.9: Coefficient of friction as a function of layer thickness of a *carbon nitride* layer on a silicon substrate sliding against diamond.

5.6. Discussion

The calculated results of the coefficient of friction as a function of the layer thickness for the work of Sherbiney [3] and Wang & Kato [8] are in good agreement with the measurement results they reported. These results confirmed that the present model is applicable for the prediction of friction of layered systems in which a hard rough surface slides against a soft layer on a hard substrate or a hard layer on a soft substrate.

The coefficients of friction as a function of the layer thickness predicted by using the model of Halling are also plotted in figures 5.7, 5.8 and 5.9. Those calculations were carried out by using the value for the constant c (see equation 5.2) equal to 10 for the cases of lead and indium layer on steel and c equal to 125 [10] for the case of a carbon nitride layer on silicon. According to Halling, this constant should be experimentally determined. The value of the constant c affects the calculation of the coefficient of friction considerably (see figure 5.10). In fact, as shown by Bhattacharaya & Nix [6], the effective hardness of a layered surface varies as a function of the ratio between the indentation depth and the thickness of the layer which is used in the model described in chapter 4. By using the present model, one does not need to determine the value of c since the calculation of the effective elasticity and hardness (see equations (4.34) and (4.35)) does not contain any empirical constants but only the indentation depth and mechanical properties of the layer and the substrate. The different way of using the effective elasticity and hardness of the layered surface causes the

difference in the value of the coefficient of friction obtained by the present model and Halling's model.

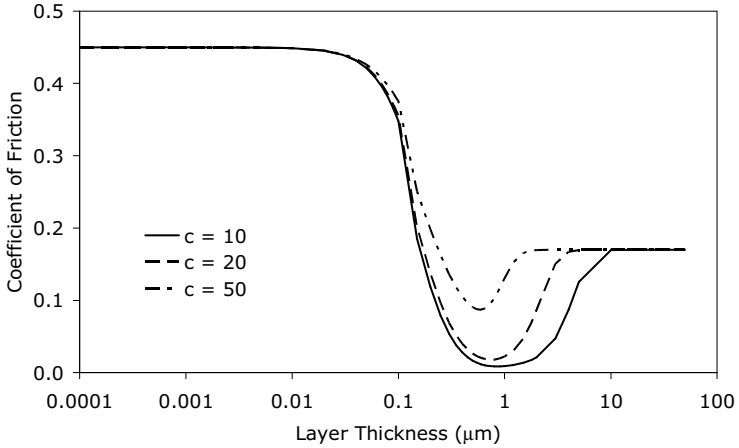

Figure 5.10: Coefficient of friction as a function of layer thickness of a lead layer on hardened steel sliding against hardened steel, calculated using the model of Halling with various values of c, see equation 5.2.

In addition, for the case of asperities penetrating through the layer, Halling assumed that the entire load is carried by the substrate, thus the ratio between the contact area with the layer compared to the total contact area for a very thin layer predicted with Halling's model is larger than the value predicted by the present model. Therefore, the model of Halling predicts a higher friction for $t < 0.1$ μm in the case of a soft layer on a hard substrate and a lower value in the case of a hard layer on a soft substrate. For a very thick layer, where a fully plastic contact situation occurs, the current model and the model of Halling show a slight difference in predicting the coefficient of friction.

The plasticity index ($\psi = (E^*/H)(\sigma/\beta)^{0.5}$) as defined by Greenwood & Williamson [12] for the case of a lead layer or an indium layer is equal to 1.35 for a very thin layer and 76 for a very thick layer. Halling's model uses the definition of Greenwood & Williamson [11] who stated that if the value for the plasticity index is more than unity the contact situation is fully plastic. In this model, the value of the plasticity index equal to unity is defined as the onset of yielding which means the start of an elastic-plastic contact situation (see equation (4.6)). Therefore, for the case of the lead layer, if the contact is assumed to be entirely plastic, the coefficient of friction calculated using the present model will be close to the coefficient of friction calculated using Halling's model (see figure 5.11). The difference observed between Halling's model and our model is due to the use of the effective hardness and the effective elasticity. The difference in defining the start of the fully plastic contact situation may therefore result in a different value in calculating friction.

Further, for the case of a carbon nitride layer on a silicon substrate, in fact, Halling's model is not valid for a layer thickness greater than 0.1 μm, in which all the contacts are purely elastic. The calculation of friction using Halling's model, see figure 5.9, was carried out by assuming that the contact is entirely plastic, which is not correct. This means that the model of Halling is only suitable for predicting the trend rather than predicting the coefficient of friction where local elastic contact occurs.

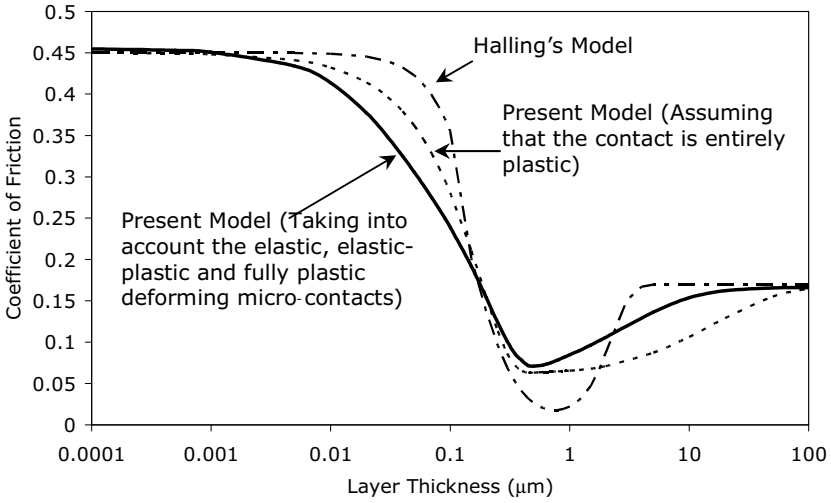

Figure 5.11: Coefficient of friction as a function of layer thickness of a lead layer on hardened steel sliding against hardened steel, calculated using the model of Halling, the present model assuming that the contact is entirely plastic and the present model taking into account the contribution of elastic and elastic-plastic deforming micro-contacts.

Overall results show that the present model gives a better prediction of the friction in comparison with the experimental results. Halling's model and the present model gave the same trend in predicting the friction as a function of the layer thickness for the plastic contact situation. For a thin layer, Halling's model gave a higher friction than the present model for the case of a soft layer on a hard substrate and a smaller friction for the case of a hard layer on a hard substrate. Further, it should be noted that the values of the interfacial shear strength of each asperity for the elastic, elastic-plastic and fully plastic contact situations are assumed to be equal and were estimated from experimental observations.

According to Blancoe & William [12], the shear strength of boundary films varies as a function of contact pressure. Therefore, the assumption of equal shear strengths for elastic, elastic-plastic and fully plastic contact

situations may result in differences in the friction calculations. This might be also the reason why the coefficient of friction obtained from the calculation deviates from the values obtained from the experiment. Indeed, interfacial shear strength is a difficult parameter to obtain.

5.5. Concluding remarks

A friction model based on a deterministic description of the macro-geometry was developed. The present model extends the capability of Halling's model and shows a better prediction of the coefficient of friction as a function of layer thickness. With this model, one can predict the coefficient of friction as a function of the layer thickness of a soft layer on a hard substrate or a hard layer on a soft substrate and estimates the optimum layer thickness in order to obtain the lowest coefficient of friction of a layered system.

This deterministic friction model will be used in the following chapter to calculate the friction of the tribosystem of zirconia doped with CuO sliding against alumina.

References

[1] F.P. Bowden and D. Tabor, Friction and lubrication of solids, Part I, Clarendon Press, 1950.

[2] J. Halling, The rule of surface films in the frictional behavior of lubricated and dry contacts - A unifying influence in tribological theory, ASLE Transaction 24, 4 (1983) 528-536.

[3] M.G.D. El-Sherbiney, Tribological Properties of Ion-plated Thin-metallic Films, PhD Thesis, University of Salford, England, 1975.

[4] Y. Zhao, D.M. Maietta and L. Chang, An asperity microcontact model incorporating the transition from elastic deformation to fully plastic flow, ASME Journal of Tribology, 122 (2000) 86-93.

[5] K. Komvopoulos, N. Saka and N.P. Suh, The mechanism of friction in boundary lubrication, Journal of Tribology 107 (1985) 452-462.

[6] A.K. Bhattacharaya and W.D. Nix, Analysis of elastic and plastic deformation associated with indentation testing of thin films on substrates, International Journal of Solids and Structures, 24 (1988) 1287-1298.

[7] K.L. Johnson, Contact mechanics, Cambridge University Press, Cambridge, 1985.

[8] D.F. Wang and K. Kato, Effect of coating thickness on friction for carbon nitride films in repeated sliding against a spherical diamond with nano-scale asperities, Wear 252 (2002) 210-219.

[9] G.J. Kovacs, G. Safran, O. Geszti, T. Ujvari, I. Berboti and G. Radnoczi, Stucture and mechanical properties of carbon-nickel and CN_x - nickel nanocomposite films, Surface and Coatings Technology, 180-181 (2004) 331-334.

[10] J. Halling and R.D. Arnell, Ceramic coatings in the war of wear, Wear 100 (1984) 367-380.

[11] J.A. Greenwood and J.B.P. Williamson, Contact of nominally flat sufaces, Proceeding of Royal Society London, Series A, 295(1966) 300-319.

[12] K.A. Blencoe and J.A. Williams, Friction of sliding surfaces carrying boundary films, Wear 203-204 (1997) 722-729.

Chapter 6
Prediction of the Coefficient of Friction of Zirconia Doped with Copper Oxide (CuO) Sliding Against Alumina

6.1. Introduction

In chapter 5, a deterministic friction model was developed based on the contact model described in chapter 4. This chapter will discuss the prediction of the coefficient of friction of zirconia doped with copper oxide (CuO) sliding against alumina by using the deterministic friction model described in chapter 5.

This chapter starts with the investigation results that can be used to explain the possible low friction mechanism occurring in the tribosystem of zirconia doped with CuO sliding against alumina. Based on the observations and the experimental results, the coefficient of friction as a function of layer thickness of this tribosystem will be presented.

6.2. Low friction mechanism

In chapter 3, it was shown that the addition of CuO in zirconia is beneficial in reducing the coefficient of friction when sliding against alumina (see figure 3.4). Nano-indentation tests performed on the wear track where low friction was observed (see figure 3.14a) suggest that a layer which has a lower hardness ($H_l \approx 6$ GPa) than that of the bulk ($H_s \approx 14$ GPa) is present on the wear track. These results are basically in accordance with the low friction mechanism proposed by Bowden & Tabor [1] that a soft thin layer on top of a hard substrate can reduce friction.

By using the adhesion theory of Bowden & Tabor [1] and by inserting the hardness data obtained from the nano-indentation tests ($H_l \approx 6$ GPa, $H_s \approx 14$ GPa), the macroscopic coefficient of friction of the tribosystem of zirconia doped with CuO sliding against alumina is:

$$f = \frac{\tau}{H} = \frac{\frac{1}{3\sqrt{3}} H_l}{H_s} = \frac{\frac{1}{3\sqrt{3}} 6}{14} \cong 0.082 \qquad (6.1)$$

The aforementioned value of the coefficient of friction is lower than the measured coefficient of friction ($f \approx 0.15$-0.25) because the calculation did not include the ploughing effect. Nevertheless, the calculated value of the macroscopic coefficient of friction shown above confirms the evidence of low friction in the tribosystem of zirconia doped with CuO sliding agaist alumina.

An EDS element mapping on a scanning TEM image of zirconia doped with CuO sintered at 1500°C was performed by Ran et al. [2]. They showed that copper-rich grains are formed in between the zirconia grains after sintering. The copper-rich grains are also present at or near the surface. Therefore, it is possible that the copper-rich grains, which are soft, somehow come into the contact region by a squeezing out mechanism due to high local contact pressure. The squeezed out copper-rich grains are smeared further as the system slides and a (patchy) layer is formed resulting in a soft thin interfacial layer on top of a hard substrate which will principally reduce friction. This mechanism is schematically shown in figure 6.1.

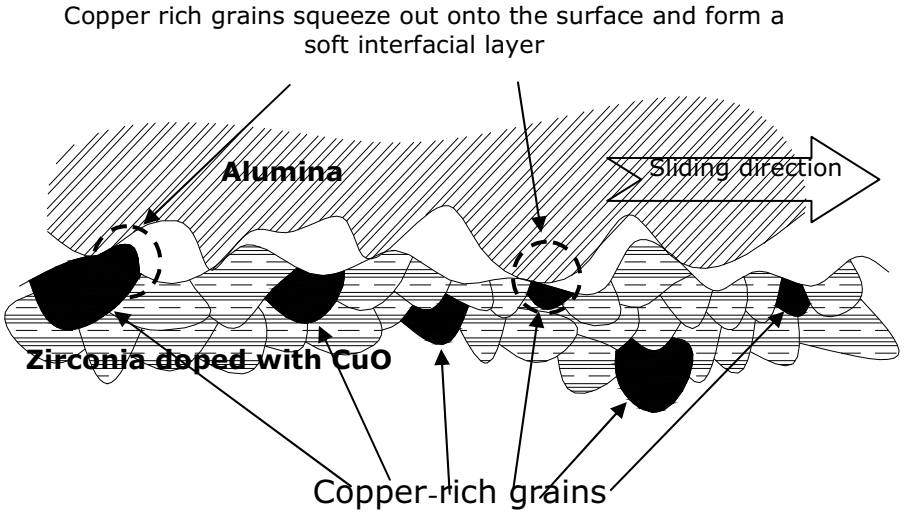

Figure 6.1: Schematic representation of the squeezing out mechanism of copper-rich grains.

As shown in figure 3.12, the layer is not uniform but patchy. This is due to the fact that the copper-rich grains are dispersed in the bulk but only some of them are present at or near the surface. Therefore, even if all of the copper-rich grains at or near the surface are squeezed out, the wear track is not covered completely by the smeared grains. As the smeared layer is attached to the surface, this layer will be loaded repeatedly as it slides against the counter-body.

Surface profile measurement across the wear track where low friction was observed shows that the wear track is relatively smooth and it is relatively higher than the surrounding surface (see figure 3.13). The exact thickness of the layer is not easy to estimate but as shown in figure 6.2, a surface profile taken across the wear track suggests that the layer thickness might be around 100 to 200 nm.

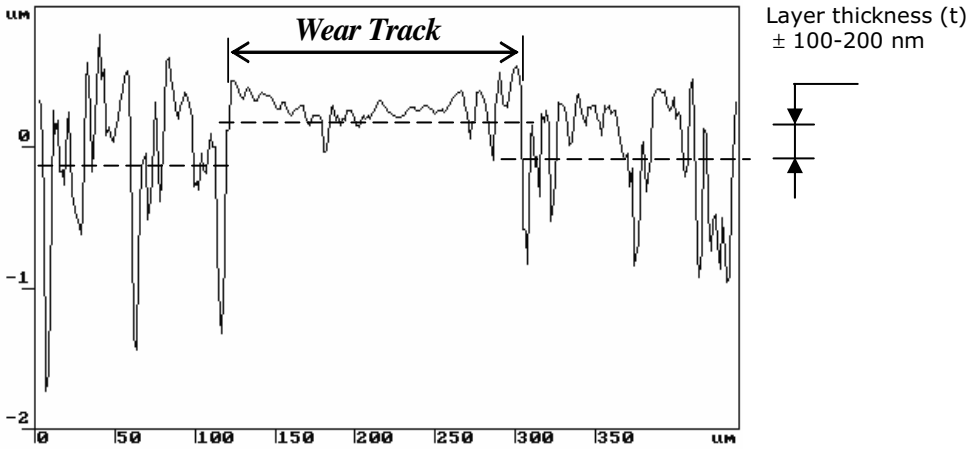

Figure 6.2: Estimation of the layer thickness from the surface profile across the wear track where low friction was observed.

Since the tribosystem of zirconia doped with CuO sliding against alumina is in fact a soft thin layer on top of a hard substrate sliding against a hard counter-body, the friction model described in chapter 5 can be used to predict the friction of this tribosystem, as outlined in the following section.

6.3 Coefficient of friction as a function of layer thickness of zirconia doped with CuO sliding against alumina

To predict the coefficient of friction of zirconia doped with CuO, two asymptotes of the coefficient of friction are required (see section 5.5). At first, the coefficient of friction of the tribosystem without a layer (pure zirconia) and secondly, the coefficient of friction of the tribosystem with a very thick layer (zirconia covered with very thick copper-rich layer).

The first asymptote is obtained from the friction measurement of pure zirconia sliding against alumina. To obtain the second asymptote, first CuO powder is melted on top of pure zirconia. Some of the melted CuO powder will be diffused into the pure zirconia substrate forming a strong bond between the copper-rich layer and the pure zirconia substrate. The thick layer is then

polished to a proper surface roughness ($R_a \approx 0.1$ μm) prior to testing. Micro-indentation was performed on this specimen to check whether the mechanical properties of the copper-rich layer produced by melting had the same mechanical properties compared to that of the layer observed in the wear track of zirconia doped with CuO. The indentation load as a function of indentation depth of the indentation measurement is shown in figure 6.3. The theory of Pharr [3] was used to determine the elasticity modulus and the hardness of the material from the load displacement curve (see appendix B). The hardness and the elasticity modulus of the copper-rich layer on top of pure zirconia were 5.9 GPa and 130 GPa respectively. These values are almost the same as the mechanical properties of the copper-rich layer in the wear track where low friction was observed when zirconia doped with CuO slid against alumina (see figure 3.14). Based on these results, it is assumed that the second asymptote of the coefficient of friction (for a very thick layer) is the coefficient of friction of the copper-rich layer produced by a melting process on top of pure zirconia sliding against alumina.

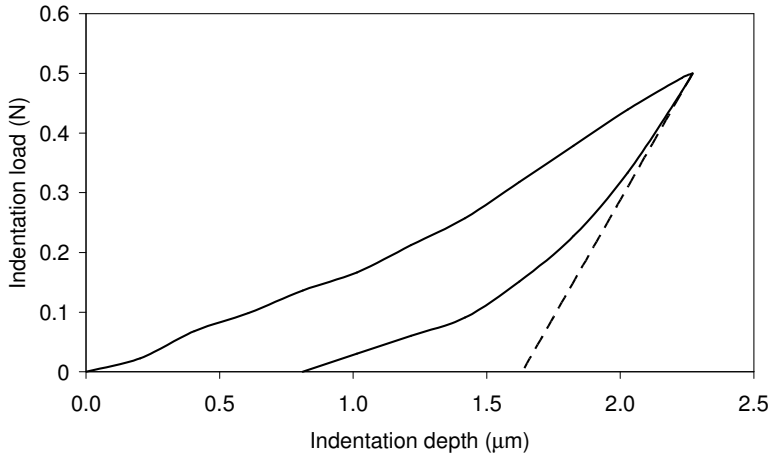

Figure 6.3: Indentation load as a function of indentation depth of melted CuO on top of pure zirconia.

The three samples, pure zirconia, zirconia covered with a very thick copper-rich layer and zirconia doped with CuO, were tested against an alumina ball (10 mm diameter) using a pin-on-disc tribometer (see figure 2.6). The normal applied normal load was 5N and the sliding velocity 0.1 m/s.

The coefficient of friction of melted CuO on top of pure zirconia sliding against alumina is plotted together with the coefficient of friction of pure zirconia and zirconia doped with CuO sliding against alumina, as shown in figure 6.4. Figure 6.4 shows that the steady state coefficient of friction of pure zirconia sliding against alumina (first asymptote) is about 0.65 and the steady state coefficient of friction of a very thick copper-rich layer sliding against alumina

(second asymptote) is about 0.35, while the coefficient of friction of zirconia doped with CuO sliding against alumina is about 0.25.

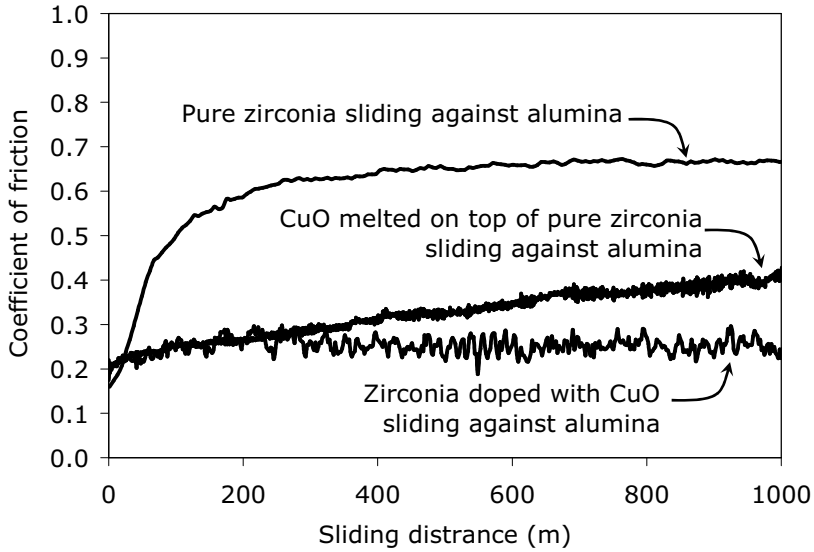

Figure 6.4: The coefficient of friction of melted CuO on top of pure zirconia, pure zirconia and zirconia doped with CuO sliding against alumina (normal load 5N, sliding velocity 0.1m/s).

The asperity heights and radii distribution of the alumina ball which is in contact with the zirconia doped with CuO are shown in figure 6.5. The macroscopic contact area can be calculated based on the contact of a ball in contact with a flat layered surface as described in chapter 4. As the contact area can be determined, then the asperities in contact with zirconia doped with CuO and the coefficient of friction as a function of layer thickness for the case of a uniform copper-rich layer on top of zirconia can also be determined using the model described in chapter 5.

However, as discussed before, the layer is patchy and not uniform. So the contact area is not wholly covered by the layer. Therefore, in order to model this condition, a parameter γ that determines the percentage of the wear track that is covered with the layer is introduced. By using this parameter, one can determine the asperities that make contact with the layer and the rest of the asperities that make contact with the substrate. For the case of zirconia covered with a copper-rich layer, the coefficient of friction as a function of layer thickness for different values of γ can be calculated by analyzing the contact and the resistance to motion experienced by each asperity (as described in chapter 5). The results are presented in figure 6.6.

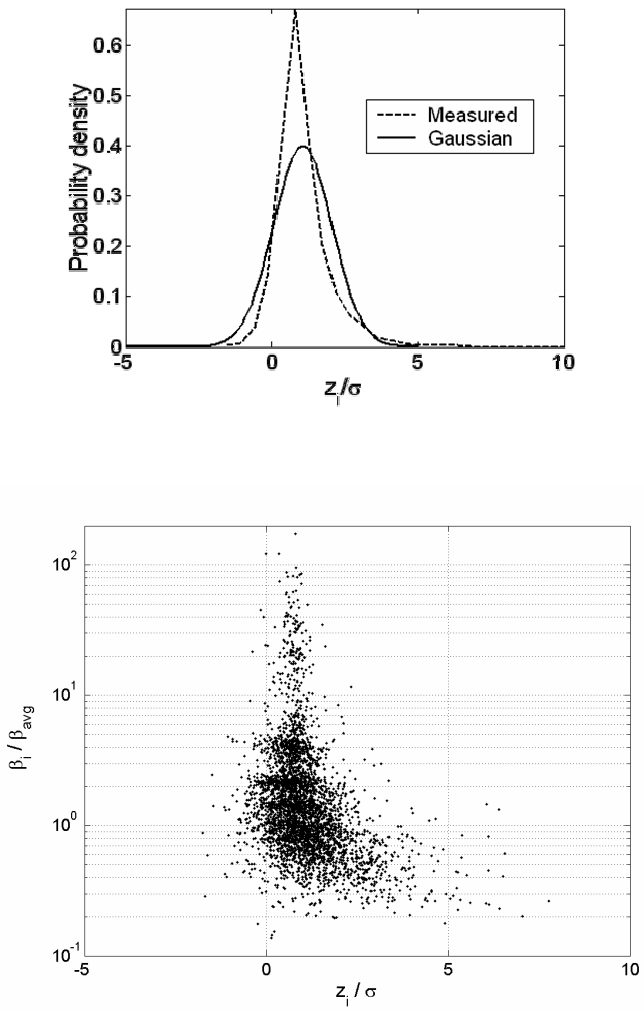

Figure 6.5: The asperity height distribution and radii distribution of the alumina ball which is in contact with the zirconia doped with CuO disc, i.e. radius ratio (β_i/β_{avg}) as a function of normalized height (z_i/σ); β_{avg} = 46 μm, σ = 0.1 μm.

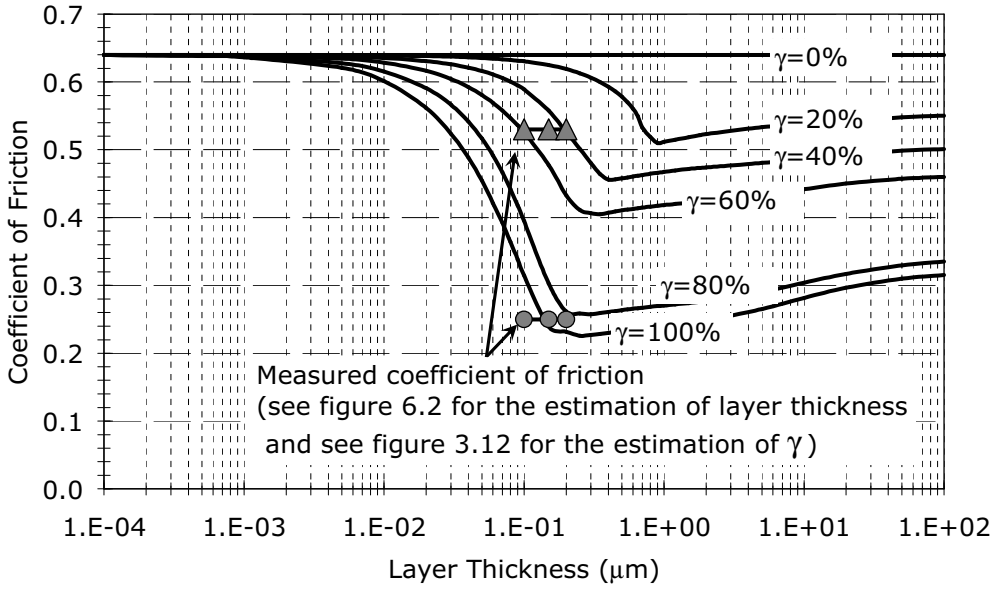

Figure 6.6: The coefficient of friction as a function of the layer thickness for different values of γ for the case of zirconia covered with a copper rich layer.

6.4 Discussion

As shown in figure 3.12, the coefficient of friction measured on the zirconia doped with CuO sliding against alumina varied between 0.2-0.25 for the first 4 km of sliding and 0.55 after 5.5 km of sliding. The values of γ estimated from figures 3.12b and 3.12c are about 80% and 50% respectively. As can be seen in figure 6.6, for the estimated value of γ, the coefficient of friction at the estimated layer thickness can be predicted rather well with the model outlined in chapter 5. Figure 6.6 also clearly shows that when the part of the contact area covered by the patchy layer is less ($\gamma\downarrow$) the coefficient of friction increases ($f\uparrow$) due to the fact that more asperities are in contact with the substrate.

The local maximum temperature rise at each asperity contact due to frictional heating can also be calculated from equation (2.25). For the asperity distribution shown in figure 6.5, the maximum temperature rise at each asperity contact for the case of pure zirconia sliding against alumina with a sliding velocity of 0.1 m/s is presented in figure 6.7. As shown in figure 6.7, the flash temperatures range from about 0°C to 25°C. This result reveals that the formation of the soft thin layer as proposed in figure 6.1 is dominated by a mechanical process and the effect of heat can be neglected.

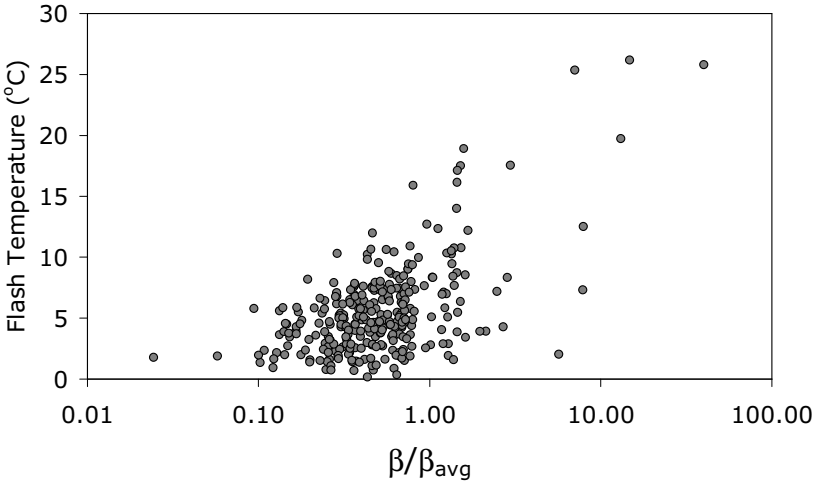

Figure 6.7: Temperature rise at each asperity contact due to frictional heating (the asperity distribution is shown in figure 6.5 is used).

The main difficulties in predicting the coefficient of friction of zirconia doped with CuO sliding against zirconia is that the layer thickness is not known beforehand. Therefore, a layer formation model should be developed in order to predict the coefficient of friction. The layer thickness and the value of γ are very strongly dependent on the number of copper-rich grains present near or at the surface. In addition, the applied normal load determines the formation and the removal of the layer as shown in figure 6.8.

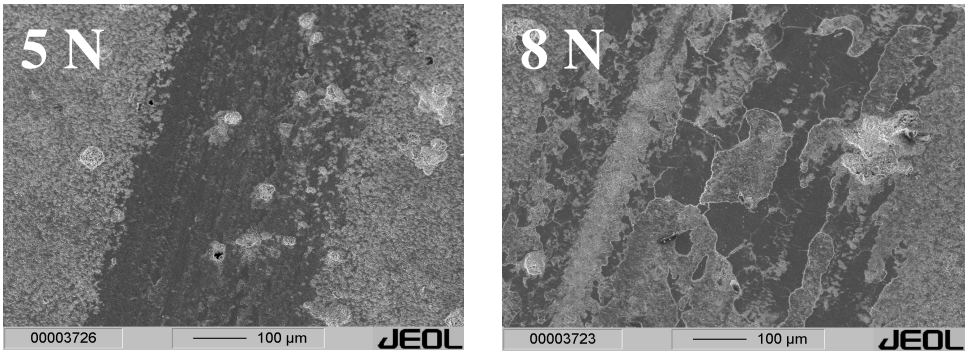

Figure 6.8: SEM images taken from the wear track of zirconia doped with CuO sliding against alumina at various normal loads and 0.1 m/s sliding velocity.

6.5 Concluding remarks

The sliding tests of zirconia doped with CuO sliding against alumina reveals that a soft thin patchy layer is present in the wear track. The deterministic friction model outlined in chapter 5 is able to predict the coefficient of friction of zirconia doped with CuO sliding against alumina. However, the thickness of the copper-rich layer cannot be estimated beforehand. Therefore, a layer formation model is needed in order to predict the coefficient of friction of zirconia doped with CuO.

References

[1] F.P. Bowden and D. Tabor, Friction and lubrication of solids, Part I, Clarendon Press, UK, 1950.
[2] S. Ran, A.J.A. Winnubst, K.W. Wiratha and D.H.A. Blank, Sintering behaviour of 0.8 mol%-CuO-doped 3Y-TZP ceramics, submitted for publication to Journal of American Ceramic Society, 2004.
[3] G.M. Pharr, Measurement of mechanical properties by ultra-low load indentation, Materials Science and Engineering A253 (1998) 151-159.

Chapter 7
Conclusions and Recommendations

7.1. Conclusions

Chapter 1: Introduction

Based on the literature review, it was shown that ceramics are potential materials for use in many technological applications. However, dry sliding ceramic systems exhibit a high coefficient of friction ($f \approx 0.4 - 0.85$) and in many cases severe wear is observed which limits their application.

Chapter 2: The transition of mild to severe wear of ceramics

A wear transition model has been developed which can predict whether a dry sliding concentrated ceramic system will experience mild or severe wear. The experimental investigation showed that the model can predict quite accurately the transition between the mild and the severe wear regimes. From this model, it became clear that besides the energy losses (chapter 1), the coefficient of friction has a significant influence in determining the wear type of ceramics. Therefore, low friction ceramic systems are required to extend operating conditions such as normal load (P) and velocity (V).

Chapter 3 Friction reduction by adding copper oxide into alumina and zirconia ceramics

It was found that small amounts of copper oxide doped in alumina ceramics can reduce the coefficient of friction from 0.65 down to 0.4-0.45 when sliding against alumina. The coefficient of friction does not vary too much with the variation of the amount of CuO. It was also observed that the coefficient of friction does not change much as a function of the normal load and the sliding velocity. Humidity does not have any significant influence on the friction of alumina doped with CuO

Significant reduction in the coefficient of friction can be achieved by adding CuO into zirconia. CuO doped in zirconia can reduce the coefficient of friction from a value of 0.7 down to 0.2 – 0.3, depending on the operational conditions, when sliding against alumina. Smooth patchy layers were formed in

the wear track, which are responsible in lowering the coefficient of friction. The patchy layers wear off due to repeated loading resulting in a high coefficient of friction after a length of time. Humidity has a significant influence on the friction of zirconia doped with CuO. The coefficient of friction is lower at higher humidity. However, humidity does not have any significant influence on the friction of pure zirconia.

Alumina and zirconia doped with CuO show high friction ($f \approx 0.7 - 1$) when tested at elevated temperature (100 – 500°C).

When sliding against steel, the addition of copper oxide into alumina and zirconia does not have any influence in reducing friction. This is due to the fact that a lot of metal is transferred onto the ceramic surface which creates in fact a metal-metal tribosystem.

Chapter 4 Deterministic contact model of a rough surface in contact with a flat layered surface

A deterministic contact of a rough surface against a flat layered surface has been developed. As for the case of a sphere pressed against a flat layered surface (single asperity model), the proposed model shows good agreement with the experimental and numerical results, one can extend the single asperity model to calculate the contact of a rough surface with a flat layered surface by analysing the contact of each individual asperity (deterministic model). This deterministic contact model allows the calculation of the contact behaviour of Gaussian as well as non-Gaussian surfaces and eliminates the assumption of an average asperity radius.

Chapter 5 Deterministic friction model of a rough surface sliding against a flat layered surface

A friction model based on the deterministic contact model described in chapter 4 has been developed to be able to predict the friction of layered surfaces in contact with a rough surface. The developed model is an extension to Halling's model and shows a better prediction of the coefficient of friction as a function of the layer thickness of layered surfaces. With this model, one can predict the coefficient of friction as a function of the layer thickness of a soft layer on a hard substrate, or a hard layer on a soft substrate, and estimates the optimum layer thickness in order to obtain the lowest coefficient of friction of a layered system.

Chapter 6 Prediction of the coefficient of friction of zirconia doped with copper oxide (CuO) sliding against alumina

The tribosystem of zirconia doped with CuO sliding against alumina is in fact a soft thin layer (copper-rich layer) on top of a hard substrate sliding against a rough hard counter-body. The patchy layer was formed by a squeezing out mechanism and the layer thickness was estimated to be about 100-200 nm. The coefficient of friction for the estimated layer thickness could be predicted rather

well with the model outlined in chapter 5 for the case of γ (the percentage of the coverage in the wear track) equal to 80 % and 50 % estimated from SEM images of the wear track where low friction was observed.

7.2. Recommendations

Experiments could be performed in order to validate the wear transition model for the case of concentrated sliding elliptical contacts.

More studies should be carried out to investigate the relation of the microstructure, which is determined by sintering time and sintering temperature, with friction and wear of zirconia doped with CuO sliding against alumina. Further, the layer formation mechanism must be investigated to give feedback for optimizing the material processing technique for zirconia doped with CuO that gives better tribological behaviour, i.e. low friction and high wear resistance. In addition, the mechanism of the transition from low friction to high friction in the tribosystem of zirconia doped with CuO sliding against alumina should be studied in more detail in order to maintain the low friction regime.

Appendix A
Summary of the Hertzian Contact Formulas for Circular-, Elliptical- and Line contacts

A.1 Circular contact

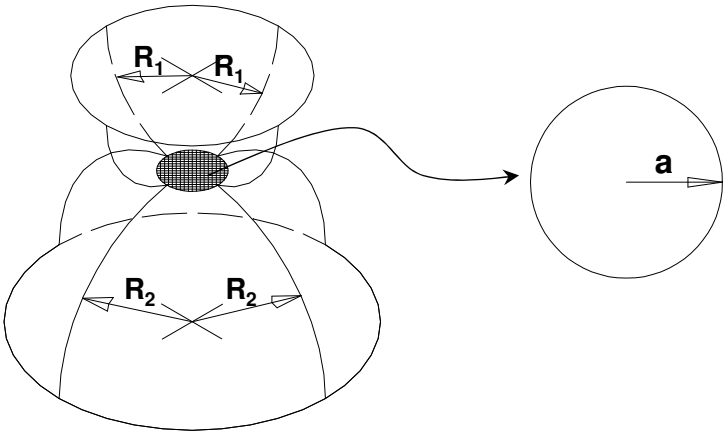

Figure A1: Contact of two spheres resulting in a circular contact.

Consider two spheres (with radius of R_1 and R_2) in contact under an applied load P. The contact area will be a circle. The radius of contact according to Hertz can be calculated as follows:

$$a = \left(\frac{3PR}{E^*} \right)^{\frac{1}{3}} \tag{A.1}$$

with:

$$\frac{2}{E^*} = \frac{1-\upsilon_1^2}{E_1} + \frac{1-\upsilon_2^2}{E_2} \tag{A.2}$$

and:

$$\frac{1}{R} = \frac{1}{R_{1x}} + \frac{1}{R_{1y}} + \frac{1}{R_{2x}} + \frac{1}{R_{2y}} = \frac{2}{R_1} + \frac{2}{R_2} \qquad \text{(A.3)}$$

in which E is the reduced elastic modulus and R is the reduced radius.
The elastic approach (δ) can be calculated as:

$$\delta = \left(\frac{9P^2}{8R(E^*)^2} \right)^{\frac{1}{3}} \qquad \text{(A.4)}$$

The mean pressure (P_m) and the maximum pressure (P_o) can be calculated as:

$$P_m = \frac{P}{\pi a^2} \quad , \quad P_o = \frac{3}{2} P_m \qquad \text{(A.5)}$$

A.2 Elliptical contact

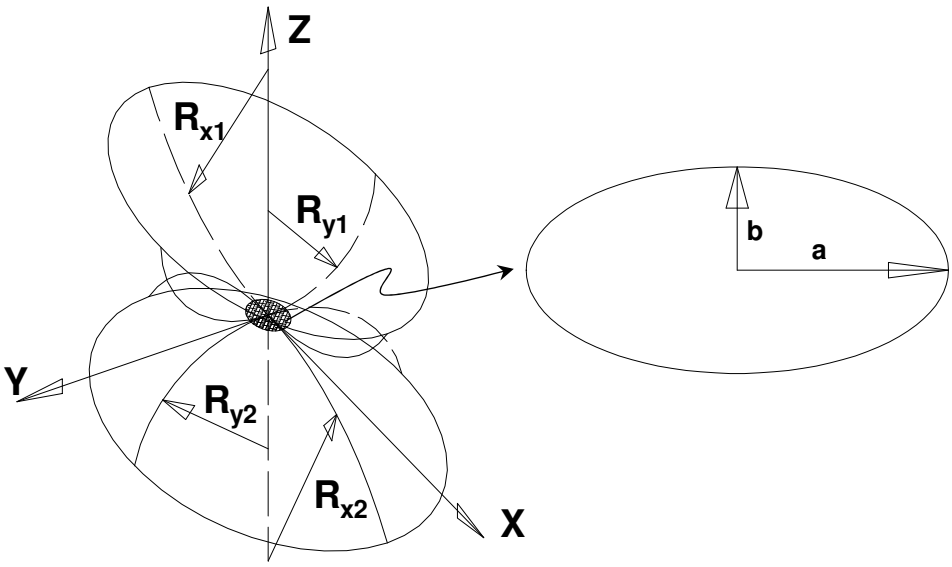

Figure A2: Contact of two ellipsoids resulting in an elliptical contact.

Suppose two bodies with different radii (see figure A2) are in contact under a normal load P; the contact area will be an ellipse. The major and minor axes of the contact area (a and b) and the normal approach (δ) can be calculated as follows:

$$a = \alpha\left(\frac{3PR}{E_*}\right)^{\frac{1}{3}} \tag{A.6}$$

$$b = \beta\left(\frac{3PR}{E_*}\right)^{\frac{1}{3}} \tag{A.7}$$

$$\delta = \gamma\left(\frac{9P^2}{8R(E^*)^2}\right)^{\frac{1}{3}} \tag{A.8}$$

where:

$$\frac{1}{R} = \frac{1}{R_{1x}} + \frac{1}{R_{1y}} + \frac{1}{R_{2x}} + \frac{1}{R_{2y}} \tag{A.9}$$

and:

$$\alpha \approx \kappa^{\frac{1}{3}}\left[\frac{2}{\pi}E(m)\right]^{\frac{1}{3}} \tag{A.10}$$

$$\beta \approx \kappa^{\frac{-2}{3}}\left[\frac{2}{\pi}E(m)\right]^{\frac{1}{3}} \tag{A.11}$$

$$\gamma \approx \kappa^{\frac{2}{3}}\left[\frac{2}{\pi}E(m)\right]^{\frac{-1}{3}}\left[\frac{2}{\pi}K(m)\right] \tag{A.12}$$

with:

$$E(m) \approx \frac{\pi}{2}(1-m)\left\{1 + \frac{2m}{\pi(1-m)} - \frac{1}{8}\ln(1-m)\right\} \tag{A.13}$$

$$K(m) \approx \frac{\pi}{2}(1-m)\left\{1+\frac{2m}{\pi(1-m)}\ln\left(\frac{4}{\sqrt{1-m}}\right)-\frac{3}{8}\ln(1-m)\right\} \quad \text{(A.14)}$$

$$\kappa \approx \left[1+\sqrt{\frac{\ln(16/\lambda)}{2\lambda}}-\sqrt{\ln(4)}+0.16\ \ln(\lambda)\right]^{-1} \quad \text{(A.15)}$$

$$m = 1-\kappa^2 \quad \text{(A.16)}$$

$$\lambda = \frac{R_x}{R_y} \quad \text{for } 0 < \lambda \le 1 \quad \text{(A.17)}$$

The mean pressure (P_m) and the maximum pressure (P_o) can be calculated as:

$$P_m = \frac{P}{\pi ab} \quad , \quad P_o = \frac{3}{2}P_m \quad \text{(A.5)}$$

A.3 Line contact

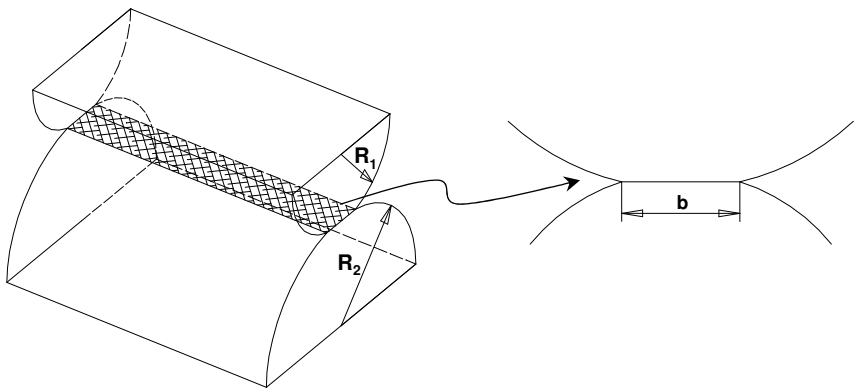

Figure A3: Contact of two cylinders resulting in a line contact.

Suppose two cylinders (with radii R_1 and R_2) are in contact under a normal load P, the contact width (b) can be calculated as:

$$b = 2\sqrt{\frac{2\frac{P}{B}R}{\pi E^*}} \qquad \text{(A.18)}$$

where B is the length of the cylinder and E* and R are the reduced elasticity modulus and reduced radius respectively. E* and R can be calculated using equation A2 and A3.
The mean and maximum contact pressure therefore can be calculated as :

$$P_m = \frac{P}{2Bb} \quad , \quad P_o = \frac{4}{\pi} P_m \qquad \text{(A.18)}$$

Appendix B
Calculation of Hardness and Elasticity Modulus from the Indentation Load-Displacement data

Figure B1 shows typical indentation load-displacement data. The indentation process starts by loading the indenter with an increased load at a constant rate to a certain value, held at the peak value for a preset amount of time and then decreased to zero at the same rate as that for loading (see figure B1).

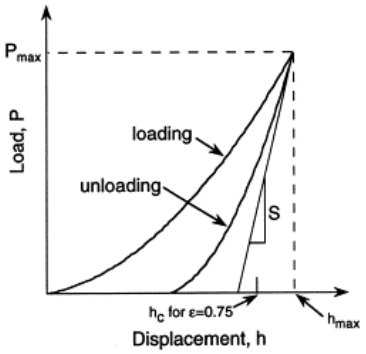

Figure B1: A typical indentation load-displacement curve.

The data analysis begins by fitting the unloading curve to the power law relation:

$$P(h) = B(h - h_f)^m \tag{B.1}$$

where B, h_f, and m are empirically determined fitting parameters, P is the indentation load and h is the displacement.
The unloading stiffness (S) can be calculated from the derivative of equation B1 at the maximum indentation depth (h_{max}):

$$S = \frac{dP}{dh}(h_{max}) = mB(h_{max} - h_f)^{m-1} \tag{B.2}$$

As the unloading stiffness (S) is obtained, then the reduced modulus (E^*) for the contact of the indenter and the specimen is defined by:

$$E^* = S\frac{\sqrt{\pi}}{2\sqrt{A}} \tag{B.3}$$

where A is the projected contact area (see figure (B2).
The contact area (A) is determined from a tip calibration function $A(h_c)$ as:

$$A(h_c) = \alpha h_c^2 \tag{B.4}$$

where α is a constant (α = 24.5 for Berkovich and Vickers indenter) and h_c is the contact depth (see figure B2) which can calculated from the load-displacement data as:

$$h_c = h_{mx} - \varepsilon\frac{P_{max}}{S} \tag{B.5}$$

in which ε is a constant (ε = 0.72 for the conical indenter, ε = 0.75 for the Berkovich indenter and ε = 1 for the flat punch).

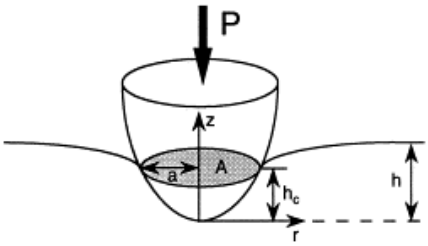

Figure B2: The physical processes involved in indentation.

As the reduced modulus (E^*) of two bodies in contact is known, the elasticity modulus and the Poisson's ratio of the indenter is known (for an indenter, E_1 = 1140 GPa and v_1 = 0.07), the elasticity modulus of the measured specimen is then calculated as:

$$E_2 = \frac{E_1 E^*(1-\nu_2^2)}{E_1 - E^*(1-\nu_1^2)} \tag{B.6}$$

The hardness is defined by the ratio of the maximum load to the projected contact area:

$$H = \frac{P_{max}}{A} \tag{B.7}$$

Appendix C
Comparison Between the Model Presented in Chapter 4 with Data Available in the Literature

C.1 T.E.S. El-Shafei, R.D. Arnell and J. Halling, ASLE Transaction 26 (1983) 481-486.

Table C.1: Material properties used by El-Shafei et al.

	Properties		
	Elasticity Modulus (GPa)	Poisson Ratio [-]	Hardness (GPa)
Indenter (Steel) Radius: 3.175 & 7.935 mm	210	0.3	7.6
Substrate (Steel)	210	0.3	7.6
Layer (Lead) Thickness : 0, 1.5, 3, 6,9, 12 μm	18	0.35	0.17

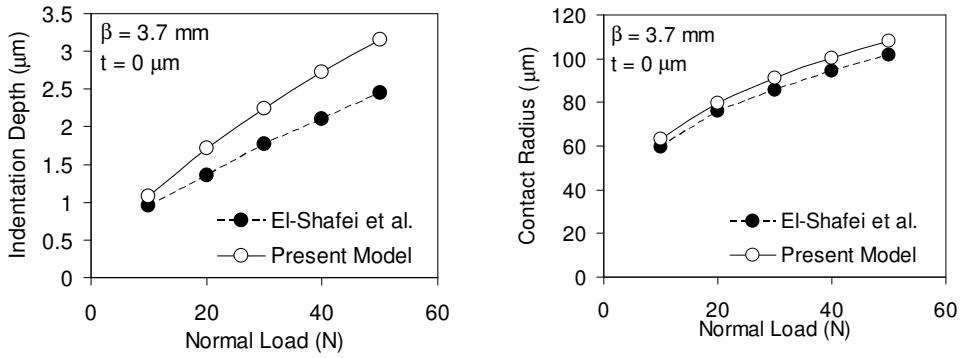

Figure C.1 Comparison between the experimental results published by El-Shafei et al. (dashed line) and the calculated results using the present model (solid line).

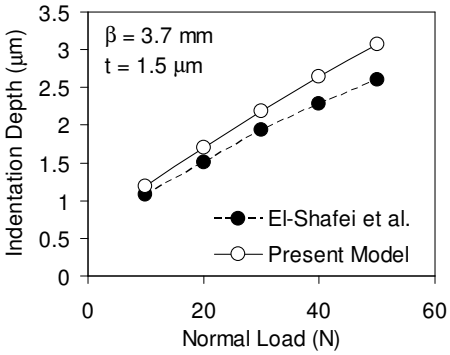

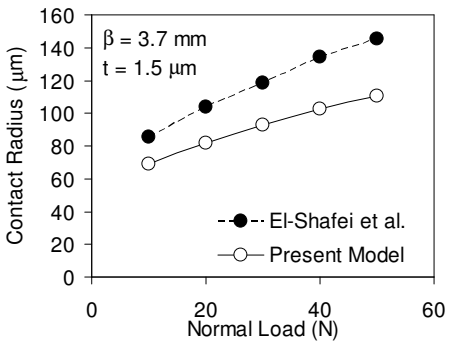

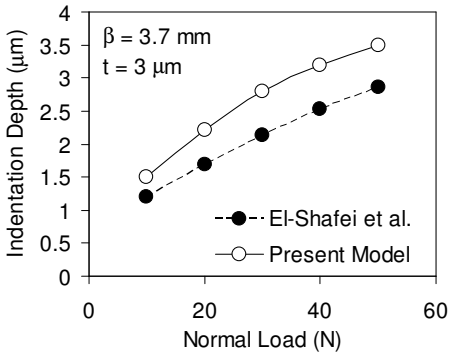

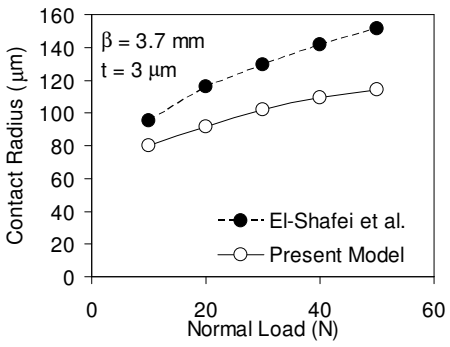

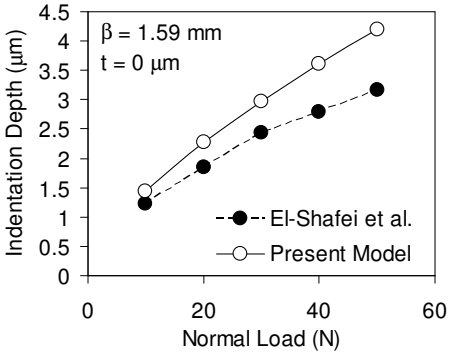

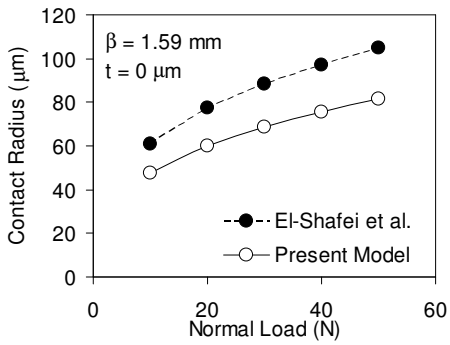

Figure C.1 Continued

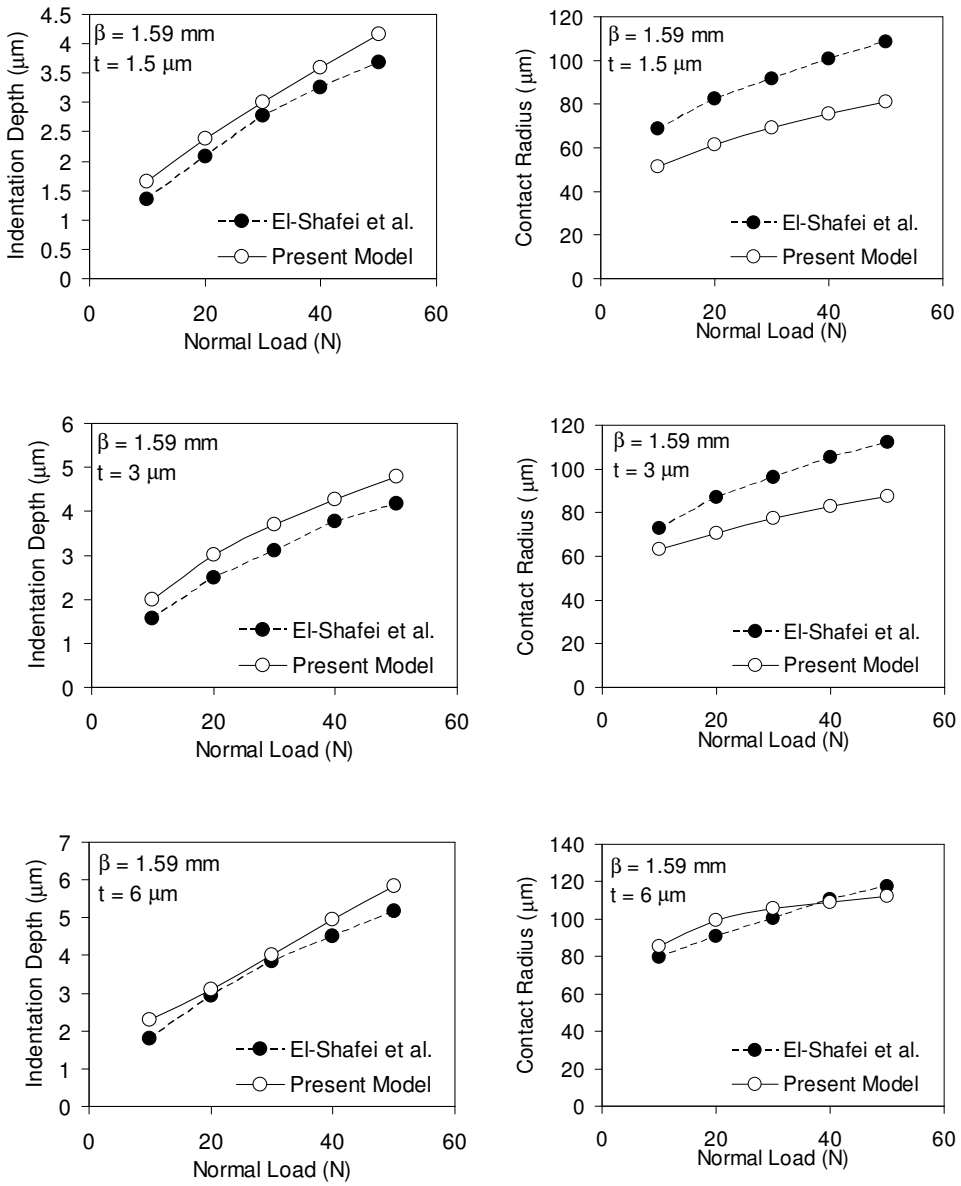

Figure C.1 Continued

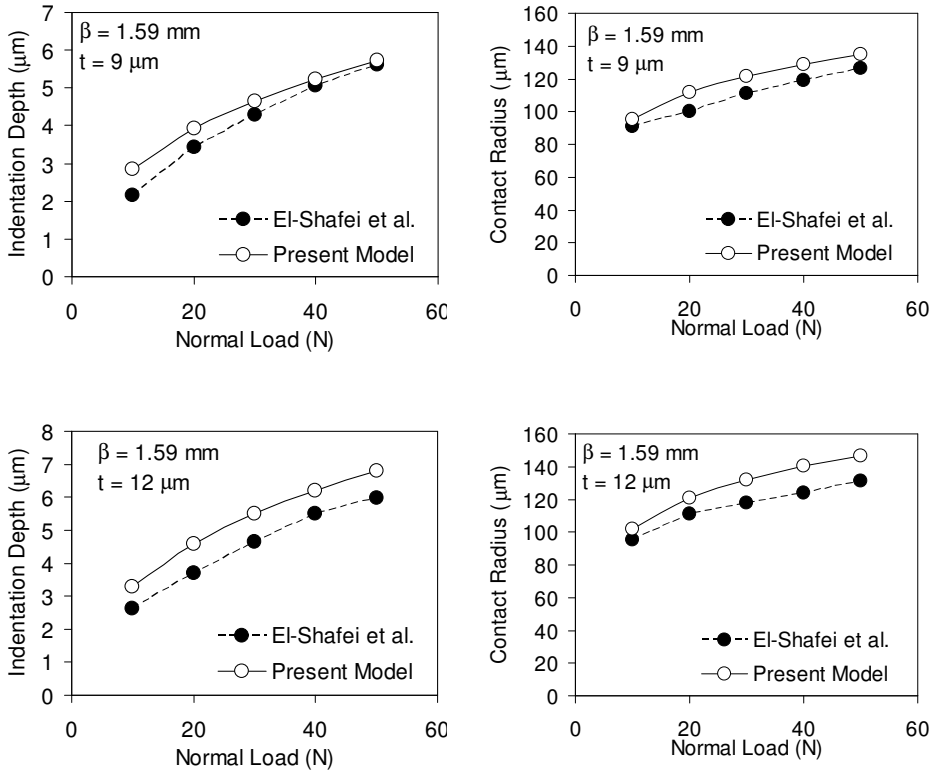

Figure C.1 Continued

C.2 M.G.D. El-Sherbiney, PhD Thesis, University of Salford, UK, 1975.

Table C.2: Material properties used by El-Sherbiney

	Properties		
	Elasticity Modulus (GPa)	Poisson Ratio [-]	Hardness (GPa)
Indenter (Steel) Radius: 6.35, 12.75 mm	210	0.3	7.6
Substrate (Mild Steel)	140	0.3	1.86
Layer (Lead) Thickness : 1.2, 15 μm	18	0.35	0.17

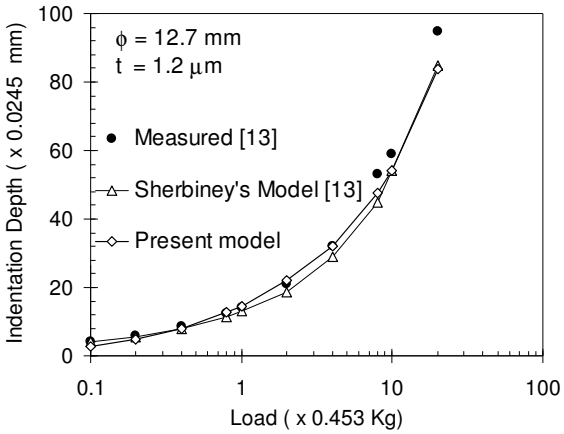

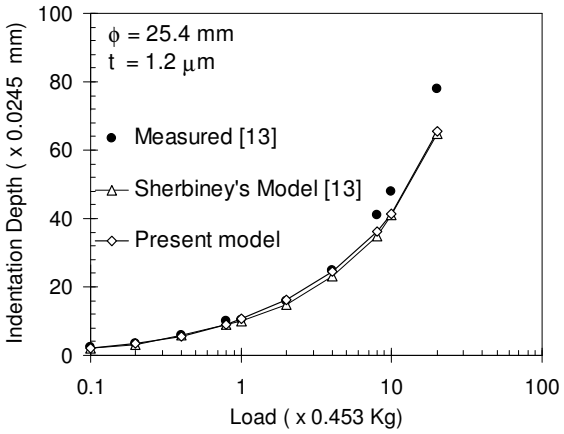

Figure C.2: The comparison between the experimental data obtained by El-Sherbiney, the model of El-Sherbiney and the calculated results using the present model (units along the axis are according to Sherbiney's thesis).

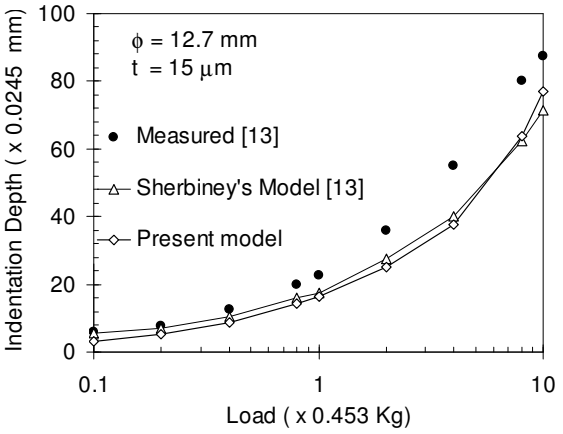

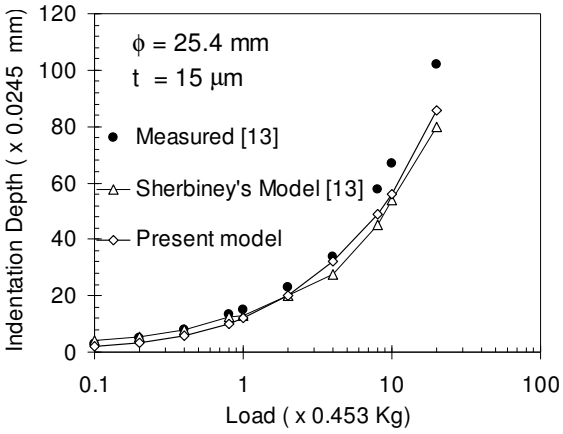

Figure C.2: Continued

C.3 A.G. Tangena, PhD Thesis, University of Eindhoven, The Netherlands, 1987.

Table C.2: Material properties used by El-Sherbiney

	Properties		
	Elasticity Modulus (GPa)	Poisson Ratio [-]	Hardness (GPa)
Indenter (Rigid) Radius: 2.5, 3.175, 4, 5, 12.5 mm,	1000	0.07	-
Substrate (Mild Steel)	210	0.3	1.2
Substrate (Copper)	125	0.32	0.3
Layer (Lead) Thickness : 2, 4, 6 μm	14	0.45	0.04
Layer (Silver) Thickness : 2, 4, 6 μm	71	0.38	0.15
Layer (Gold) Thickness: 3 μm	79	0.42	0.09

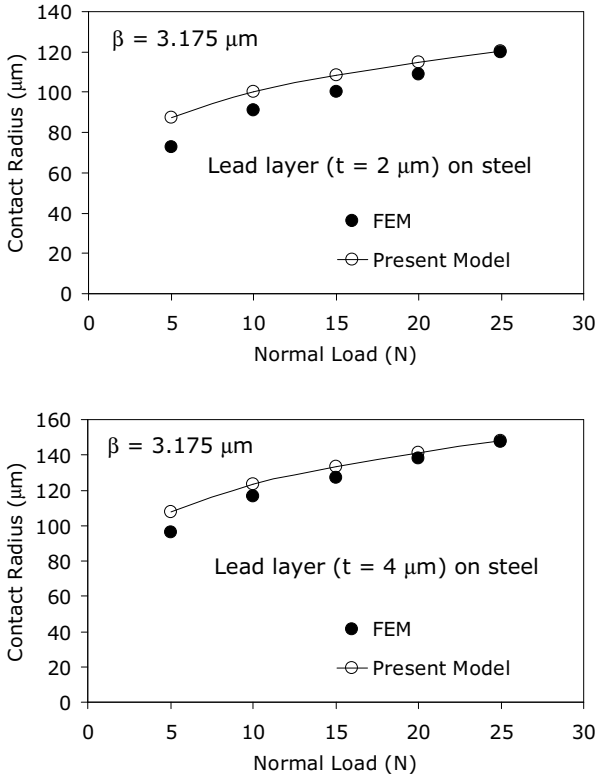

Figure C.3: Comparison between the finite element simulations obtained by Tangena and the calculated results using the present model.

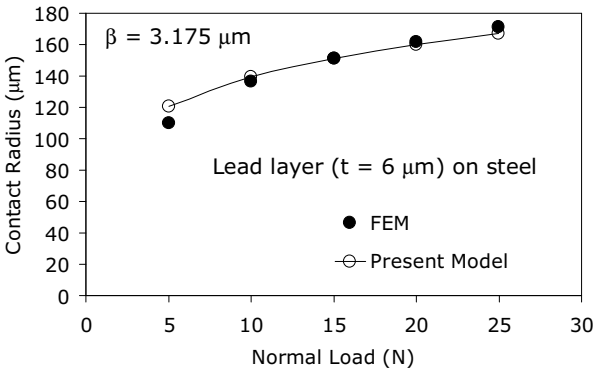

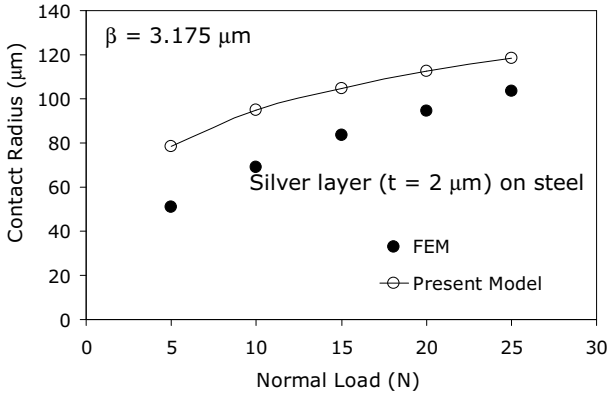

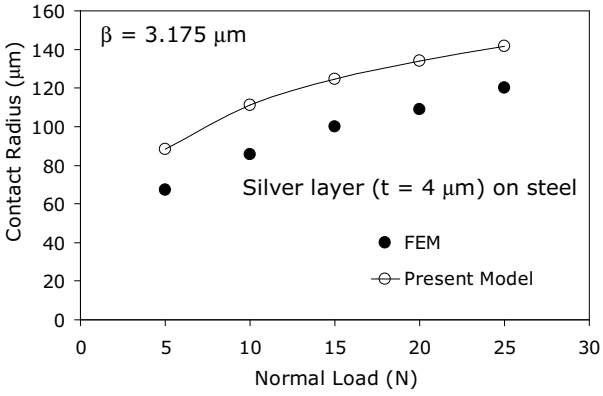

Figure C.3: Continued

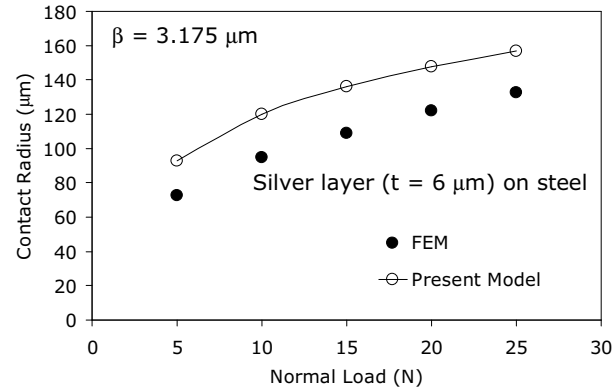

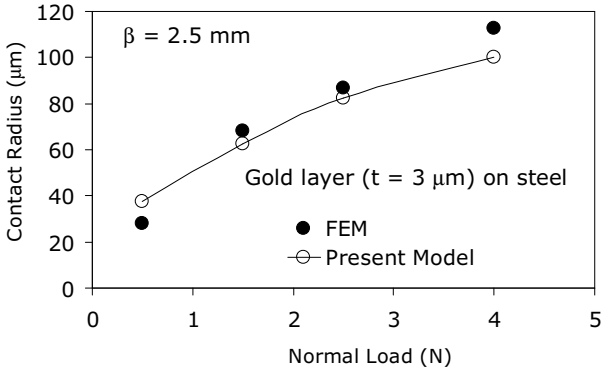

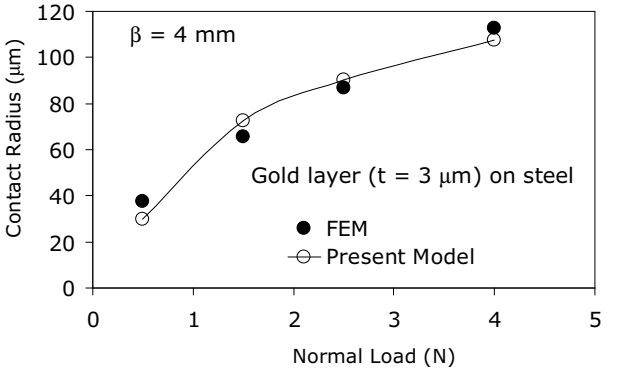

Figure C.3: Continued

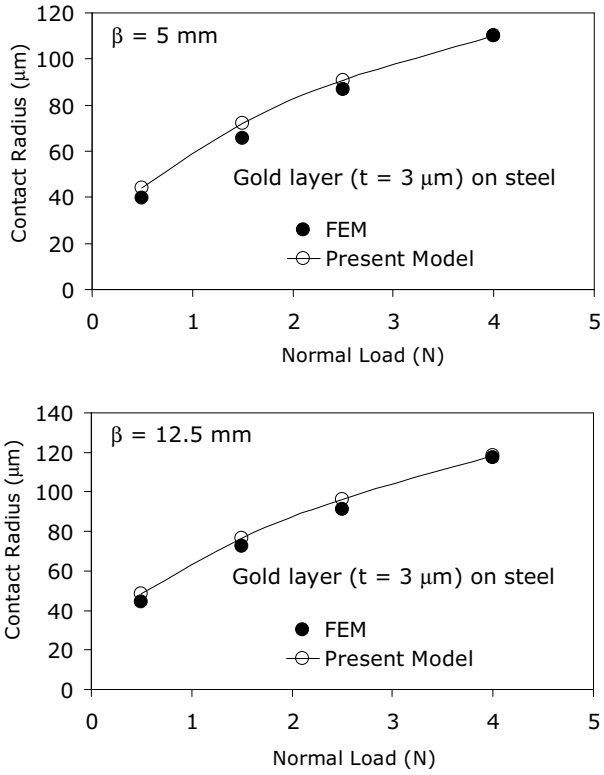

Figure C.3: Continued

C.4 K.C. Tang and R.D. Arnell, Thin Solid Films, 355-356 (1999) 263-269.

Table C.4: Material properties used by Tang & Arnell

	Properties		
	Elasticity Modulus (GPa)	Poisson Ratio [-]	Hardness (GPa)
Indenter (Diamond) Radius: 100 μm	1141	0.07	-
Substrate (Steel)	200	0.3	7.5
Layer (DLC) Thickness : 1, 2, 5, 10 μm	400	0.3	15, 22.5, 30

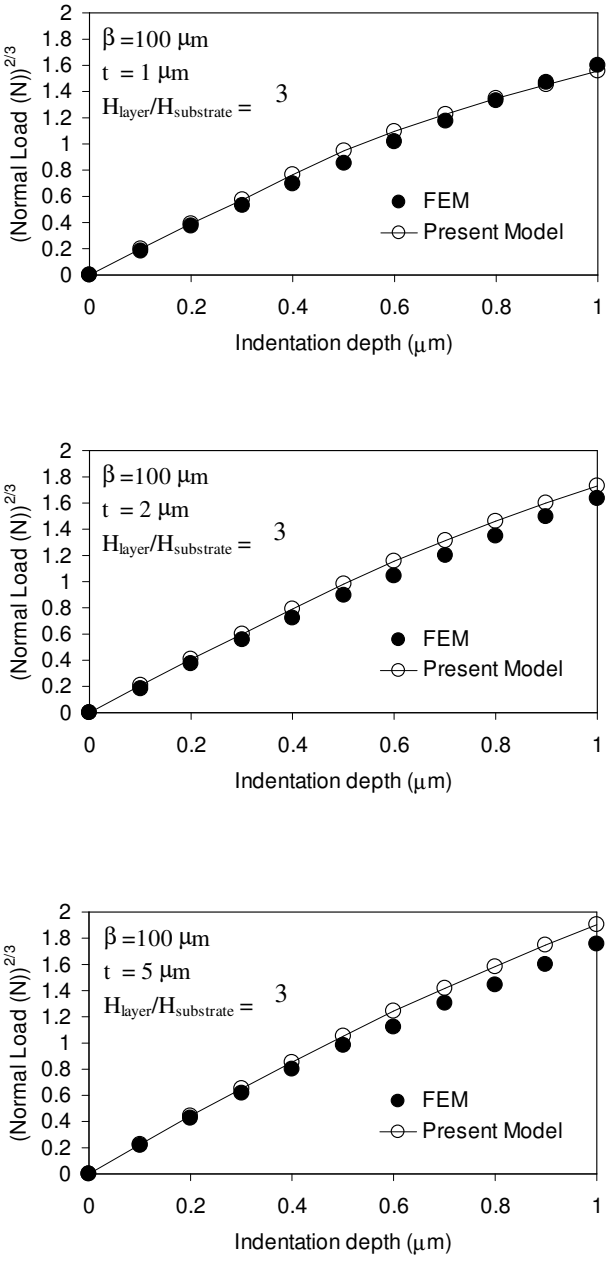

Figure C.4: Comparison between the FEM simulations carried out by Tang & Arnell and the present model.

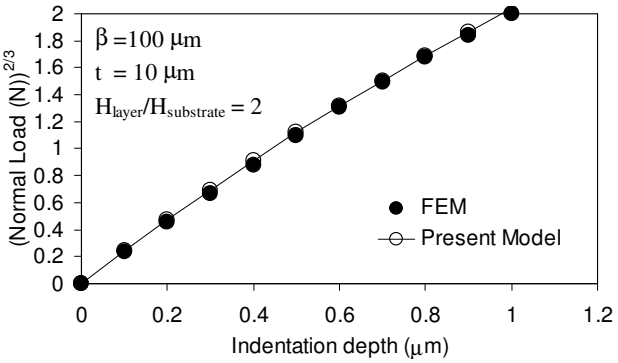

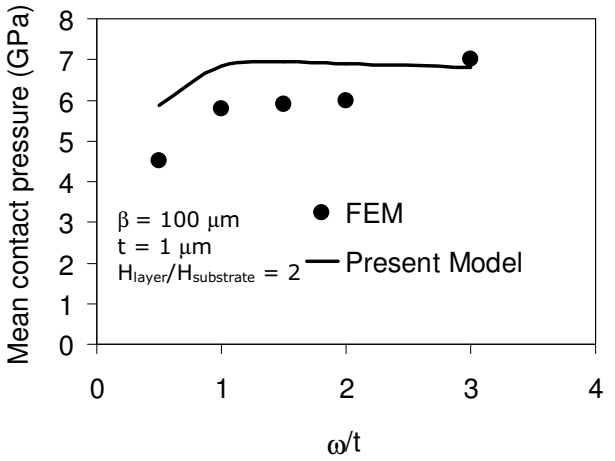

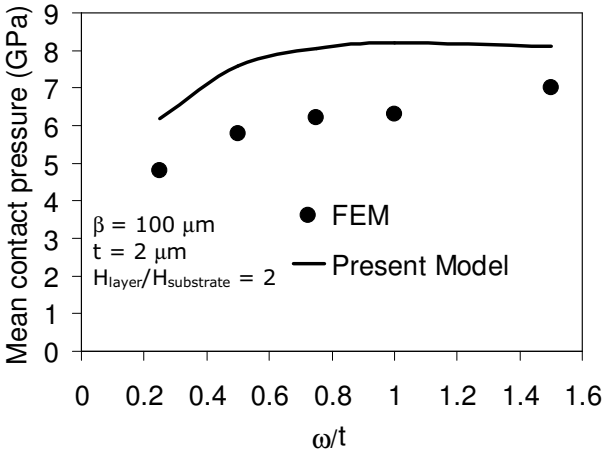

Figure C.4: Continued

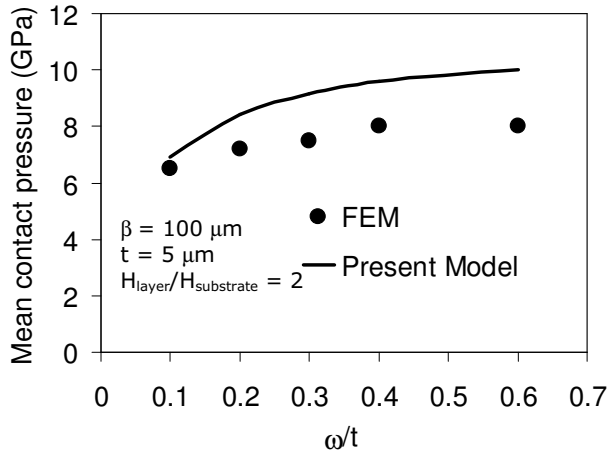

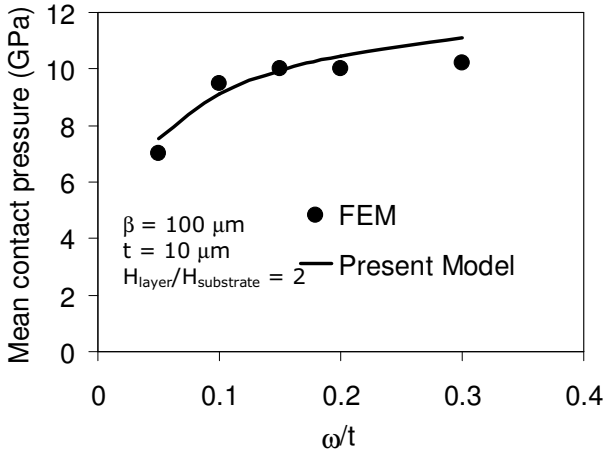

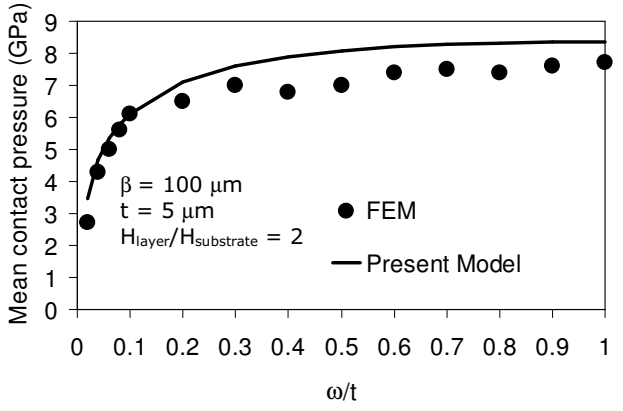

Figure C.4: Continued

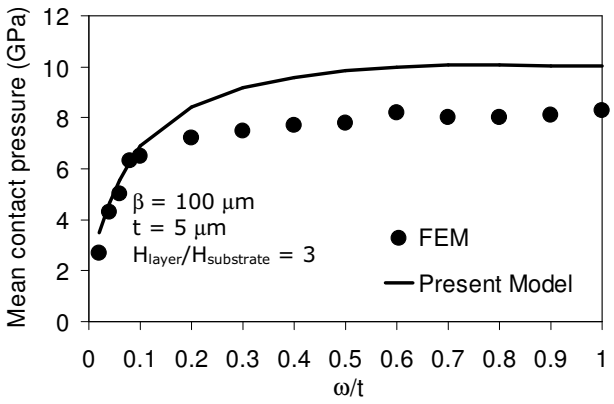

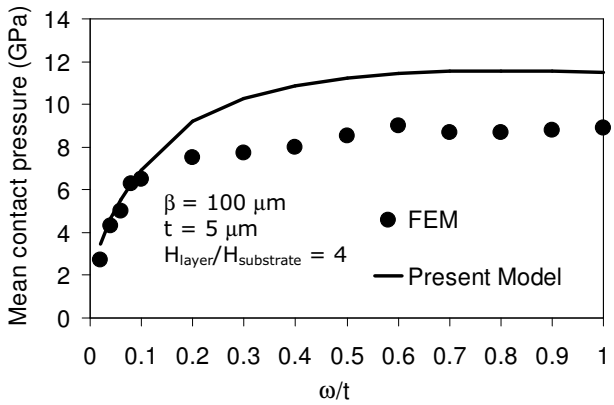

Figure C.4: Continued